

ABSTRACT

Title of Dissertation: INVESTIGATION OF NANOPHOTONIC
STRUCTURES FOR IMAGING AND
SENSING

Zhijian Zhang, Doctor of Philosophy, 2017

Dissertation directed by: Professor Miao Yu
Department of Mechanical Engineering

The ability to image micro/nano scale objectives with miniaturized optical components has always been of great interest due to its great potential in applications such as microscopy, nanofabrication, and biomedical monitoring. However, in traditional practice using dielectric lenses, the focal size is inevitably limited by the Abbe's diffraction limit ($0.51f\lambda/\rho$). Here, λ is the wavelength in vacuum, and f and ρ are the focal length and the radius of the lens, respectively. Moreover, the performance of conventional spherical lenses deteriorates as their sizes approach the wavelength. On the other hand, owing to the recent advances in micro/nano

fabrication techniques, miniature sensors have received much attention, which are highly desirable in many sensing applications for physical, chemical, and biomedical parameter measurements. However, the performance of miniature sensors usually suffers from the similar difficulty as miniaturized imaging systems. Recently nanophotonic structures have been explored for the development of miniaturizing imaging and sensing systems due to their capability of confining and manipulating light at a subwavelength scale.

In this dissertation work, several different mechanisms that nanophotonic structures can be used to help enhance the performance of imaging and sensing in miniaturized systems are investigated. First, plasmonic lens utilizing the nanophotonic structure to achieve the subwavelength focusing ability is studied. Three different regions in the plasmonic lens design are defined. Furthermore, a plasmonic lens in the Fresnel's region is designed and k.ed to achieve a sub-diffraction limit focus. Second, radially polarized light generated by the TEM mode in the annular aperture in metal is investigated, which can further enhance the focusing ability. Third, in terms of sensing, an ultra-thin plasmonic interferometer constructed with a nano-hole array is fabricated on a fiber facet. By using this structure, the multi-parameter sensing capability of this interferometer is demonstrated; high sensitivity refractive index and temperature sensing are achieved. Finally, a novel sensor design based on the cladding modes and buffer modes generated by the planar grating on the fiber facet is proposed. Experimental studies of this sensor demonstrate its superior temperature sensitivity and the potential of multi-parameter sensing.

INVESTIGATION OF NANOPHOTONIC STRUCTURES FOR IMAGING AND
SENSING

By

Zhijian Zhang

Dissertation submitted to the Faculty of the Graduate School of the
University of Maryland, College Park in partial fulfillment
of the requirements for the degree of
Doctor of Philosophy
2017

Advisory Committee:

Associate Professor Miao Yu, Chair

Professor Bongtae Han

Professor Don L. DeVoe

Professor Patrick F. McCluskey

Professor Christopher C. Davis, Dean's Representative

© Copyright by

Zhijian Zhang

2017

Dedication

To my wife Chenlu, my daughter Ruochen, and my parents

Acknowledgements

First of all, I would like to express my sincere gratitude to my advisor, Professor Miao Yu, for her consistent support and guidance through my whole Ph. D. study. This dissertation can never be done without her intellectual input and the encouragement she gave to me. I have learned a lot from her through this journey, not only scientific knowledge but more importantly the attitude to conquer difficulties. This unseeing spiritual wealth is the most valuable treasure I gained in the past five years.

I would like to thank the other members in my committee. I thank Professor Bongtae Han. I was really impressed by how fast he responded to my help requests and how detailed his suggestions are. I am very grateful to Professor Don L. DeVoe. When I need some help or recommendation, he is always responsive and helpful. I thank Professor Patrick F. McCluskey for his kind help and advice. I am thankful to Professor Christopher C. Davis. As such an expert in plasmonics, I am really lucky to have his comments and suggestions to improve my dissertation.

I also want to thank all the colleagues in the Sensor and Actuators, Yuxiang Liu, Cheng Pang, Haijun Liu, Hyungdae Bae, Felix Stief, Laith Sawaqed, Zhongshan Wen, Ying Chen, Hyuntae Kim, Randy Ganye, Yongyao Chen, and Jon Tedeschi. I could not finish this dissertation work without their help. More importantly, they made me a colorful and joyful campus life there in College Park.

I want to thank Dr. Douglas A. Olson, Dr. Joshua Schumacher, Dr. Zeeshan Ahmed, and Dr. Jingyun Fan in National Institute of Standards and Technology. With their help,

I got the access to the great facilities. Moreover, the discussions with them made my fabrication and measurement better and better.

I am grateful to all the group members in Dr. Peter Choyke and Dr. Hisataka Kobayashi's group in National Institute of Health, especially Dr. Tadanobu Nagaya and Dr. Yuko Nakamura. They broadened my horizons in the area of biomedicine. With them, I find the beauty how engineering helps real-world solutions.

My deepest gratitude goes to the love of my life, my loving wife, Chenlu Wang. Not to mention her tremendous supports, I cannot thank her enough for accompanying me, watching me and being there for me not only throughout my Ph.D. study but also my whole journey of growing from a boy to a man, and from a man to a father. While I am finishing my dissertation here in Maryland, she is starting a new job, and at the same time taking care of our sweetest daughter, Ruochen, in Texas. I could not even imagine how difficult that is for her. For that, I will always be indebted to her. Moreover, I thank my little princess, Ruochen for all the joy and happiness she brought. Thank my parents and parents-in-law for their unconditional love and help. My great friends, Xue Fei and Lance, Yuanting, Lin Zhu, Donglei, Rian and Jinglei, Christy and Vali, Qi Xia and Kelvin, and everyone in the soccer team, thank you all!

Table of Contents

Acknowledgements.....	iii
Table of Contents	vi
List of Figures	viii
Chapter 1. Introduction and background	1
1.1. Problem of interest.....	1
1.2. Literature review	6
1.2.1. Plasmonic lens	6
1.2.2. Plasmonic structures with radially polarized light.....	18
1.2.3. Plasmonic structures for sensor miniaturization.....	26
1.2.4. Fiber optic sensors based on cladding modes and buffer-guided modes	31
1.3. Motivation for this doctoral research.....	38
1.4. Objectives and scope of the dissertation.....	40
1.5. Organization of the dissertation works	41
Chapter 2. Plasmonic lens in different regions	42
2.1. Plasmonic lens overview.....	42
2.2. Plasmonic lens in different regions: properties and limitations.....	45
2.2.1. Subwavelength focusing in surface plasmon dominating region	45
2.2.2. Plasmonic focusing in Fresnel region and Fraunhofer region	48
2.3. Plasmonic lens design in Fresnel region.....	57
Chapter 3. Radially polarized light generated by TEM mode resonance and its applications	69
3.1. Introduction.....	69
3.2. TEM resonance generated with inclined incidence	70
3.2.1. Theoretical model	70
3.2.2. Simulations with PEC.....	73
3.2.3. Simulations with silver	75
3.3. TEM resonance generated with normal incidence on PEC	77
3.4. Surface plasmon dominating region plasmonic lens with radially polarized light generated by TEM resonance	79
Chapter 4. On-fiber plasmonic structures for multi-parameter sensing.....	87
4.1. Overview of on-fiber multi-parameter sensing.....	87
4.2. On-fiber plasmonic interferometer design and fabrication.....	89
4.3. On-fiber plasmonic interferometer fabrication and sensing measurement .	93
4.4. Discussion for on-fiber plasmonic interference.....	97
4.5. Multi-parameter sensing with a planar grating on the facet of a multimode fiber	101
Chapter 5. Cladding mode and buffer-guided mode excited by a planar grating on a fiber facet for multi-parameter sensing.....	110
5.1. Introduction of cladding modes and buffer-guided modes in SMF.....	110
5.3. Multi-parameter sensing	119
Chapter 6. Summary	126
6.1. Summary of the dissertation work	126

6.2. Future work.....	129
Appendix A: Protocol for Nanofabrication on Fiber Facet	131
Appendix B: List of Publications.....	144
Bibliography	147

List of Figures

Figure 1.1 (a) SPP-based far-field microscope setup. (b) SPP dispersion on the gold-glycerine interface[19].	7
Figure 1.2 (a) SEM of a triplet nanohole array which has a negative effective refractive index[21]. (b) AFM image of a magnifying superlens enabled by hyperbolic metamaterial.	7
Figure 1.3 Experimental setup for NSOM measurement of plasmonic lens fabricated on silver film[12].	9
Figure 1.4 Calculated intensity for the x (a) and z (b) component of the electric field for a silver disk 150 nm thick with a diameter of 6 μm . (c) Comparison of the cross section of the calculate electric field along x direction for the disk in a and the measured NSOM intensity for a circle milled into a 150 nm thick silver film with a 6 μm diameter. The period of the fringes is 244 nm [12].	9
Figure 1.5 SEM image of a plasmonic lens with 15 rings. The scale bar is 5 μm [74].	10
Figure 1.6 Plasmonic lens array on a lithography writing head[78].	11
Figure 1.7 A schematic of a nano-slit array with different width formed on thin metallic film [26].	12
Figure 1.8 Dependence of propagation constant of SPPs in the slit on the slit width. The solid and dashed lines represent real and imaginary part, respectively. The dotted line stands for plane EM wave in air[26].	13
Figure 1.9 (a) FDTD calculated result of normalized Poynting Vector in z for designed metallic nano-slits lens. The film thickness is 500nm, and the total slits number is 65. The structure's exit side is posited at $z=0.7 \mu\text{m}$. (b) Cross section of the focus at $z=1.5 \mu\text{m}$ [26].	14
Figure 1.10 Planar lens based on nanoscale slit array in metallic film. (a) The geometry of the lens. (c)Focusing pattern measured by confocal scanning optical microscopy (c)FEM field simulation[27].	15
Figure 1.11 (a) Schematic diagram of the sandwiched plasmonic lens with chirped circular slits corrugated on Au film.(b) Measured 3D E-field intensity distribution of the plasmonic lens vs. lateral x and propagation distance z using NSOM[29].	16
Figure 1.12 (a) Schematic of the planar plasmonic lenses formed by variant cross-shaped aperture arrays. (b) The transmission efficiency (red solid line) and phase(blue dotted line) of the transmitted field as function of arm length at the working wavelength.(c) Measured axial intensity profile (in the y-z plane) of light passing through[28].	16
Figure 1.13(a) SEM image of a 5 μm patch of nanoholes with 400-nm period [30]. (b). nanolens made of periodical concentric silver rings[84]. (c) Surface plasmon resonances were tuned by changing the lattice geometry[30].	18
Figure 1.14 Diagram of the proposed setup for evanescent Bessel beam generation[85].	19
Figure 1.15 Numerical simulation results for (a) total field strength at the bottom of the silver layer for radial polarization, (b) total field strength at the bottom of the silver layer for linear polarization illumination as a comparison[85].	20

Figure 1.16 Schematic diagram showing the geometry of the plasmonic lens and the orientation of the field components under radial and linear polarization illumination[35].	21
Figure 1.17 NSOM measurement showing SPP focusing in the plasmonic lens illuminated by linearly polarized light[35].	22
Figure 1.18 NSOM measurement showing SPP focusing in the plasmonic lens illuminated by radially polarized light[35].	22
Figure 1.19 Coherent superposition of two orthogonally polarized modes to form azimuthally and radially polarized beams; (a) azimuthally polarized doughnut beam; (b) radially polarized doughnut beam[42].	23
Figure 1.20 Arrangement for transformation of a linearly polarized Gaussian beam to a radially or azimuthally polarized beam. The insets show the SVR scheme, together with an SVR photo [46].	24
Figure 1.21 Drawing of the conical Brewster prism[45].	25
Figure 1.22 SEM images 20 periods of concentric metallic rings[48].	25
Figure 1.23 three commonly used configurations of SPR sensors: (a) prism coupler-based SPR system; (b) grating coupler-based SPR system; (c) optical waveguide-based SPR system [53].	27
Figure 1.24 Schematic diagrams illustrating a localized surface plasmon[54].	28
Figure 1.25 Schematic diagrams illustrating two-slit plasmonic interference at metal/dielectric interference.	29
Figure 1.26 (a) SEM micrograph of a groove-slit-groove (GSG) plasmonic interferometer. (b) Normalized per-slit transmitted intensity spectra and relative intensity change of the plasmonic interferometer measured at various concentrations of glucose in water[55].	30
Figure 1.27 (a) Schematic (cross section view) of the hybrid metal-dielectric structure for enhancing LSP integrated on the optical fiber tip. (b) Measured reflectivity and calculated electric field intensity distributions[56].	31
Figure 1.28 SEM image on the fiber grating surface after etching[108].	32
Figure 1.29 Structure of etch-eroded FBG for ambient refractive index sensing[109]	33
Figure 1.30 Experimentally measured transmission spectrum of an LPFG with a period of 198 μm [112].	34
Figure 1.31 Experimentally measured transmission spectrum of a 8 mm long standard FBG photo-written in a single-mode step-index optical fiber [61].	34
Figure 1.32 Schematic of a TFBG.	35
Figure 1.33 Experimentally measured transmission spectrum of a 8 mm long $\theta=16^\circ$ -tilted TFBG surrounded by air[61].	35
Figure 1.34 Schematic of cladding mode generated by core diameter mismatch.	36
Figure 1.35 Taper-based SMF Michelson interferometer[63].	37
Figure 1.36 (a) Geometry of the WGM interference model. (b) Bend loss as a function of wavelength for the fiber with WGM. [68]	37
Figure 1.37 (a) Experimental setup for testing the coated-SMF loop temperature sensor. (b) The temperature response of the three types of coated-SMF loop sensors[73].	38
Figure 2.1 Schematic of plasmonic focusing in three different regions	44

Figure 2.2 Attenuation length (range of the SPP dominating region) of SPP in the dielectric as a function of wavelength. The permittivity of air ($\epsilon_a \approx 1.0$) and the permittivity of gold and silver found in [127] were used .	47
Figure 2.3 Schematic of a plasmonic lens with an arbitrary design, which has a radius ρ and a designed focal length of f . P is an arbitrary point on the lens aperture, which is away from the lens center by a distance a . F is the focus. P' is an observation point on the focal plane, which is away from F by a distance x . α is the semi-angle of the light cone from the lens aperture to the focus. θ is the observation angle of P' to the optical axis.	50
Figure 2.4 Field intensity distribution along x-direction (a) and y-direction (b), while the incident light is under x-direction polarization and with different incident angles 0° and 40°	55
Figure 2.5 Schematic of a plasmonic lens with a single ring aperture with radius ρ and width w , which is milled in a gold film with thickness t .	58
Figure 2.6 Fig 6. FDTD simulation results obtained for a plasmonic lens with a single ring slit: (a) intensity distribution of the focal plane along x-z direction, (b) intensity distribution along the optical axis, and (c) intensity distribution along the x-direction of the focal plane.	59
Figure 2.7 Schematic of a plasmonic lens of 4 concentric ring slits with radii of r_1, r_2, r_3, r_4 and widths of w_1, w_2, w_3, w_4 milled on a gold film with a thickness of t . The designed focal length is f . F is the focal point and O is the center of the lens.	60
Figure 2.8 FDTD simulation results of a plasmonic lens with 4 rings: (a) field intensity distribution in the x-z plane, (b) intensity distribution along the optical axis, and (c) intensity distribution along the x-direction of the focal plane.	62
Figure 2.9 FDTD simulation results of a 4 ring plasmonic lens with an enlarged width: (a) field intensity distribution in the x-z plane, (b) intensity distribution along the optical axis, and (c) intensity distribution along the x-direction of the focal plane.(d) Field distribution in the x-z plane of a 4 ring plasmonic lens with perfect conductor.	63
Figure 2.10 Comparison of angular intensity distribution of a single ring lens $J_0(\xi)$ (red line) and a single hole lens $J_1(\xi)$ (black line)	65
Figure 3.1 Schematic of annular aperture in a metal plate. The electric field polarization of the TEM mode is also shown[135].	71
Figure 3.2 Transmission spectrum for the annular aperture array with PEC. The field distribution is calculated at the end of the emitting side.	74
Figure 3.3 Transmission spectrum for 1st order TEM mode for $P=300\text{nm}$ and $P=600\text{nm}$.	74
Figure 3.4 Transmission spectrum for the annular aperture array with silver. The field distribution is calculated at the end of the emitting face.	76
Figure 3.5 The field distributions at the cross-sections from side view for (a) 193 THz and (b) 440 THz.	76
Figure 3.6 Schematic of the annular aperture array with dual gratings on the top and bottom.	77
Figure 3.7 (a) The transmission spectrum for the structure in Figure 3.6 under normal incidence. (b) The field distribution calculated at the end of the emitting face at 317	

THz. (c) The direction of electric field distribution at the end of the emitting face at 317 THz. (d) The field distributions at the cross-sections from side view at 317 THz.	78
Figure 3.8. Sketch of a plasmonic lens under inclined illumination and its top view. The focus point B of the plasmonic lens shifts away from the center under inclined illumination [15]	80
Figure 3.9 Schematic of a plasmonic lens with a single ring aperture with radius ρ and width w , which is milled in a gold film with thickness t	81
Figure 3.10 The field intensity distribution at the plane 10 nm distance away from the designed plasmonic lens surface for $\theta=45^\circ$ and $\lambda=1435$ nm.	81
Figure 3.11 The field intensity distribution at the plane 10 nm distance away from the designed plasmonic lens surface for $\theta=45^\circ$ and $\lambda=758$ nm.	83
Figure 3.12(a) The field intensity distribution at the x-z cross section for the designed plasmonic lens surface for $\theta=45^\circ$ and $\lambda=758$ nm. (b) The intensity along the optical axis.	84
Figure 3.13 The field intensity distribution at the y-z cross section for the designed plasmonic lens surface for $\theta=45^\circ$ and $\lambda=758$ nm. (b) The intensity along the y axis for $x=0$ and $z=0$	85
Figure 4.1(a) Schematic of on-fiber plasmonic interferometer with nano-hole array. The inset shows the unit cells of the array ($t=150$ nm, $d= 528$ nm and $\Lambda = 1055$ nm). (b) SEM of the fabricated sensor. (c) SEM of the nano-hole array.	89
Figure 4.2(a) Schematic of the experimental setup, (b) typical reflection spectrum of the sensor in glucose solution at room temperature (glucose concentration 10 %), (c) reflection spectrum of SP resonance extracted from (b), (d) reflection spectrum of plasmonic interference extracted from (b), (e) schematic of the on-fiber plasmonic interference, (f) reflection spectrum obtained with RCWA simulations for a hole array structure of infinite size in a 10 % glucose solution. The insets show the field distributions at the SP resonance peak and the Wood's anomaly dip in one unit cell.	92
Figure 4.3(a) Extracted reflection spectra dominated by SP resonance with respect to refractive index change, (b) peak wavelength of the SP resonance versus refractive index, (c) extracted reflection spectra dominated by plasmonic interference with respect to different refractive indices, (d) effective OPD versus refractive index.	95
Figure 4.4(a) Extracted reflection spectra dominated by SP resonance with respect to temperature change, (b) peak wavelength of SP resonance versus temperature, (c) extracted reflection spectra due to plasmonic interference with respect to temperature change, and (d) effective OPD versus temperature.	96
Figure 4.5 The comparison of dispersion relations of surface plasmons on the hole array structure and on the flat silver surface. The dashed line represents the light dispersion in the fiber core region	100
Figure 4.6 SEM pictures of the planar grating fabricated on a MMF end face.	103
Figure 4.7 Schematic of multimode interference.	104
Figure 4.8 (a) reflection spectra of multimode interference with respect to temperature change (b) peak wavelength position as temperature increased (black)/ decreased (red) over the range from 30 °C to 100 °C.	105
Figure 4.9 Schematic of the optical interrogation system with tunable laser	106
Figure 4.10 reflection spectra of the sensor in air and in water around 1550 nm.	107

Figure 4.11 (a) reflection spectra of the sensor in IPA solution with different concentration, (b) reflection intensity at the fixed wavelength 1507 nm as the refractive index of the solution changes	108
Figure 5.1 Schematic of core mode (red line) coupled to cladding mode (blue lie) in a step-index SMF by scattering.	110
Figure 5.2 Schematic and SEM of the planar grating fabricated on a fiber end face to generate buffer modes and cladding modes.....	114
Figure 5.3 (a) Schematic of the optical interrogation system, and (b) a typical reflection spectrum of the sensor with $Z \approx 28$ cm.....	115
Figure 5.4 (a) OPDs extracted from the reflection spectrums for the cases of $Z \approx 10$ cm, 28 cm and 50 cm (b) effective refractive index of the buffer extracted from reflection spectrums in the buffer modes dominating wavelength range, and (c) effective refractive index of the buffer extracted from reflection spectrums in the cladding modes dominating wavelength range.....	118
Figure 5.5 Electric field intensity distributions of the first few modes supported at 736 nm and 840 nm in the system.	119
Figure 5.6 (a) the whole reflection spectra with respect to temperature change, (b) reflection spectra around peak A with respect to temperature change, (c) reflection spectra around peak B with respect to temperature change, (d) peak positions of peak A with respect to different temperatures, (e) peak positions of peak B respect to different temperatures,	120
Figure 5.7 (a) mean peak positions of peak A with respect to different temperatures in three different measurements, (b) mean peak positions of peak B with respect to different temperatures in three different measurements.	122
Figure 5.8 (a) the whole reflection spectra with respect to axial strain change, (b) reflection spectra around peak A with respect to axial strain change, (c) reflection spectra around peak B with respect to axial strain change, (d) peak positions of peak A with respect to different axial strains, (e) peak positions of peak B respect to different axial strains.....	123
Figure 5.9 (a) mean peak positions of peak A with respect to different axial strains in three different measurements, (b) mean peak positions of peak B with respect to different axial strains in three different measurements.....	124

Chapter 1. Introduction and background

1.1. *Problem of interest*

Nanophotonics, which focuses on the study of the behavior of light on the nanoscale, has drawn much attention for decades, since the miniaturization of optical components becomes more and more important in many applications, such as photolithography [1, 2], optical manipulation [3], imaging [4] and sensing [5, 6]. With the capability of confining and manipulating light at subwavelength, nanophotonic structures offer novel properties and high power efficiency [7]. In general, nanophotonics covers a broad range of topics from nanotechnology applications to fundamental nanoscience. This dissertation mainly focuses on the fundamental studies of the principles of some specific nanophotonic structures, which can help enhance the performance of imaging and sensing of miniaturized systems, as well as their applications.

A plasmon, generated on a metal nanophotonic structure, is the energy excitation of collectively oscillating free electrons. Usually, it couples with a photon at the interface of metal and dielectric and forms a quasiparticle which is called surface plasmon polariton (SPP) or called surface plasmon (SP)[8]. For the half-infinite metal and dielectric interface, we could easily derive the dispersion of surface plasmon by applying Maxwell equation and boundary conditions as[9]

$$k_{sp} = k_0 \sqrt{\frac{\epsilon_d \epsilon_m}{\epsilon_d + \epsilon_m}}, \quad (1.1)$$

where k_0 is the free space wave vector, ε_d is the dielectric permittivity and ε_m is the metal permittivity. The permeability is assumed to be 1, which is true for general cases. It is noted that the wave vector of SP k_{sp} is always larger than the free space wave vector ($k_{sp} > k_0$), which means that SP cannot be excited by the free space incidence on the smooth metal-dielectric surface. SP can be excited with Otto configuration and Kretschmann configuration, based on the attenuated total reflection method [10]. This method requires prisms and glancing incidence, which is not preferable for miniaturized systems. On the other hand, when subwavelength structures are fabricated at the interface, the incident light will be scattered by these structures and some component with a large wave vector can excite SP. These structures that support SP modes are called plasmonic structures, which have been intensely investigated to enhance the imaging and sensing system [5, 11].

With the help of SP, due to its shorter wavelength than free space light and its capability to confine and manipulate light in an ultra-small space [12-17], it has been shown that sub-diffraction-limit focusing and imaging can be achieved. Particularly, Prof. Davis' group demonstrated that a large effective refractive index could be achieved with matching the permittivity of dielectric and metal. Therefore, an in-plane image magnification lens was fulfilled with the optical resolution about 60 nm at 515 nm working wavelength [18-20], which is far beyond the diffraction limit. Later, they demonstrated that similar resolution can also be achieved by using different types of nanophotonic structures called photonic metamaterials [21-23]. Furthermore, they showed that 30 nm resolution could be achieved by applying digital filters in the system [24, 25]. Nevertheless, this kind of focusing and imaging

can only be achieved in the very near-field, since the SP mode is tightly confined near the surface. These kinds of plasmonic structures which are used to focusing light are called plasmonic lenses. Other studies have been conducted to develop plasmonic lenses in the diffractive regions to replace traditional refractive index based microlenses or to decrease the lens size [26-31]. For example, a plasmonic lens with one-dimensional (1D) nanoslit array defined on a metal surface was proposed and studied through numerical simulations [26]. The experimental demonstration of a lens with a similar pattern was reported later by Verslegers *et al.* [27]. More recently, two-dimensional (2D) plasmonic focusing lenses were realized with chirped circular nanoslits [29] and cross-shaped aperture arrays [28, 31]. Furthermore, a plasmonic lens in the far-field region was also developed by using nanohole patches [30]. Even with the above mentioned plasmonic lens development in the diffractive regions, the physical behaviors of plasmonic focusing in these regions have never been thoroughly studied, and the focus size is still within the diffraction limit in these designs.

On the other hand, radially polarized light has been applied to traditional optical systems to reduce the focus size by utilizing its radial symmetry for years [32, 33]. It has been demonstrated that radially polarized light can enhance the focusing ability of plasmonic lenses as well [34-41]. It cannot only help reduce the focus size but also help increase the focal length because a Bessel beam can be generated due to the radial symmetry. However, it is not easy to generate radially polarized light. The methods people used to generate radially polarized light are either costly or having its own drawbacks, including coherent superposition of two orthogonally polarized

modes [42], space-variant subwavelength gratings[43, 44], conical Brewster prism [45], integrate spatially variant wave plate [46], combination of SLMs [47], concentric metallic gratings fabricated on optical fibers [48]. In addition, many applications of plasmonic lenses require complicated alignment of the optical axis with the axis of the radially polarized light.

Regarding sensing, nanophotonic structures play important roles to shrink the sensor size and improve the performance. Sensor miniaturization has received much attention in a broad range of applications for physical, chemical and biomedical parameters sensing [49, 50]. Owing to the recent advances in micro/nano fabrication techniques [51], miniature sensors can be realized in smaller and smaller scales. As a popular miniature sensor platform, optical fiber based sensors have been extensively investigated because of their small sizes, light weight, flexibility, robustness to electromagnetic interference, and remote sensing ability [49].

Nevertheless, as the size of a conventional optical element gets closer to the operating wavelength, the size of fiber-optic sensors seems irreducible due to the diffraction limit [52], Nevertheless, recent studies on surface plasmons (SPs) shed some light on the realization of optical devices with an even smaller form factor, since SPs enable the confinement and manipulation of light at the subwavelength scale [14]. With the help of SPs, sensors with excellent sensing ability and ultra-thin film configurations have been demonstrated, including SP resonance [53], localized SP [54], and plasmonic interferometer based sensors [55]. Recently, the facet of an optical fiber tip is found to be an appealing platform to integrate plasmonic structures for sensing applications [56, 57]. However, all of these sensors are either limited to

single parameter sensing or can be sensitive to multiple parameters but are not capable of distinguishing different parameters.

Among the optical fiber sensing methods, there is one well-known and widely-used scheme which utilizes cladding modes to measure the environment parameters. Since a cladding mode extends its evanescent field into the surrounding environment [58], it is very sensitive to the environment parameter change, especially the refractive index change. In the beginning, short- or long-period fiber gratings were used to couple the light from fiber core to cladding to form cladding modes [59, 60]. Later, tilted fiber Bragg grating (TFBG) was found to be more efficient in generating cladding mode [61, 62]. However, fiber gratings whose lengths vary from millimeters to centimeters are still too long for the miniaturizations propose, especially when it comes to the spatial resolution of the measurement. Other methods to generate cladding modes, such as fiber tapering [63-65] and core diameter mismatch [66, 67], suffer from large coupling loss. In addition to the cladding layer, the buffer layer of optical fibers can support guided modes as well under some circumstances. The whispering gallery mode (WGM) supported by the buffer coating has been recognized [68] after the studies of bend-induced losses [69, 70]. As can be expected, high-sensitivity temperature sensor [71-73] have been achieved by WGMs due to the polymer material properties of the buffer layer. Nevertheless, in most of the previous studies, a large fiber bending is needed to generate the WGMs in the buffer layer. Nanophotonic structures give the potential to design a system with small size, large cladding mode coupling coefficient, and generating buffer-guided mode without bending.

This dissertation work is aimed to achieve enhanced understanding of nanophotonic structures in terms of their applications in imaging and sensing, and apply such understanding to enhance the performance of miniaturized imaging and sensing systems.

1.2. Literature review

1.2.1. Plasmonic lens

SPP has been used to enhance the resolution of imaging systems thanks to its short wavelength for a long time. It has been first experimentally demonstrated by Smolyaninov et al.[18, 19]. In their experiment, laser light illuminates a parabolically shaped glycerin droplet through a glass prism and excites SPPs propagating at the gold and glycerin interface, as shown in Figure 1.1 (a). The gold-glycerin interface provides the large value of the effective index, seen from the SPP dispersion in Figure 1.1(b). Thus SPPs with the wavelength about 70 nm travels along the interface and reflects at the boundary of the glycerin droplet which functions as a magnifying lens of SPPs. SPPs are partially scattered above the prism and can be observed by a microscope. In the end, an optical resolution of 60 nm is achieved by 515 nm laser illumination, which is far beyond the diffraction limit.

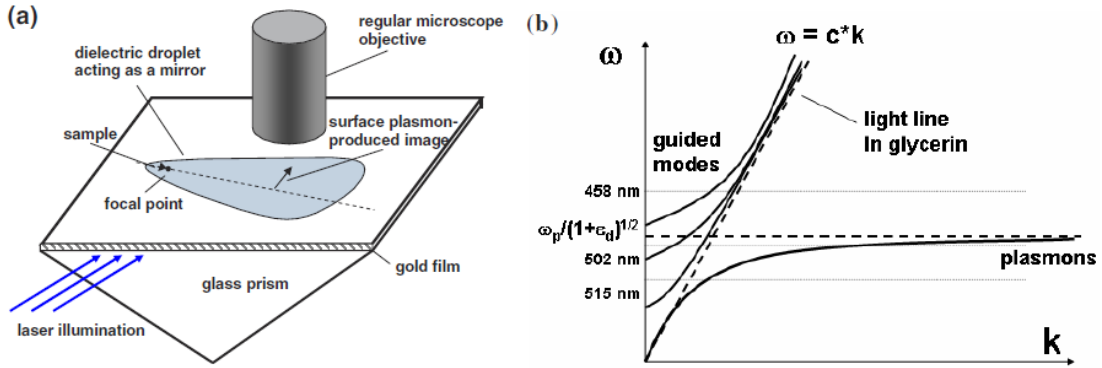


Figure 1.1 (a) SPP-based far-field microscope setup. (b) SPP dispersion on the gold-glycerine interface[19].

Later, Smolyaninov et al. has also demonstrated SPP can enhance the resolution of 2D imaging by achieving a negative refractive index mirror with a nanohole array photonic crystal structure at the surface[21], shown in Figure 1.2 (a), as well as a photonic metamaterial structure with a hyperbolic dispersion[22], shown in Figure 1.2 (b).

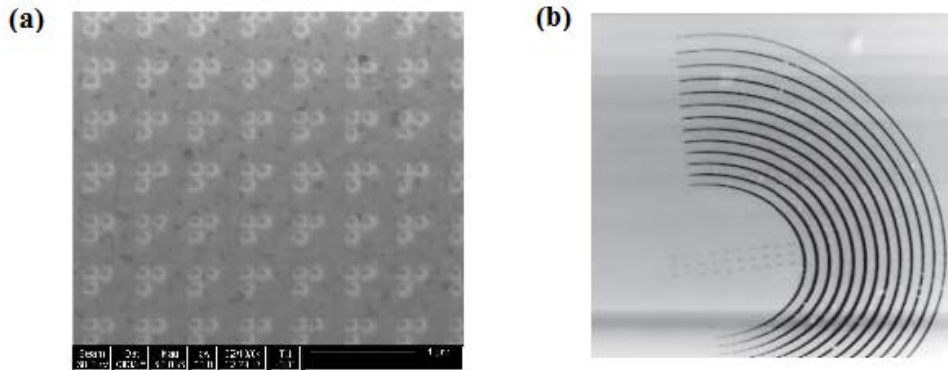


Figure 1.2 (a) SEM of a triplet nanohole array which has a negative effective refractive index[21]. (b) AFM image of a magnifying superlens enabled by hyperbolic metamaterial.

Although the works mentioned above have accomplished great successes to enhance the resolution far beyond the diffraction limit by up to $1/7$ of the illuminating wavelength ($\lambda_0/7$), or even further to $\lambda_0/14$ with additional digital filters [24, 25], they usually require additional excitation mechanisms for SPPs, like the glancing

incidence with glass prism shown in Figure 1.1(a). Other studies have been conducted to study metal nanophotonic structures which are designed to directly couple photons from free-space incidence to SPPs and focus light, which are named as plasmonic lenses. It is first investigated by Liu *et al.* [12] In their experiment, as shown in Figure 1.3, a single annular aperture is fabricated on a silver film deposited on a quartz substrate. Linearly polarized light illuminates on the structure from the substrate. Since the width of the slit is designed to be smaller than the half of the incident wavelength, large portion of the light will be diffracted at the edge and therefore excited propagating SPP at the surface. The energy will be guided toward the center of the structure to the focus spots, making the structure serve as a lens. Because of the linearly polarized incidence, the SPPs generated at the opposite edges of the slit have a phase different of π , thus a destructive interference can be found at the very center of the plasmonic lens. Therefore, there will be two focus spots around the center due to the constructive interference of SPPs. It is verified in their finite difference time domain (FDTD) simulation. The calculated field distribution is shown in Figure 1.4(a, b). Compared with the parallel field E_x , the electric field in the vertical direction E_z is the dominating term in the SPP field. Therefore it is demonstrated that there will be two focus spot around the center of the lens. In the experiment, the field intensity is scanned by near-field scanning optical microscopy (NSOM), and the cross-section intensity distribution is shown in Figure 1.4(c). Due to the characteristic of NSOM system which is more sensitive to E_x , the field distribution from NSOM scanning only shows the profile of E_x distribution, but it still demonstrates the focusing capability of

such plasmonic lens. A sub-diffraction-limit focus size 244 nm is achieved by considering the wavelength of the incident light is 514nm.

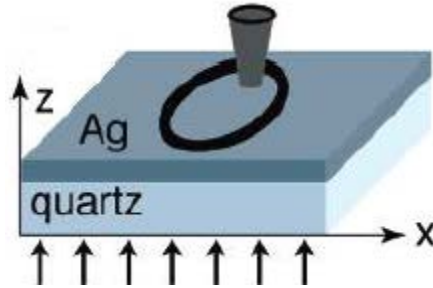


Figure 1.3 Experimental setup for NSOM measurement of plasmonic lens fabricated on silver film[12].

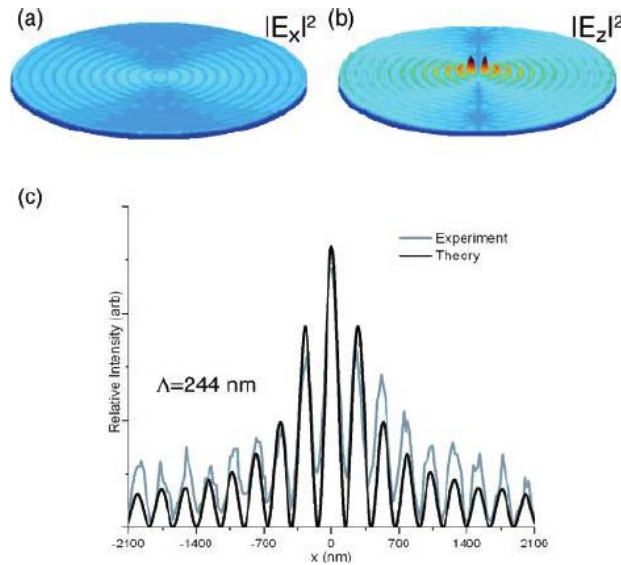


Figure 1.4 Calculated intensity for the x (a) and z (b) component of the electric field for a silver disk 150 nm thick with a diameter of 6 μm . (c) Comparison of the cross section of the calculate electric field along x direction for the disk in a and the measured NSOM intensity for a circle milled into a 150 nm thick silver film with a 6 μm diameter. The period of the fringes is 244 nm [12].

Since 2005, much attention has been drawn into the study of the plasmonic lens[15, 74-79], due to its obvious advantages for sensing and imaging. The circular grating has been added to the single ring lens to enhance the focus intensity [74], as shown in Figure 1.5. The circular grating serves a Bragg mirror which reflects the

outgoing SPPs back into the center of the lens. By doing that a 10-fold intensity enhancement is achieved.

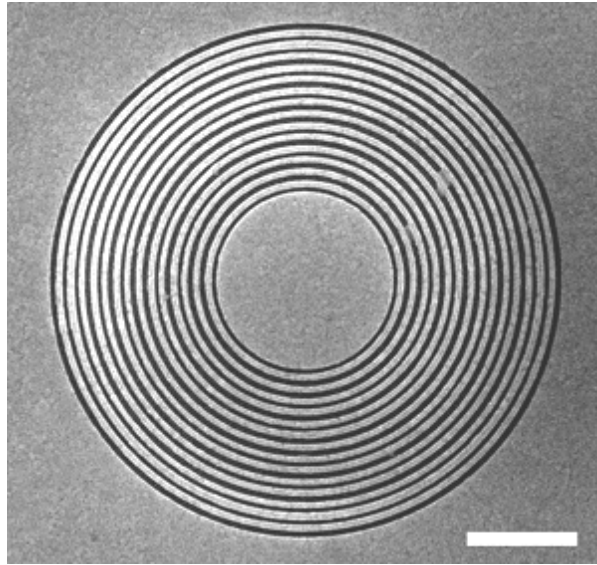


Figure 1.5 SEM image of a plasmonic lens with 15 rings. The scale bar is 5 μm [74].

Later, a plasmonic lens array, shown in Figure 1.6(a), has been applied to a maskless nanolithography system (Figure 1.6 (b)) [78]. With the help of plasmonic lens, an inexpensive parallel scanning probe lithography method with high speed and sub 100-nm lateral resolution have been achieved. Due to the high energy concentration from SPPs, the throughputs have been improved 2~5 orders of magnitude, compared with other maskless lithography techniques. Later, they have even achieved 22-nm lateral resolution by introducing localized surface plasmonic structure at the center of the plasmonic lens[77].

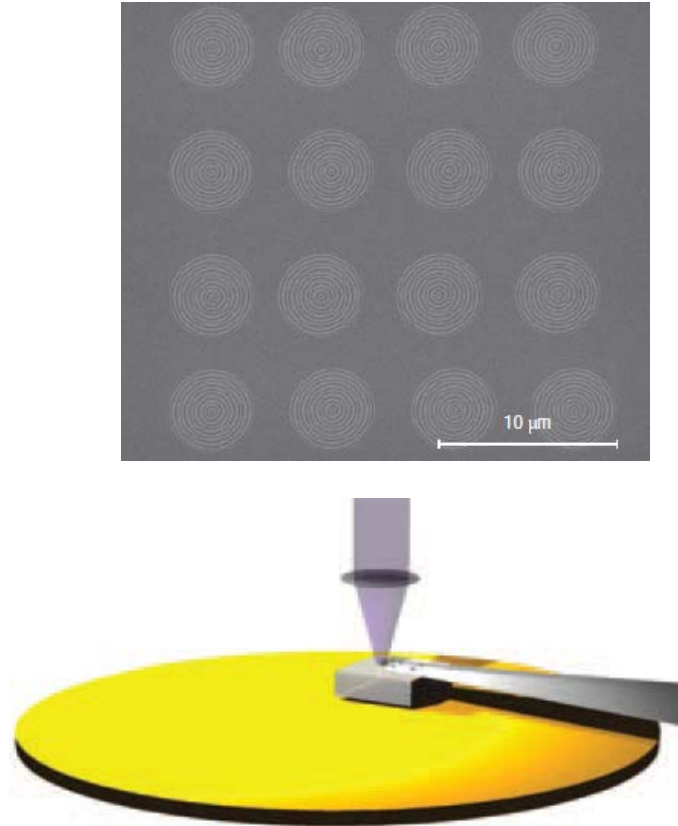


Figure 1.6 Plasmonic lens array on a lithography writing head[78].

Despite the success of focusing light to the sub-diffraction-limit spot size on the metal surface, the above-mentioned plasmonic lenses lack of the ability to focus light in the region away from the surface, since SPP decays exponentially along the direction perpendicular to the surface. Therefore it limits some applications. For example, for the plasmonic-lens-assistant maskless lithography we mentioned[78], an accurate aerodynamic flying head must be designed to maintain the distance as small as 10 nm to accommodate the short focal length of the plasmonic lens. To avoid this shortcoming, diffractive plasmonic lenses have been developed [26-31, 80-83].

A typical diffractive plasmonic lens design is shown in Figure 1.7 [26], where subwavelength nano-slits are milled through a silver film. Once a plane wave with TM polarization illuminates from one side of the silver film, SPPs are generated and

guided through the slits. In the metal/dielectric/metal structure, SPPs at the top and bottom surfaces will couple with each other, and the dispersion of the guided SPP mode can be expressed as [26]

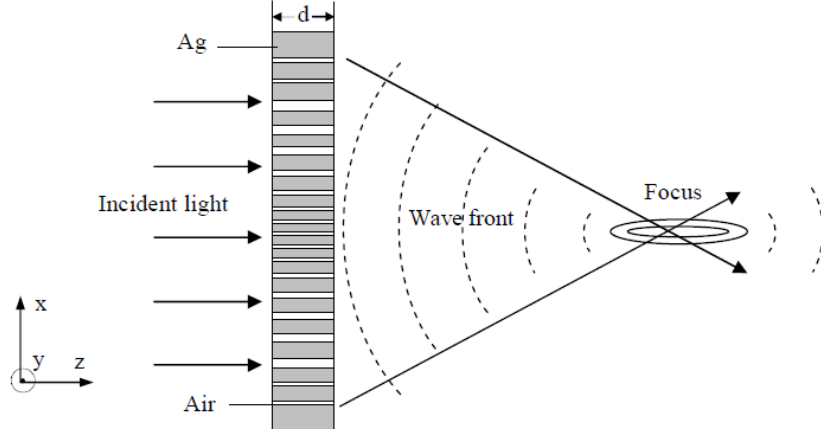


Figure 1.7 A schematic of a nano-slit array with different width formed on thin metallic film [26].

$$\tanh\left(\frac{w}{2}\sqrt{\beta^2 - \epsilon_d k_0^2}\right) = -\frac{\epsilon_d \sqrt{\beta^2 - \epsilon_m k_0^2}}{\epsilon_m \sqrt{\beta^2 - \epsilon_d k_0^2}}, \quad (1.2)$$

where w is the width of the slit, β is the complex propagating constant of the guided SPP mode, k_0 is the free space wave vector, ϵ_d and ϵ_m are the permittivities of the dielectric and metal respectively. Since k_0 , ϵ_d , ϵ_m are fixed, this equation shows the relationship between the propagation constant and the slit width, which is plotted as shown in Figure 1.8 [26].

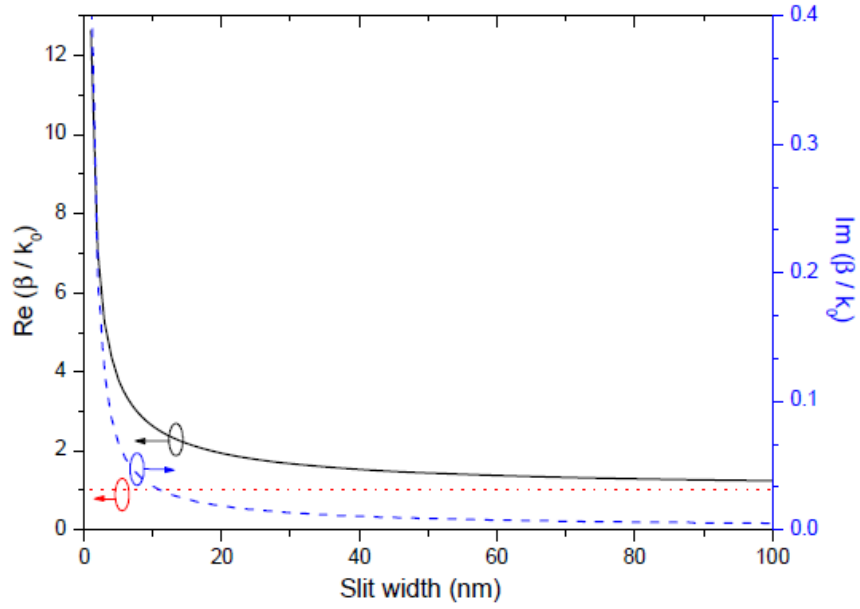


Figure 1.8 Dependence of propagation constant of SPPs in the slit on the slit width. The solid and dashed lines represent real and imaginary part, respectively. The dotted line stands for plane EM wave in air[26].

This relationship indicates a mechanism to modulate the phase at the outlets of the slits by changing the width of the slits. A curved wavefront can be formed by modulating the phase. And a focusing lens with the focal length f can be designed, while the phase of the slit sitting at position x satisfies the constructive interference requirement

$$\varphi(x) - \varphi_0 = 2N\pi + \frac{2\pi fn}{\lambda} - \frac{2\pi n \sqrt{f^2 + x^2}}{\lambda}, \quad (1.3)$$

where φ_0 is the phase at the center of the lens, λ is the free space wavelength, N is an integer and n is the refractive index of the propagating media.

According to this principal, a metallic nano-slit plasmonic lens has been designed, and its performance has been verified by FDTD simulation as seen in Figure 1.9. Slits with width from 10 nm to 70 nm have been milled through the silver

film with 500 nm thick. This diffractive plasmonic lens works at 650 nm and presents a focus with FWHM 270 nm and focal length 1.5 μm , shown in Figure 1.9.

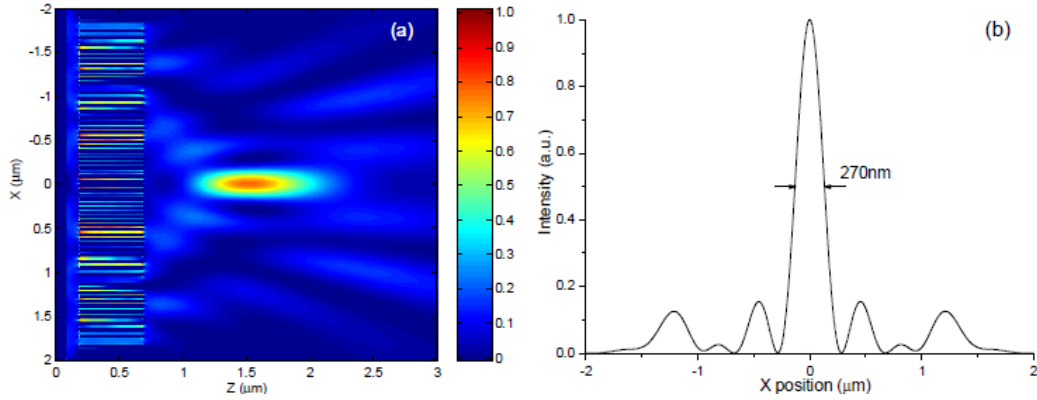


Figure 1.9 (a) FDTD calculated result of normalized Poynting Vector in z for designed metallic nano-slits lens. The film thickness is 500nm, and the total slits number is 65. The structure's exit side is positioned at $z=0.7 \mu\text{m}$. (b) Cross section of the focus at $z=1.5 \mu\text{m}$ [26].

Later, the diffractive plasmonic lens with nanoslits has been experimentally demonstrated [27]. 13 nano-slits have been fabricated on the silver film deposited on glass substrate (Figure 1.10 (a)). The focusing capability of a far-field cylindrical lens has been verified by showing the field distribution patterns scanned with confocal scanning optical microscope (CSOM) (Figure 1.10 (b)) and simulated by FDTD method (Figure 1.10 (c)). From the experiment and numerical results, a planar focus is achieved by the plasmonic lens with the FWHM 880 nm and focal length about 5.3 μm , while it is under TM-polarized incidence with the wavelength of 637 nm.

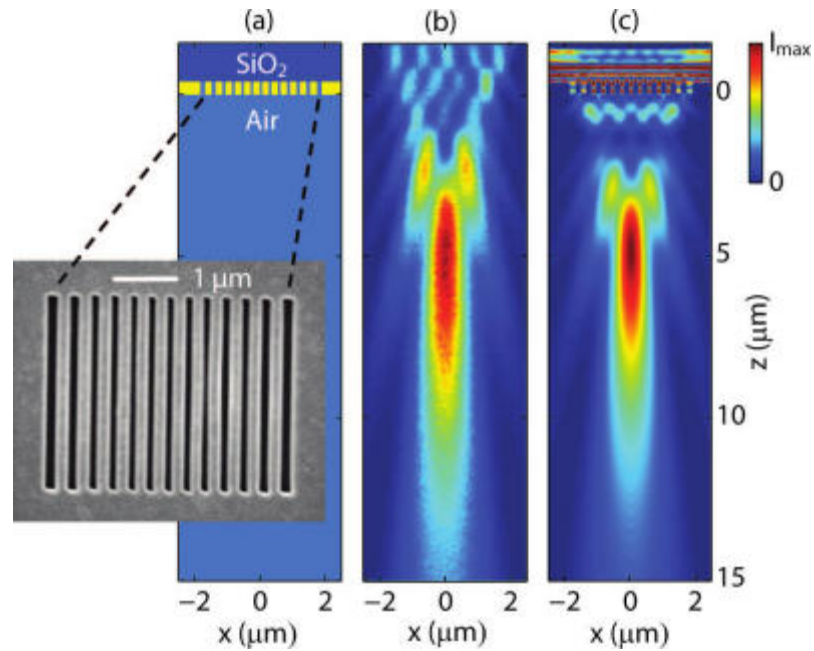


Figure 1.10 Planar lens based on nanoscale slit array in metallic film. (a) The geometry of the lens. (b) Focusing pattern measured by confocal scanning optical microscopy (c) FEM field simulation [27].

After the early investigations about one-dimensional (1D) diffractive plasmonic lenses which only focus light in plane, lots of studies have shown the three-dimensional (3D) focusing capabilities with different two-dimensional plasmonic (2D) lens designs. In the chirped circular nano-slits design [29], concentric circular apertures with various widths have been fabricated on a gold film, shown in Figure 1.11 (a). The widths of the circular slits control the phase of emitting light in the same way as in nano-slits mentioned before. 3D Field intensity distribution of the system under linearly polarized incidence has been detected by NSOM, as seen in Figure 1.11 (b). A strong focus at the focal length of $1.0 \mu\text{m}$ with the FWHM about 300 nm is verified.

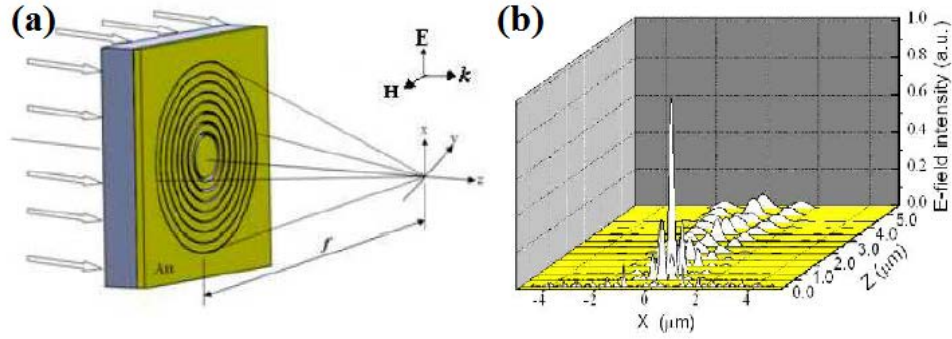


Figure 1.11 (a) Schematic diagram of the sandwiched plasmonic lens with chirped circular slits corrugated on Au film. (b) Measured 3D E-field intensity distribution of the plasmonic lens vs. lateral x and propagation distance z using NSOM[29].

Other studies show different designs to manipulation the phase of the emitting light by guided SPPs. In one approach, the planar plasmonic lens is formed by cross-shaped aperture arrays [28, 31], as shown in Figure 1.12 (a). The phase and the amplitude of the wavefront are modified by changing the arm lengths of the cross-shaped apertures, as seen in Figure 1.12 (b). Thanks to the 2D controlling of the phase in the metal plane, a 3D focusing is achieved and record by CSOM, shown in Figure 1.12 (c). A focus size of $2.3 \mu\text{m}$ with the focal length $16 \mu\text{m}$ is characterized, while the lens is under linearly polarized incidence at the wavelength of 850 nm .

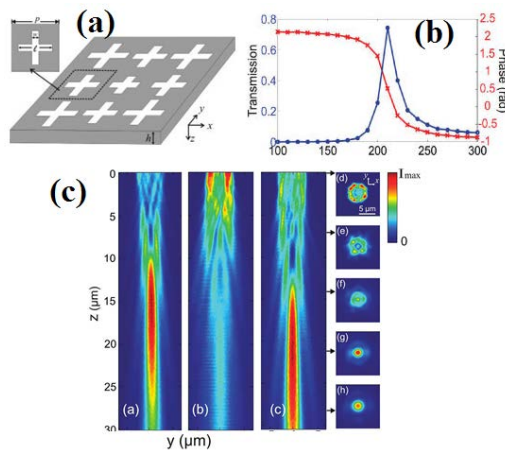


Figure 1.12 (a) Schematic of the planar plasmonic lenses formed by variant cross-shaped aperture arrays. (b) The transmission efficiency (red solid line) and phase (blue dotted line) of the transmitted field as function of arm length at the

working wavelength. (c) Measured axial intensity profile (in the y-z plane) of light passing through [28].

Besides the focal size and focal length, transmission coefficient is also an important property of a focusing lens. There are some researches investigate the transmission coefficient of diffractive plasmonic lenses [30, 84]. In those researches, periodic plasmonic structures are applied, as shown in Figure 1.13 (a) and (b). While the periodicity satisfies the equation [84]

$$k_{spp} = k_0 n \sin \phi + q k_g \quad (1.4)$$

where k_0 is the wavevector in free space, k_{spp} is the wavevector of the SPP wave, ϕ is the angle of incidence, n is the refractive index of the dielectric media, q is an integer, and k_g is the reciprocal vector of the grating periodicity Λ ($k_g = 2\pi/\Lambda$), the transmission of the plasmonic lens will be enhanced. As shown in Figure 1.13 (c), while the plasmonic lens is working at the wavelength described by the equation (1.3), the transmission of the system will be enhanced.

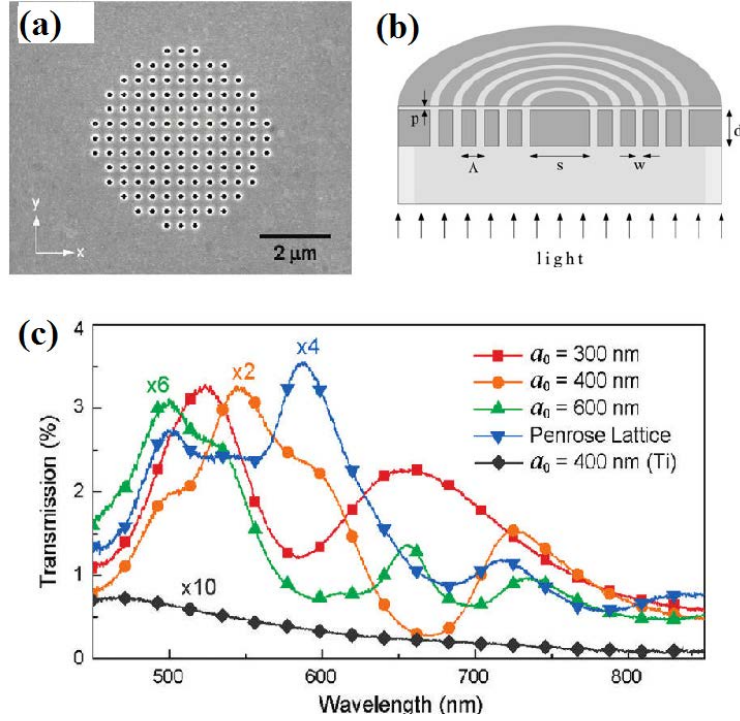


Figure 1.13(a) SEM image of a 5 μm patch of nanoholes with 400-nm period [30]. (b). nanolens made of periodical concentric silver rings[84]. (c) Surface plasmon resonances were tuned by changing the lattice geometry[30].

1.2.2. Plasmonic structures with radially polarized light

In all the studies about plasmonic lens mentioned above, only linearly polarized incidence cases have been considered. Nevertheless, other studies [34-39, 85-88] have shown that radially polarized incidence will significantly improve the focusing capability of plasmonic lens. This is first noticed in an evanescent Bessel beam generation study [85]. The setup is shown in Figure 1.14. As can be seen, a radially polarized light is focused by an aplanatic lens and illuminates onto a silver film. The focused light contains components with various incident angles. At certain incident angle SPP will be generated. Because the radial symmetry, all the generated SPPs will be guided into the center of the optical axis. According to the numerical simulation, a Bessel function field distribution will be found, as shown in Figure 1.15

(a). Compared with linearly polarized light situation (Figure 1.15 (b)), the radially polarized incidence will not only enhance the intensity at the focus but also presents a single focus with even smaller focus size at the center. The focus size, or in the other word full width at half maximum (FWHM), depends on the Bessel function solution will be as small as $0.219\lambda_0$, where is λ_0 the wavelength of the incident light. Despite the setup in this study is not a strictly plasmonic lens since the traditional aplanatic lens plays the role of focusing, it shows the advantage to apply radially polarized light into plasmonic focusing structures.

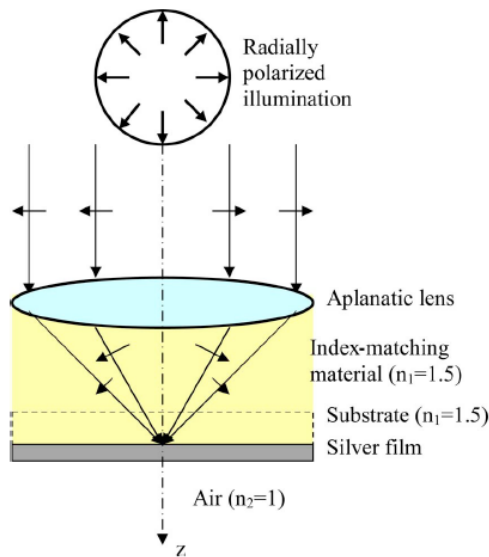


Figure 1.14 Diagram of the proposed setup for evanescent Bessel beam generation[85].

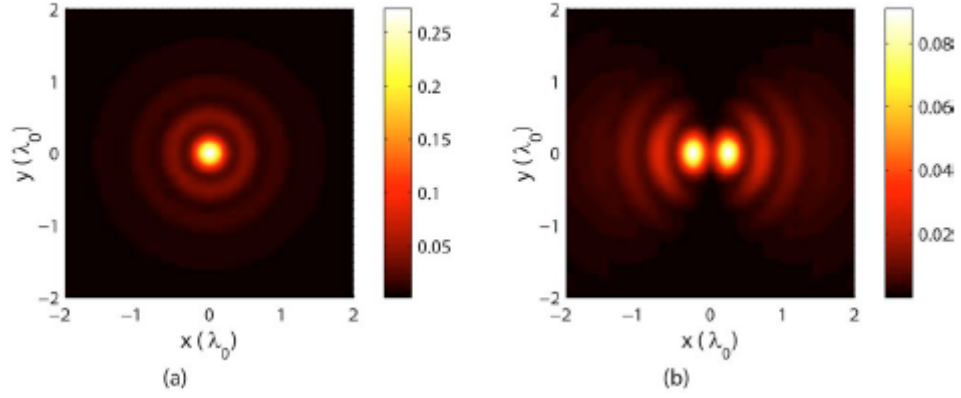


Figure 1.15 Numerical simulation results for (a) total field strength at the bottom of the silver layer for radial polarization, (b) total field strength at the bottom of the silver layer for linear polarization illumination as a comparison[85].

After that, the enhanced focusing capability of plasmonic lens with radially polarized incidence has been demonstrated in studies[34, 35]. As illustrated in Figure 1.16 [35], a single ring slit plasmonic lens under different polarization incidence will behave differently. While under radially polarized incidence, the in-plane electric field E_R will vanish at the center of the lens due to destructive interference, since the phases of E_R at the opposite edges are with 180° difference. However, for out-of-plane electric field E_z , which is the dominating component for SPP field, there will be constructive interference at the center. The ratio of $|E_R|$ and $|E_z|$ depends on material properties of metal and dielectric, by $|E_z|^2/|E_R|^2 = |\epsilon_M/|\epsilon_D|$ where ϵ_M and ϵ_D are the permittivities of metal and dielectric respectively. In the optical range, $|\epsilon_M|$ is usually about one order larger than $|\epsilon_D|$. Thus there will be a single focus from the constructive interference at the center of the lens for the overall effect. Moreover, due to the radial symmetry, the field distribution has a zero order Bessel function profile, which gives a very small focus size. On the other hand, the case of linearly polarized incidence is just the reverse, where E_R constructively interference and $|E_R|$ destructively

interference at the center. Two focus spots across the center along the direction of the polarization will be found.

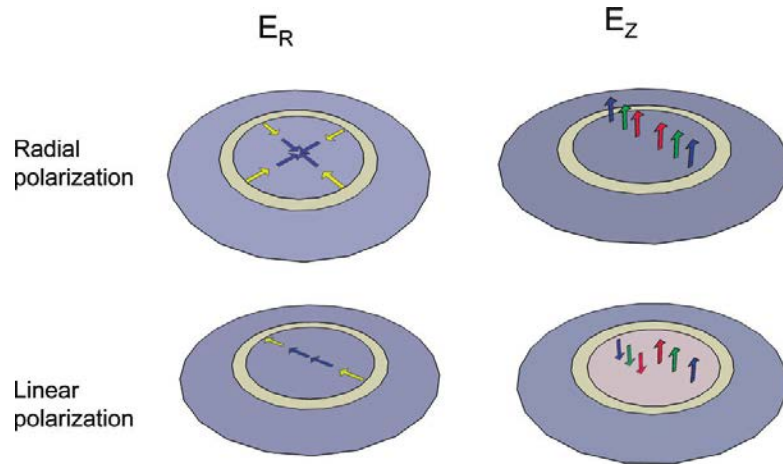


Figure 1.16 Schematic diagram showing the geometry of the plasmonic lens and the orientation of the field components under radial and linear polarization illumination[35].

For the experimental demonstration [35], a single ring plasmonic lens with the diameter of 15 μm is fabricated on a 150 nm thick Ag film deposited on glass substrate. A radially polarized light with the wavelength of 1064 nm has been illuminated in the NSOM scanning measurement. The wavelength is chosen intentionally that the ratio $|E_Z|^2/|E_R|^2$ is large enough to overcome the shortage of NSOM system whose coupling coefficient for E_R is larger than for E_Z . By doing so, the field distribution scanned by NSOM will match the profile of the overall intensity profile. The NSOM scanning result for radially polarized light incidence has been shown in Figure 1.17. Compared with the case of linearly polarized incidence, shown in Figure 1.18, a single focus with strong intensity has been achieved by radially polarized light.

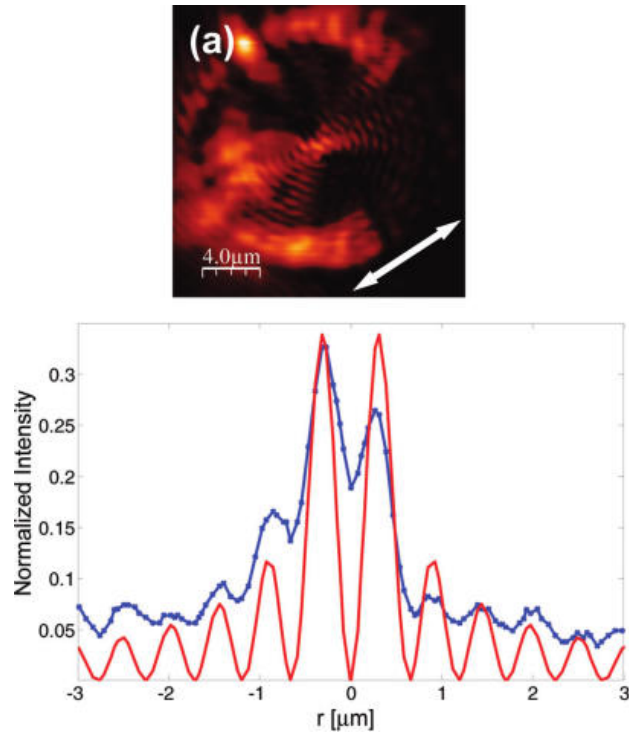


Figure 1.17 NSOM measurement showing SPP focusing in the plasmonic lens illuminated by linearly polarized light[35].

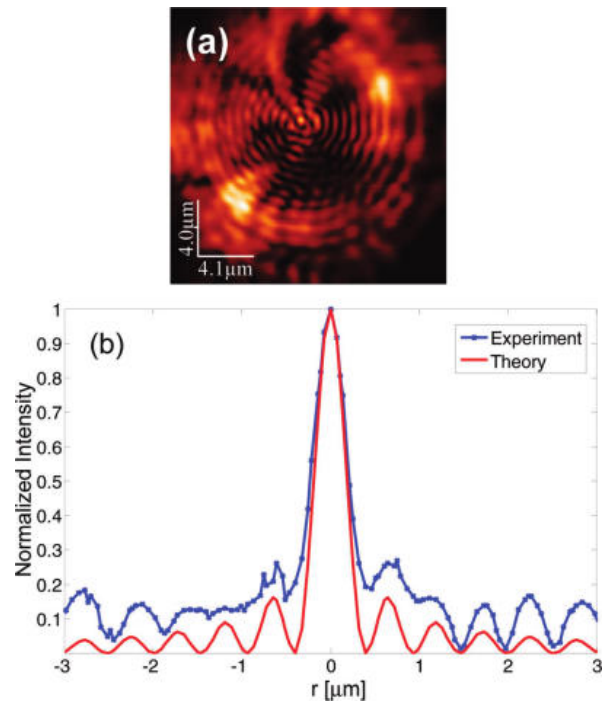


Figure 1.18 NSOM measurement showing SPP focusing in the plasmonic lens illuminated by radially polarized light[35].

Despite the advantages that radially polarized incidence can bring to plasmonic lenses, it is not easy to generate radially polarized light. There are many kinds of methods to generate radially polarized light; nevertheless, we can roughly classify them into three categories.

The first kind of methods is based on resonator configurations in laser cavities [42, 89, 90]. For example, in a resonator, the coherent summation of two orthogonally polarized modes can lead to both azimuthally polarized light and radially polarized light by changing different mode combinations, as shown in Figure 1.19 [42].

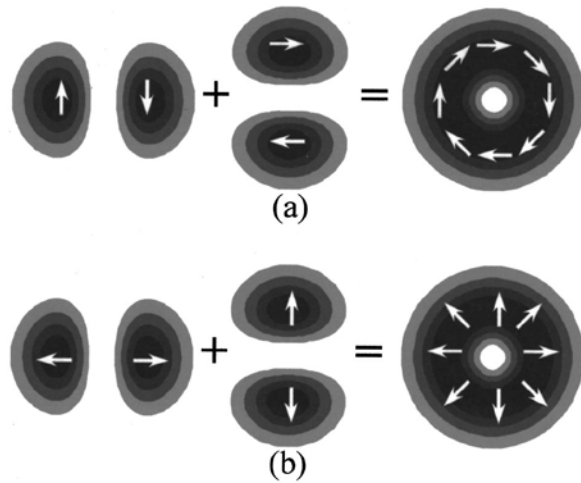


Figure 1.19 Coherent superposition of two orthogonally polarized modes to form azimuthally and radially polarized beams; (a) azimuthally polarized doughnut beam; (b) radially polarized doughnut beam[42].

The second kind of methods is to spatially control the polarization direction and phase by different ways [43, 44, 46, 47, 91]. As an illustration, the spatial polarization direction can be modified by half-wave plates [46], shown in Figure 1.20. A spatially varying retarder (SVR) which is composed of 8 half-wave plates in different directions can control the polarization direction through each wave plate and eventually transform a linearly polarized light into radially polarized light. The same

kind of spatially polarization modulation can also be achieved by space-variant subwavelength gratings[43, 44], combination of spatial light modulators[47], arranged liquid crystal molecules[91].

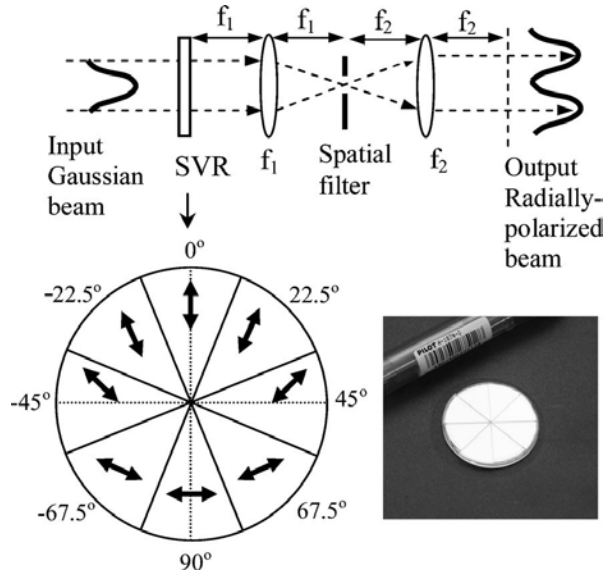


Figure 1.20 Arrangement for transformation of a linearly polarized Gaussian beam to a radially or azimuthally polarized beam. The insets show the SVR scheme, together with an SVR photo [46].

The third kind of methods is to utilize the polarization selective configurations to filter out the light with local polarization direction different from radially polarized light. A conical Brewster prism [45], as shown in Figure 1.21, will filter out light with one particular polarization, since the conical angle satisfies Brewster condition for all the light incidence parallel to the optical axis. Moreover, because of its axial symmetry, the output light will be radially polarized.

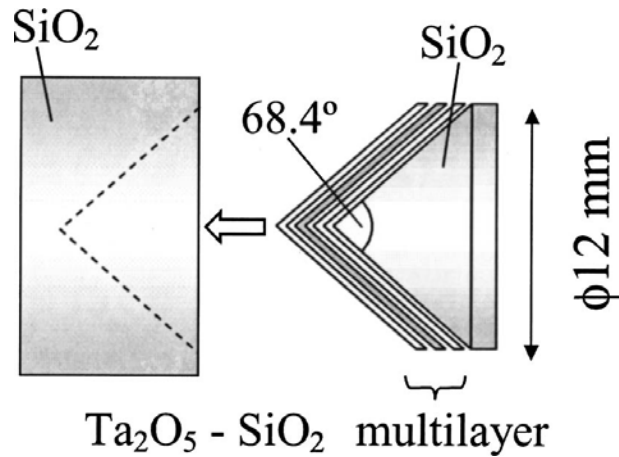


Figure 1.21 Drawing of the conical Brewster prism[45].

The subwavelength concentric metallic gratings work in a similar way[48]. A grating with a subwavelength period will strongly reflect TE polarized light and allows TM polarized light to transmit through. For the concentric metallic gratings, all the light with TE polarization respect to the grating will be filtered out. The transmitted light with TM polarization respect to the grating is actually radially polarized light.

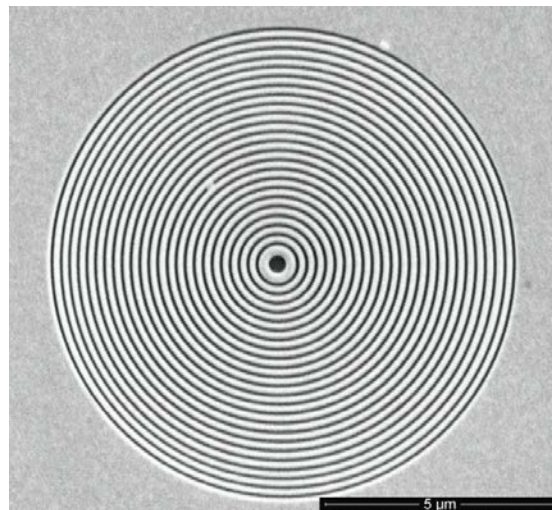


Figure 1.22 SEM images 20 periods of concentric metallic rings[48].

Most the above-mentioned methods to generate radially polarized light are complicated and require precise alignment. Even more, it will require another precise

alignment when it is applied to the plasmonic structures, such as plasmonic lens we have previously discussed.

1.2.3. Plasmonic structures for sensor miniaturization

For decades, sensor miniaturization has drawn people's attention in a broad range of sensing fields for physical, chemical and biomedical parameters, because the scope of researches focuses into smaller and smaller scale. It becomes an even more important matter, after the booming of nanotechnologies. However, as the size of the optical components goes as small as the operating wavelength, it suffers from the same size difficulty as in the miniaturized imaging system due to diffraction limit. Nevertheless, recent researches suggest that plasmonic structures have the potential to shrink the size of optic components to an even smaller scale with their capability of confining and manipulating light at subwavelength.

The first surface plasmon resonance (SPR) based sensor was demonstrated by Nylander and Liedberg [92-94] and was applied to gas detection and biosensing. After that, SPR based sensors were widely investigated, especially in the measurement of chemical and biological parameters due to the high sensitivity, label-free advantage and ultra-thin thickness.

As discussed previously, SPP cannot be excited by the free space incidence on the smooth metal-dielectric surface because of the momentum mismatch (see Eq. 1.5). Therefore, people conceived many different configurations to introduce SPR. Figure 1.23 shows the three commonly used configurations of SPR sensors. The basic idea is to increase the momentum of the incident light to match the momentum of SPP, which is achieved by attenuated total reflection [Figure 1.23 (a)], diffraction

grating at the metal surface [Figure 1.23(b)] or waveguide structures [Figure 1.23]. Once SPR is excited, strong field concentration is found in the evanescent region at the interface. The strong field enhancement results in the high sensitivity to the environment refractive index change. Thus the environment media change can be monitored by the SPR wavelength shift or the optical intensity at the resonance wavelength.

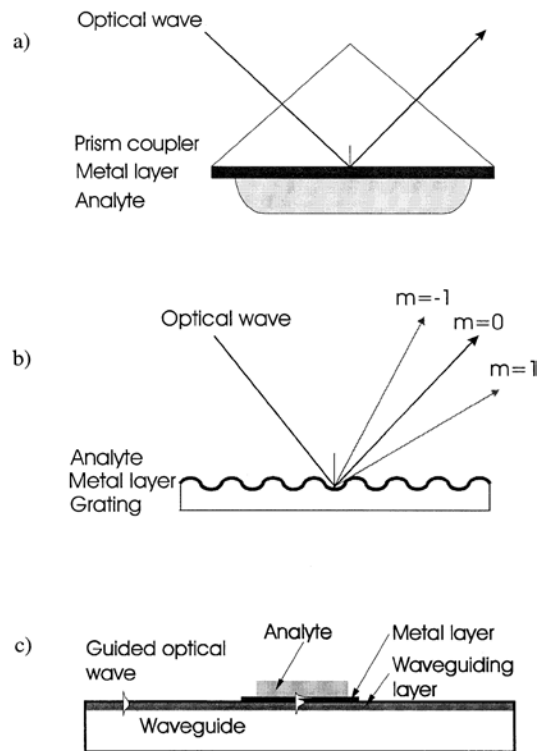


Figure 1.23 three commonly used configurations of SPR sensors: (a) prism coupler-based SPR system; (b) grating coupler-based SPR system; (c) optical waveguide-based SPR system [53].

Sensors based on localized surface plasmon (LSP) have also been investigated [43]. For LSP cases, light interacts with material in the scale which is determined by the geometric size of nanoparticles. Plasmon oscillation is locally confined in the area near the nanoparticle, shown in Figure 1.24. Since the nanoparticle size can be far smaller than the wavelength, LSP based sensor are often used to enhance the lateral

spatial resolution [95, 96] of sensing. In addition to measuring LSP resonance directly, LSP was found essential to enhance Raman scattering due to its highly localized field enhancement, which is called surface-enhanced Raman spectroscopy (SERS) [54, 97]. With SERS, not only the environment refractive index but also the type of molecules can be measured.

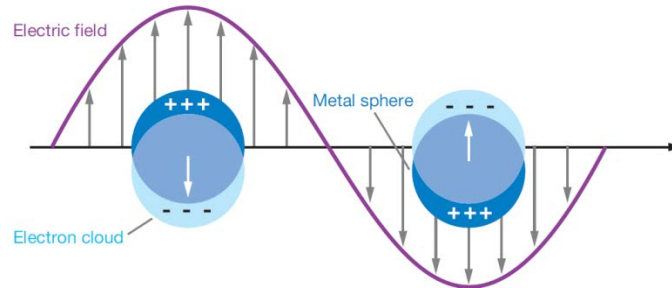


Figure 1.24 Schematic diagrams illustrating a localized surface plasmon[54].

Plasmonic interference, SPP interference at the metal/dielectric interface, has been widely studied in recent decades after the investigation of SPP behaviors [98-101]. Taking two-slit plasmonic interference for example, SPPs, generated at the slits while the slit scattering provides the extra momentum, interference at the metal/dielectric interface, as shown in Figure 1.25. And eventually the plasmonic interference will affect the intensity distribution in the near-field [98, 100, 102] as well as the transmission or reflection spectra [98, 99].

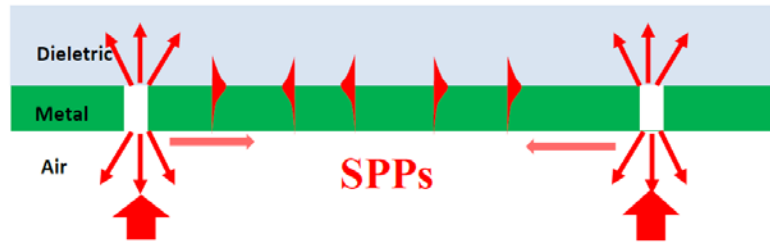


Figure 1.25 Schematic diagrams illustrating two-slit plasmonic interference at metal/dielectric interference

After that, plasmonic interference has been used for sensing purpose [55, 103].

As an example, a plasmonic interferometer is fabricated on a 300-nm thick silver film deposited on a glass substrate, shown in Figure 1.26 (a). The interferometer contains two shallow grooves and one slit in the center. SPPs generated at the grooves interfere and transmitted through the slit. Since SPP is sensitivity to environment refractive index, the interference spectra will respond to the media refractive index both in wavelength and relative intensity Figure 1.26 (b).

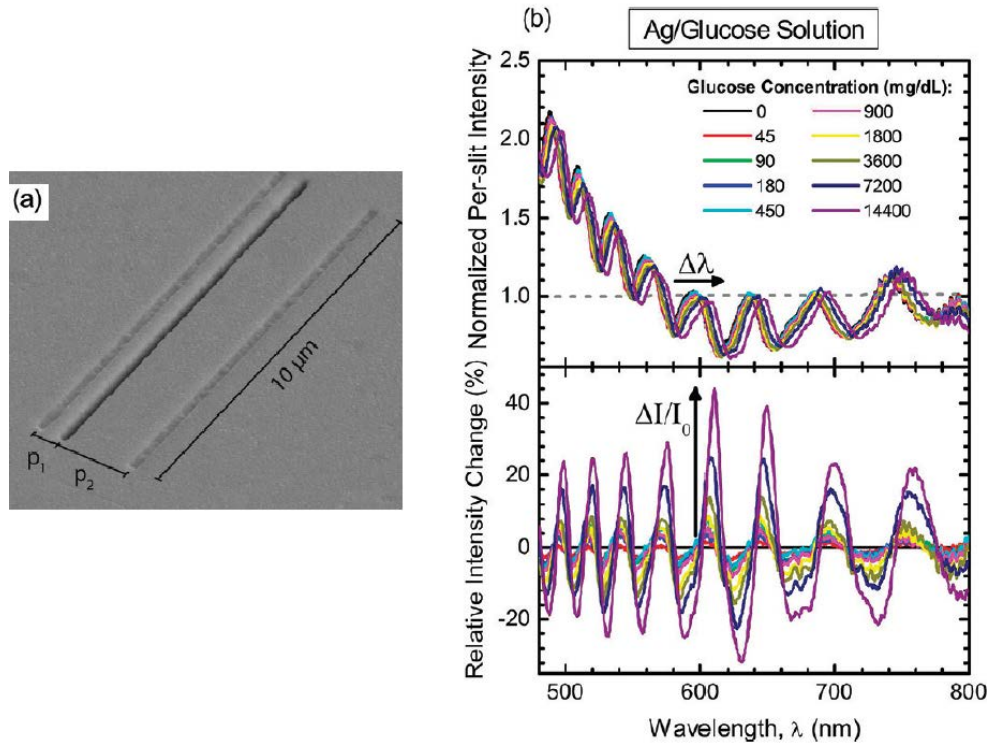


Figure 1.26 (a) SEM micrograph of a groove-slit-groove (GSG) plasmonic interferometer. (b) Normalized per-slit transmitted intensity spectra and relative intensity change of the plasmonic interferometer measured at various concentrations of glucose in water[55].

In terms of sensor miniaturization, the facet of an optical fiber tip is recently found to be an appealing platform to integrate photonic structures for sensing applications [56, 57, 104-106].

A typical design is shown in Figure 1.27 (a). A dielectric and metallic photonic structure is integrated on the tip of fiber, which significantly improves the field confinement due to enhanced LSP resonance, seen in the inset of Figure 1.27 (b). The reflectance dip of LSP resonance shown in Figure 1.27 (b) enables a refractive index sensitivity of 120nm per refractive index unit (RIU). Additionally, this sensor shows the potential to detect the pressure change due to the low Yong's modulus of the positive photoresist ZEP.

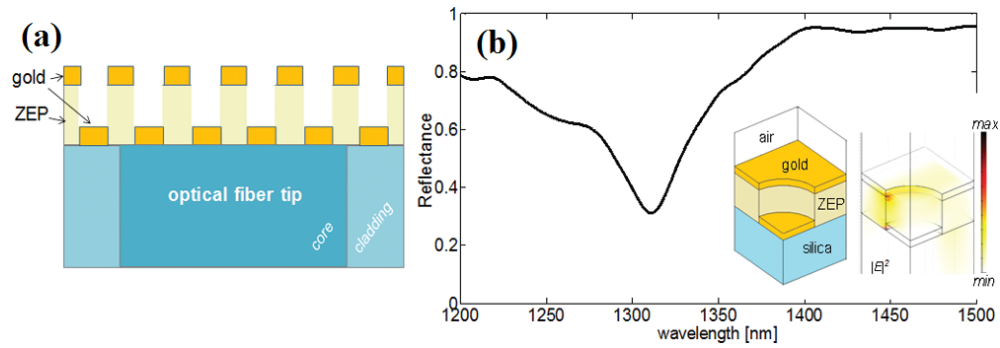


Figure 1.27 (a) Schematic (cross section view) of the hybrid metal-dielectric structure for enhancing LSP integrated on the optical fiber tip. (b) Measured reflectivity and calculated electric field intensity distributions[56].

Although researchers started to integrate plasmonic structures on fiber for sensing application, to date all of these sensors are either limited to single parameter sensing, or can be sensitive to multiple parameters but are not capable of distinguishing different parameters.

1.2.4. Fiber optic sensors based on cladding modes and buffer-guided modes

In FBG fibers, there are discrete dips can be found below the Bragg wavelength in the transmission spectra, which are due to the coupling between core modes and cladding modes. Although the cladding modes shown in the spectra are undesirable in optical communications, it turns out that they can serve as good sensors for environmental parameter changes, such as refractive index [61], and temperature [107].

It is found that cladding modes are generally more sensitive to the environmental changes than core modes. That is because the mode fields of cladding modes can extend to the media, whereas the mode fields of core modes are confined in the core region, and covered by the cladding. Take the refractive index sensing as a comparison. Through holes from the media to the core region are typically required

for the refractive index sensors based on core modes. For example, for the sensor as shown in Figure 1.28, a microhole array in a single-mode fiber (SMF) is fabricated by selective chemical etching of femtosecond-laser-induced FBG. Thanks to the through holes, the refractive index can be directly detected by the Bragg resonant wavelength shift. Despite the fabrication difficulty of the through holes, the sensor demonstrates a refractive index sensitivity of 5.484nm/RIU, which is among the highest sensitivity for fiber optic sensors based on core modes.

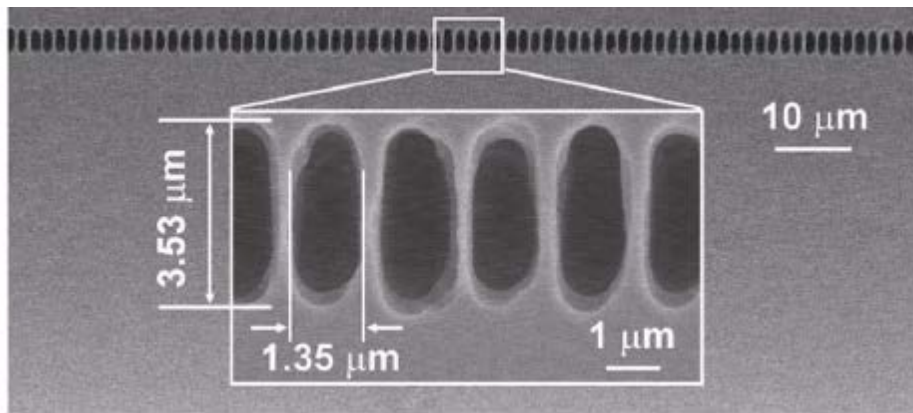


Figure 1.28 SEM image on the fiber grating surface after etching[108].

Fiber optic sensors based on cladding modes, on the other hand, show much larger refractive index sensitivities. A typical fiber optic sensor based on cladding modes is shown in Figure 1.29. The cladding of a SMF is chemically etched to a smaller diameter, which gives three advantages for refractive index sensing: 1) the coupling strength between core modes and cladding modes is enhanced, 2) the number of the cladding mode resonances is greatly decreased to be easily discriminate in the spectra, 3) more cladding mode field can extend into the media. The maximum sensing sensitivity of 172 nm/RIU is found in this sensor which is two orders larger than those fiber optic sensors based on core modes.



Figure 1.29 Structure of etch-eroded FBG for ambient refractive index sensing[109]

In the history of sensors based on cladding mode coupling, long-period fiber gratings (LPFGs) are first used for sensing applications for temperature, strain, and refractive index [60, 110-112]. LPFGs scatter the core modes into cladding, and couple the co-propagating cladding modes with co-propagating core modes thanks to LPFGs' small grating vectors. As a result, the cladding modes can be easily observed in the transmission spectra and used to measure the environmental parameters. A typically transmission spectrum of an LPFG is shown in Figure 1.30. As a comparison, the standard FBG or short-period fiber grating (SPFG) support the coupling between core mode and contra-propagating cladding modes, yet show weaker cladding mode coupling in the spectrum (see Figure 1.31 for example). Despite the large cladding mode coupling coefficient from LPFGs, the sensor based on LPFGs are limited by the lateral resolution, especially when it comes to the local parameter measurement, because the overall length of a LPFG is typically centimeter long.

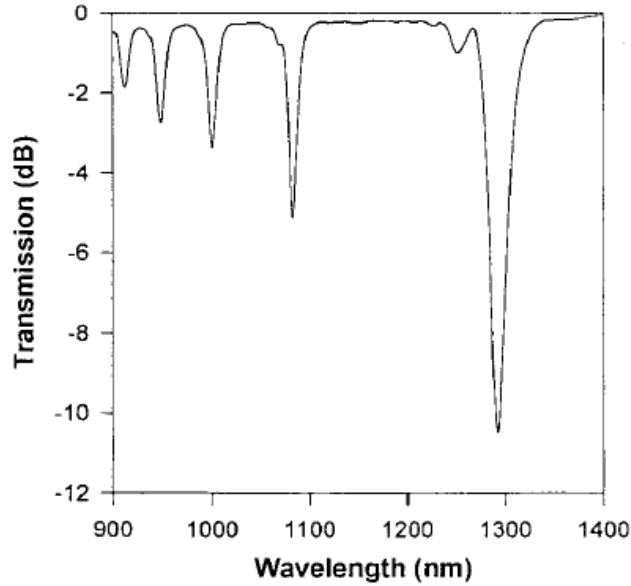


Figure 1.30 Experimentally measured transmission spectrum of an LPFG with a period of $198 \mu\text{m}$ [112].

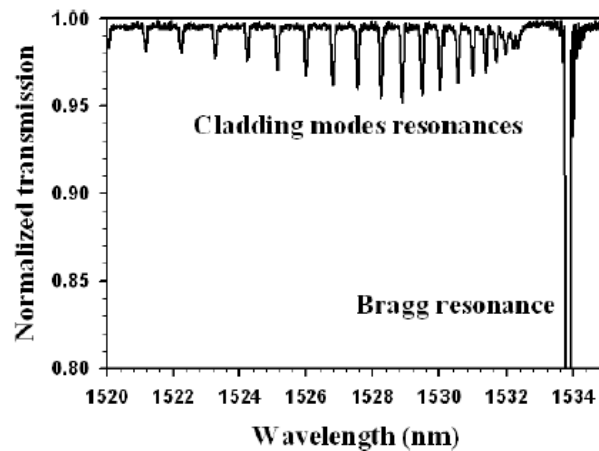


Figure 1.31 Experimentally measured transmission spectrum of a 8 mm long standard FBG photo-written in a single-mode step-index optical fiber [61].

In that case, SPFGs are preferred to miniaturize the size of sensors. And tilted short-period fiber Bragg gratings (TFBGs) are introduced to take the advantages of both small size and large coupling coefficient. As shown in Figure 1.32, Bragg gratings in the fiber are tilted. Thus more light can be reflected into the cladding, and

strong cladding modes can be characterized in the transmission spectrum, shown in Figure 1.33.

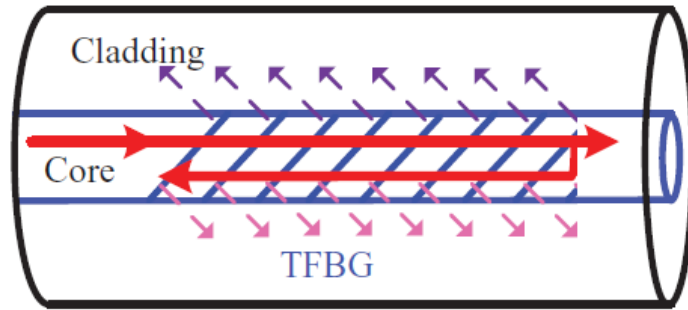


Figure 1.32 Schematic of a TFBG.

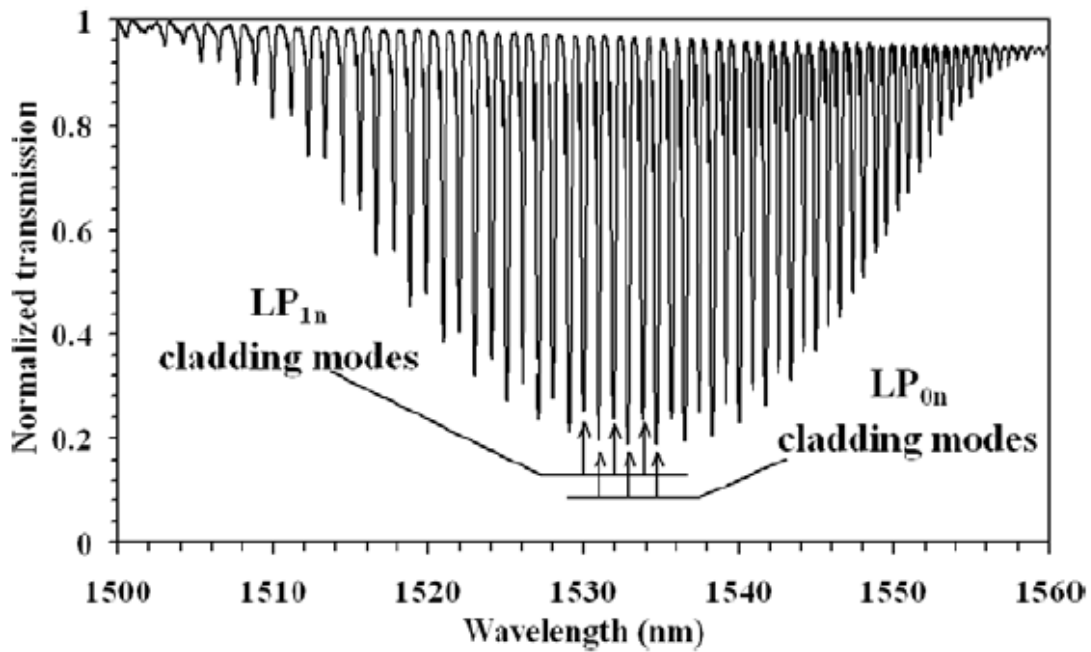


Figure 1.33 Experimentally measured transmission spectrum of a 8 mm long $\theta = 16^\circ$ -tilted TFBG surrounded by air[61].

Other than FBGs, other methods were also developed to generate cladding modes for sensing applications. One commonly used idea is to fuse the fibers in different core diameters [107, 113, 114]. As shown in Figure 1.34, one piece of fiber is aligned and spliced into a fiber with different core diameter. Due to the core diameter mismatch at the splicing boundary, the core modes can be scattered into the

cladding and coupled back to the core at the other boundary. Therefore a Mach-Zehnder interferometer is formed and can be used to measure parameters such as temperature, strain and refractive index. This configuration can use any combination of fibers with different diameters, depends on different applications, such as SMF with multimode fiber (MF) for high temperature measurement [107], SMF with photonic crystal fiber (PCF) for Simultaneous temperature and force measurement, and singlemode-multimode-thinned-single-mode fiber structure for temperature, strain and refractive index sensing.

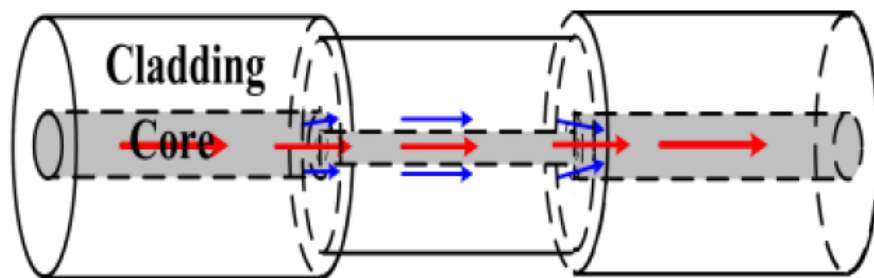


Figure 1.34 Schematic of cladding mode generated by core diameter mismatch.

Another method to generate cladding mode is to taper a fiber, which is the same in principle with the method of core diameter mismatch. As an example in Figure 1.35, one 3 dB taper is made by a fusion splicer in a SMF. Core modes can be scattered into cladding modes, travel along the fiber, be reflected by the gold coating and eventually coupled back to the core modes again, which forms a Michelson interferometer to sense different immersion length as well as the refractive index. The tapered fiber structure was later integrated with a TFBG to generate strong cladding modes and serve as an accelerometer [115] and a 3D inclinometer [116].

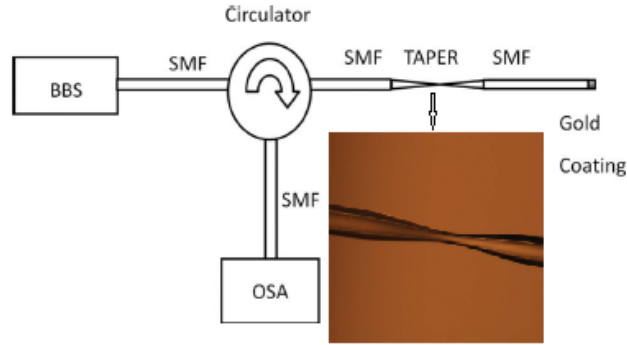


Figure 1.35 Taper-based SMF Michelson interferometer[63].

For all the methods mentioned above to generate cladding modes for sensing applications, the sensors are still either suffering from large size (FBGs), or weak coupling coefficient (core diameter mismatch and tapered structure).

On the other hand, unlike cladding layer, buffer layer of optical fibers was less studied, since it typically only serves as a mechanical protection to the glass surface. However, when an optical fiber is bent, the guided light in the core region can penetrate to the cladding and buffer regions, and later recouples coherently to the core mode, forming WGMs[68]. As showing in Figure 1.36 (a), light in the core can penetrate from the core region into buffer layer through the cladding layer thanks to the large bending of the fiber. It forms guided mode in the buffer region and can be observed in the spectrum such as shown in Figure 1.36 (b).

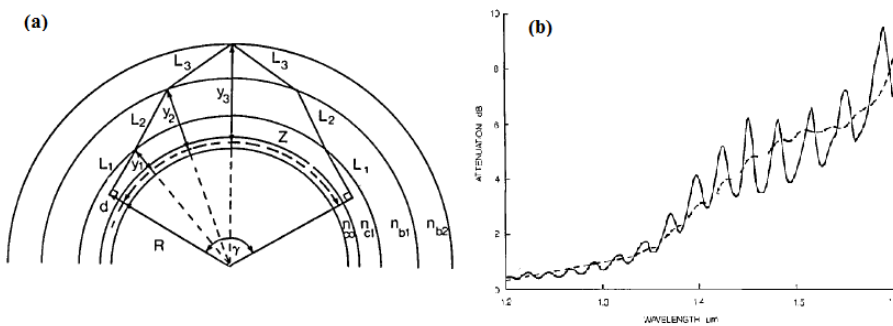


Figure 1.36 (a) Geometry of the WGM interference model. (b) Bend loss as a function of wavelength for the fiber with WGM. [68]

Different from core modes and cladding modes which are confined in the glass materials, buffer guided modes can be more sensitive to temperature and strain because of the polymer property of the buffer layer. For instance, a highly sensitive temperature sensor is achieved by exciting WGM in a coated single-mode fiber loop [73]. They test the looped SMF in the temperature controlled oven shown in Figure 1.37 (a). Seen from Figure 1.37(b), large sensitivities up to $-5.22\text{nm}/^\circ\text{C}$ have been observed, and different buffer coatings result in different temperature response.

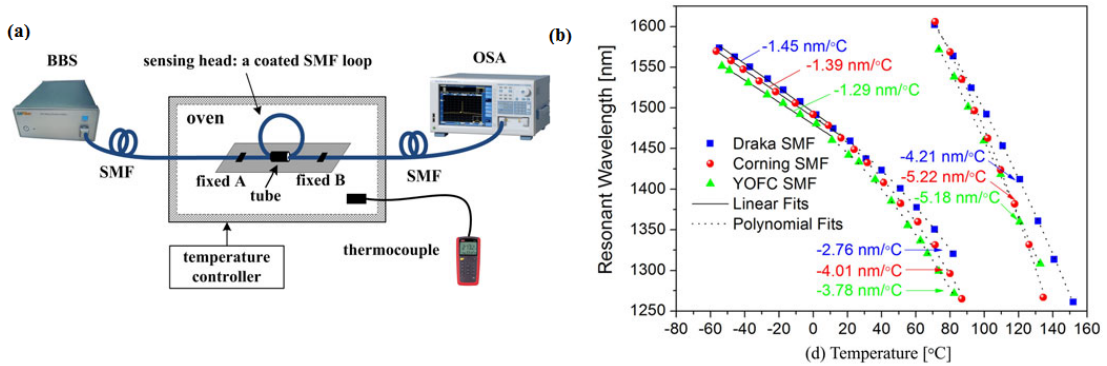


Figure 1.37 (a) Experimental setup for testing the coated-SMF loop temperature sensor. (b) The temperature response of the three types of coated-SMF loop sensors [73].

In terms of strain sensing, a large strain sensitivity up to $-1.76\text{ pm}/\mu\epsilon$ has been achieved by utilizing the polymer material property of polymer optical fibers (POFs) [117], which is more sensitive than most of the strain sensors based on core modes and cladding modes. However, POFs are more expensive than regular SMFs and lack of multi-parameter sensing ability.

1.3. Motivation for this doctoral research

Although it was a quite success to achieve sub-diffraction limit resolution by the help of SPP at the metal/dielectric interface, the physical limits of plasmonic lenses in

the diffractive regions as well as a clear definition of the boundaries of different regions for plasmonic lenses are still under-investigated. To enhance the understanding of how plasmonic lenses help imaging systems, this dissertation seeks to answer the following important but unexplored questions: 1) how to define different regions of plasmonic lenses, 2) what are the physical limits in each different region, 3) how to utilize plasmonic behaviors to enhance the resolution in the diffractive region.

Further, another goal of this dissertation is to study how to use nanophotonic structures to easily generate radially polarized light and integrate it with plasmonic lenses to enhance imaging. Although there are many methods to excite radially polarized light, they are relatively complicated and often require precise alignment with lens systems to enhance the focus resolution.

In the perspective of sensing, many nanophotonic structures mentioned above have been studied to miniaturize the systems and enhance the sensing performance. Nevertheless, they are either still in relative large sensor sizes or lacking of multi-parameter sensing capability. In this dissertation, we want to use the nanophotonic structures at the tip of the fiber to minimize the sensor size and achieve multi-parameter sensing capability with high sensitivities.

In addition to that, for all the methods mentioned above to generate cladding modes for sensing applications, the sensors are still either suffering from large size (FBGs), or weak coupling coefficient (core diameter mismatch and tapered structure). We want to easily excite cladding modes and buffer-guided modes simultaneously in optic fibers with the nanophotonic structures at the fiber facet, which will enhance the

coupling coefficient, increase the sensor performance and enable multi-parameter sensing capability.

1.4. *Objectives and scope of the dissertation*

The overall goal of the dissertation work is to achieve a better understanding of selected nanophotonic structures and use this understanding to study how to design miniature imaging and sensing systems with enhanced performance. Specific objectives include the following:

- 1) Develop an enhanced understanding of plasmonic lens through theoretical investigation into the physical limits of focusing in different regions, and formulate the design guidelines in each region.
- 2) Design and optimize a plasmonic lens working around Fresnel region, and study its subwavelength focusing ability by using numerical simulations.
- 3) Study the radially polarized light generated by using transverse electromagnetic (TEM) resonance in annular plasmonic structures and its application for improving plasmonic lens in the surface plasmon dominating region.
- 4) Design and fabricate a plasmonic interferometer on a fiber facet and experimentally study its ability of multi-parameter sensing.
- 5) Develop a novel method that utilizes gratings on fiber facets to generate cladding modes and buffer-guided modes simultaneously and study these structures for multi-parameter sensing.

1.5. *Organization of the dissertation works*

The rest of this dissertation is organized as follows. In Chapter 2, a classification of plasmonic lenses in different regions is provided, along with the study of physical limits of plasmonic lens design in different regions. After that, sub-diffraction-limit plasmonic lens in Fresnel region is discussed. In Chapter 3, the study of radial polarization generating based on TEM mode resonance in plasmonic structure is presented. A plasmonic structure with the ability to generate radially polarized light with normal incidence is demonstrated. Later, plasmonic lens designed in the near-field with dielectric layer deposited and plasmonic lens self-aligned with radial polarization generating structure are investigated. In Chapter 4, the study of an on-fiber plasmonic interferometer for the application of multi-parameter sensing is provided. In Chapter 5, the study of cladding modes and buffer-guided modes generated by gratings on fiber facets is conducted. A summary of the proposal, as well as an outline for future work, is provided in Chapter 6

Chapter 2. Plasmonic lens in different regions

2.1. *Plasmonic lens overview*

The ability to focus light into a smallest achievable spot has always been of great interest. However, in traditional practice using dielectric lenses, the focal size is inevitably limited by the Abbe's diffraction limit $(0.51f\lambda/\rho)$ [52]. Here, λ is the wavelength in vacuum, and f and ρ are the focal length and radius of the lens, respectively. Moreover, the performance of conventional spherical lenses deteriorates as their sizes approach the wavelength. Recent progress in surface plasmon polariton (SPP) has provided promising solutions to achieving compact photonic devices through manipulation of SPPs [11]. Since first discovered by Ritchie [8], SPP, which is defined as the coupling of the collective electron excitation with the incident light at the metal and dielectric interface, has been widely studied. One of the most tantalizing prospects of SPPs is their ability to focus light energy into a nanoscale volume [118]. Recently, much attention has been focused on utilizing the plasmonic property of nanoscale structures [119], to improve the performance of light focusing. Although it was a great success to improve optical resolution by SPP at the metal/dielectric interface with matching the material permittivity [18-21, 25], or with the help of photonic metamaterials[22], these approaches usually require additional launching for SPP. Furthermore, people investigated plasmonic structures which can directly couple light to SPP to enhance the imaging properties, namely plasmonic focusing lenses [4], With enhanced focusing properties, plasmonic focusing lenses are

expected to have great potential in applications such as microscopy, sensing, and nanofabrication.

Plasmonic focusing in different regions exhibits different physical behaviors. However, in previous efforts on developing plasmonic lenses, the effect of different regions on the performance of a plasmonic lens has not been thoroughly studied, especially for lenses working in a region that diffraction behaviors dominate the focusing phenomenon. Recently, the importance of the diffraction behaviors in different regions of plasmonic lenses has been realized due to the observation of a mismatch between the designed focal lengths and the experimentally obtained values [120, 121]. In addition to the focal length, the physical limits of the focus size, which is a vital aspect of plasmonic focusing, have never been studied. Worth to mention, although the Talbot effect, or self-focusing effect, has been investigated to enhance the resolution in the diffractive region, it only works on grating structures [122, 123].

In this chapter, we first define three different regions for plasmonic focusing of the plasmonic lens, followed by a theoretical investigation into the physical behaviors of plasmonic lenses in these three different regions. Furthermore, with a goal of achieving sub-diffraction-limit focus size, a specific plasmonic lens with multiple concentric ring structures is investigated. It is expected that this work will help achieve a better understanding of the physical behaviors of plasmonic focusing and provide a basis for plasmonic lens design in different regions.

Plasmonic lenses can be developed in both near-field and far-field. Here, we consider a linear polarized light with normal incident on a plasmonic focusing lens with an aperture size of ρ . Depending on the distance d from the lens exiting pupil,

we define three different regions for plasmonic focusing, namely, SPP dominating region, Fresnel region, and Fraunhofer region, as illustrated in Figure 2.1 Schematic of plasmonic focusing in three different regions. In the reactive near-field region, where SPP dominates the field distribution, the range of the near-field affected by SPP can be determined by the attenuation length of SPP (l_{zd}) in the direction normal to the interface of a metal and a dielectric. In this region (i.e., $0 < d < l_{zd}$), due to the large wavenumbers of SPPs, subwavelength focusing and energy confinement can be achieved by obtaining interference of SPPs [12]. Many efforts have been made to further improve the focusing performance in this region, such as employing radially polarized incident light [35] and introducing asymmetric surface structure [124].

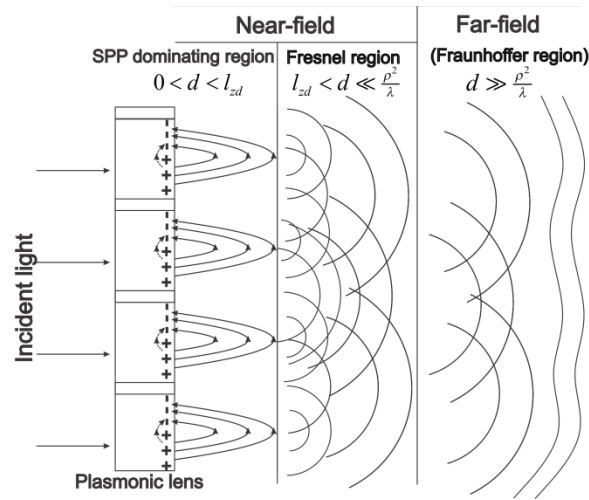


Figure 2.1 Schematic of plasmonic focusing in three different regions

Beyond the SPP dominated region, in those regions that are further away from the lens surface, diffraction behaviors will dominate the focusing phenomenon. In the Fresnel region, which is the farthest part of the near-field (i.e., $l_{zd} < d < \rho / \lambda^2$), the diffraction pattern is relatively close to the diffraction object and the propagation of the light exiting the lens can be investigated by using Kirchhoff-Fresnel diffraction

theory [52]. In the far-field (i.e., $d > \rho / \lambda^2$), where the Fraunhofer diffraction dominates the lens behavior, the diffraction pattern will be formed in a relatively long distance away from the lens.

2.2. Plasmonic lens in different regions: properties and limitations

2.2.1. Subwavelength focusing in surface plasmon dominating region

The wave vector of SPP under transverse magnetic (TM) incidence (the existence of transverse electric (TE) mode in SPP requires materials with negative permeability, which hardly exists) is given by $k_{spp} = k_0 \sqrt{\varepsilon_d \varepsilon_m / (\varepsilon_d + \varepsilon_m)}$ [125], where k_0 is the free space wave vector, ε_d and ε_m are the permittivity of the dielectric and metal respectively. Note that $|k_{spp}|$ is always larger than $|k_0|$ for the materials that can be found in nature, and thus, the wavelength of SPP (λ_{spp}) is always smaller than λ_0 . We assume nonmagnetic materials (i.e., permeability $\mu = 1$) here, which is applicable to most of the practical cases. The vertical components of wave vectors at the dielectric and metal interface can be determined as

$$k_{zd,zm} = k_0 \sqrt{\frac{\varepsilon_{d,m}^2}{\varepsilon_d + \varepsilon_m}}. \quad (2.1)$$

For a plasmonic lens working in the SPP dominating region, with the help of nanoscale metal structures, free space light can be coupled into SPP at the interface. By tailoring the nanostructure, interference of the energy excitation (i.e., SPPs) can be obtained, which can help achieve energy confinement in a dimension smaller than the diffraction limit of the incident light due to the much smaller wavelength of the SPP.

On the other hand, since SPP is strongly localized around the interface, the energy

density of SPP is much stronger than the propagating light. Therefore, in the SPP dominating region, the field distribution or the focusing effect is governed by SPP.

Since the amplitudes of the electric fields in both dielectric and metal are proportional to $E_{d,m} \propto e^{ik_{zd,m}}$, the attenuation lengths of SPP in the direction normal to the interface can be determined as [126]

$$l_{zd,zm} = |1 / \text{Imag}(k_{zd,zm})|. \quad (2.2)$$

The attenuation length can be used to define the range of the plasmonic dominating region. Since the SPP near-field focusing always happens at the dielectric side in practical applications, the range of the SPP dominating region, as shown in Figure 2.1 Schematic of plasmonic focusing in three different regions, is defined as $d < l_{zd}$.

The SPP attenuation length varies with respect to the incident light wavelength and material properties. As shown in Figure 2.2, which was obtained for a metal (e.g., gold and silver) and air interface, the range of SPP dominated region will increase as the incident light wavelength goes longer, except the anomalous dispersion region near to plasma frequencies. For example, at an incident light wavelength of 808 nm, the distance that characterizes the SPP dominating region at the interface of gold and air can be obtained as 657 nm, which is not a negligible distance compared with the wavelength.

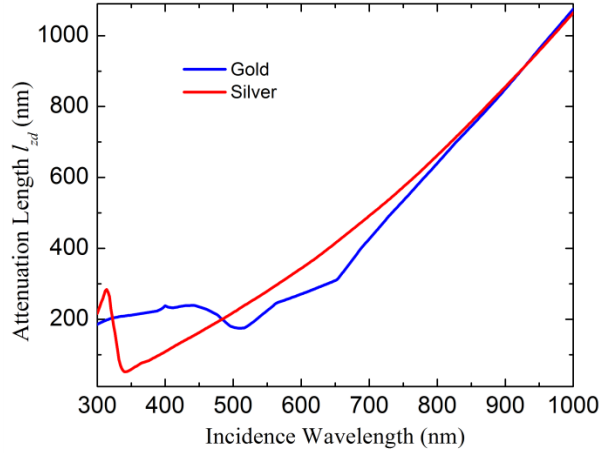


Figure 2.2 Attenuation length (range of the SPP dominating region) of SPP in the dielectric as a function of wavelength. The permittivity of air ($\epsilon_a \approx 1.0$) and the permittivity of gold and silver found in [127] were used.

Since the behavior of SPP dominates the field distribution, the focusing spot size in this near-field region depends on how to manipulate SPP interference on the lens surface. For example, with a single ring structure milled into an optically thick metallic film that is incident by linearly polarized light [12], due to one-dimensional interference of SPP, standing waves can be formed on the metal/dielectric interface along the polarization direction, resulting in one-dimensional focusing along the direction of interference at the center of the ring. The obtained focus size can be as small as $\lambda_{\text{spp}} / 2$. Since in many practical applications, 2D focusing is more desirable, radially polarized incident light can be applied on a plasmonic lens with single or multiple ring structures to achieve 2D focusing on metal/dielectric interface [34, 35]. In this case, the solution to the wave equation of SPP can be obtained in the polar coordinate with a circular symmetry, which takes the form of zero order Bessel function of the first kind; that is, the field distribution is proportional to $J_0(k_{\text{spp}}r)$ [128], where r is the distance to the center of the lens. According to the property of

the zero-order Bessel function of the first kind, the strongest field intensity happens at the center of the ring ($r=0$) and the Full Width at the Half Maximum (FWHM) spot size can be determined when $J_0(k_{spp}r) = 1/\sqrt{2}$, i.e., when $k_{spp}r = 1.13$. Therefore, the focusing spot size can be obtained as $0.36\lambda_{spp}$. Since the SPP wavelength λ_{spp} is always shorter than the optical wavelength λ_0 , the focus size of a plasmonic lens designed in the surface plasmon dominating region can easily be smaller than the diffraction limit. However, the actual size of the focus strongly depends on the SPP wavelength λ_{spp} , in the other word, depends on the material properties of the lens. Based on Eq. (1.1), the shortest λ_{spp} can be achieved when $\varepsilon_d + \varepsilon_m$ is approaching zero. Generally, the imaginary parts of ε_d and ε_m (i.e., $\text{Im}(\varepsilon_d)$ and $\text{Im}(\varepsilon_m)$) are relatively small compared with the corresponding real parts (i.e., $\text{Re}(\varepsilon_d)$ and $\text{Re}(\varepsilon_m)$), and thus can be neglected. Since ε_m has a large negative real part and ε_d has a small positive real part, to obtain a smaller λ_{spp} , a larger $\text{Re}(\varepsilon_d)$ is required. Therefore, high refractive index dielectric should be employed in a plasmonic lens working in the surface plasmon dominating region to obtain a small sized focus.

2.2.2. Plasmonic focusing in Fresnel region and Fraunhofer region

Further away from the SPP dominating region, plasmonic lenses can be designed to work in two different diffraction regions, the Fresnel region and the Fraunhofer region, as shown in Figure 2.1 Schematic of plasmonic focusing in three different regions. In the literature, plasmonic lenses have been developed in these regions to replace traditional refractive index based microlenses or to decrease the

lens size [26-31]. For example, a Fresnel region plasmonic lens with one-dimensional (1D) nanoslit array defined on a metal surface was proposed and studied through numerical simulations [26]. The experimental demonstration of a lens with a similar pattern was reported later by Verslegers *et al* [27]. More recently, two-dimensional (2D) plasmonic focusing lenses were realized in the Fresnel region with chirped circular nanoslits [29] and cross-shaped aperture arrays [28, 31]. Furthermore, a plasmonic lens in the Fraunhofer region was also developed by using nanohole patches [30]. Even with the above mentioned plasmonic lens development in the Fresnel region and Fraunhofer region, the physical behaviors of plasmonic focusing in these regions have never been thoroughly studied.

Regardless of any specific lens design, to show the focusing behavior of a diffractive lens, an arbitrary plasmonic lens with a radius ρ , a designed focal length of f , and an operating wavelength λ is considered, as illustrated in Figure 2.3. Typically, the Fresnel number is used to determine the boundary of the Fraunhofer region and the Fresnel region. Assuming that the propagating media is air, which will be used in later discussions, the Fresnel number can be defined as

$$FN = \frac{\rho^2}{\lambda f} \quad (2.3)$$

When $FN \ll 1$ (i.e., $d \gg \rho$), Fraunhofer diffraction will dominate the lens behavior. On the other hand, when $FN \gg 1$, Fresnel diffraction will dominate the lens behavior.

To ensure constructive interference at the focal point F , the phase difference between the lens center O and an arbitrary point P on the lens that is a distance a away from the lens center is required to be

$$\Delta\varphi = 2N\pi + \frac{2\pi fn}{\lambda} - \frac{2\pi n\sqrt{f^2 + a^2}}{\lambda}, \quad (2.4)$$

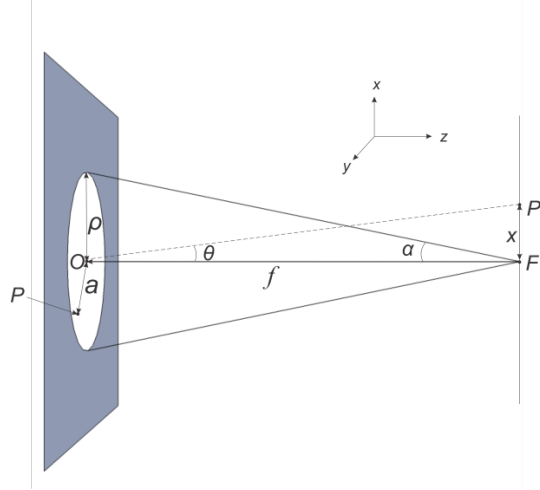


Figure 2.3 Schematic of a plasmonic lens with an arbitrary design, which has a radius ρ and a designed focal length of f . P is an arbitrary point on the lens aperture, which is away from the lens center by a distance a . F is the focus. P' is an observation point on the focal plane, which is away from F by a distance x . α is the semi-angle of the light cone from the lens aperture to the focus. θ is the observation angle of P' to the optical axis.

where N is an integer and n is the refractive index of the propagating media. For a refractive index based microlens, the phase difference is usually induced by the different thicknesses of the lens along the radial direction; while for a planar plasmonic lens, this phase difference can be achieved by modulating the complex propagating constant β of the guided SPP mode in a metal-dielectric-metal (MDM) structure. For simplicity, the guided SPP mode in a MDM slit structure is considered, which will follow the dispersion as [6]

$$\tanh\left(\frac{w}{2}\sqrt{\beta^2 - \varepsilon_d k_0^2}\right) = -\frac{\varepsilon_d \sqrt{\beta^2 - \varepsilon_m k_0^2}}{\varepsilon_m \sqrt{\beta^2 - \varepsilon_d k_0^2}}, \quad (2.5)$$

where w is the width of the slit. As can be seen from Eq. (2.5), the propagation constant β can be tuned by changing w , and thus, the width of the slit can be tailored to modify the phase difference at any point on the lens.

In previous studies [27, 31], Eq. (2.4) has been used for designing a plasmonic lens with a specific focal length without considering the diffraction regions. It has been found that there is a significant discrepancy between the focal length designed by using Eq. (2.4) and that obtained in the experiment. This is due to the fact that Eq. (2.4) is only applicable to a plasmonic lens that has a focus designed in the Fresnel region. For a plasmonic lens with a focus designed in the Fraunhofer region, Fraunhofer diffraction will dominate the lens behavior, resulting in a focal length that cannot be predicted by using Eq. (2.4) [120, 121].

In the Fraunhofer region (i.e., $FN \ll 1$), it is noted that the largest phase difference at the focus due to light propagation from two different points on the lens is

$$\Delta\varphi_{max} = \left|k_0(f - \sqrt{f^2 + \rho^2})\right| \approx \frac{k_0\rho^2}{2f} = FN \cdot \pi. \quad (2.6)$$

It can be easily obtained that $\Delta\varphi_{max} \ll \pi$, which implies that in the Fraunhofer region, $\Delta\varphi_{max}$ is negligible. According to Eq. (2.4), the phase differences due to the modulation of the SPP propagating constant should match the spatial phase difference with a $2N\pi$ difference. Therefore, the phase difference due to the disturbance from SPP phase modulation can also be neglected. In this case, the diffracting plane can be

considered to have a uniform phase. When neglecting the phase difference on the lens, the lens can be considered as a circular aperture of radius ρ and its focal length can be determined by the Fraunhofer diffraction. By applying Rayleigh-Sommerfeld integral, the normalized intensity along the optical axis can be calculated as [129]

$$I(z) = \sin^2\left(\frac{\pi\rho^2}{2\lambda z}\right) \quad (2.7)$$

Based on Eq. (2.7), the focal length f can be found as $f = z = \rho^2 / \lambda$. It can be seen that the focal length mainly depends on the radius of the lens, when $FN \ll 1$.

On the other hand, in the Fresnel region when $FN \gg 1$, based on Eq. (2.6), it can be obtained that $\Delta\varphi_{max} \gg \pi$, which means that the phase difference of different points on the lens is critical. Therefore, it is possible to modulate the phase difference with a plasmonic lens and the focal length of the plasmonic lens can be designed by using Eq. (2.4). In Table 1, several plasmonic lenses reported in the literature are listed. It can be seen that only when the $FN \gg 1$ (e.g., Refs [26], [29]) (i.e., the lens works in the Fresnel region), the designed focal length can match the experimental result. For the lenses with a focus not in the Fresnel region (e.g., Refs [27], [30], [31]), the measured focal length will not match the experimental results. However, when the focus is approaching the Fraunhofer region (e.g., Refs [27], [30]), the focal length can be well predicted by using Eq. (2.7).

Furthermore, since resolution power critically depends on the ability of a lens to focus light into the smallest spot, a focus size that is smaller than the diffraction limit has always been of great interest. However, none of designs listed in Table 1 can realize a focus beyond the diffraction limit. This is due to the fact that all the designs

are based on the principle of diffractive lens, which is inevitably limited by the diffraction limit.

To better understand the physical limit of the focus size, the lens shown in Figure 2.3 is considered. The semi-angle of the light cone from the aperture proceeding to the focus is defined as α . Let $\xi = k_0 x \sin \alpha$ be the normalized distance from the center to simplify the expressions. If the incident light is polarized in the x -direction and all points on the lens are assumed to have the same phase, the amplitude of the electric field along x -direction on the focal plane can be given as [130]

$$U = \sum_{j=1}^{\infty} a_j \frac{J_j(\xi)}{\xi}, \quad (2.8)$$

where J_j is the j th order of Bessel function of the first kind and the first four

coefficients a_j can be obtained as $a_1 = 1, a_2 = -(\frac{5}{2} \tan^2 \alpha + \frac{1}{2} \sin^2 \alpha),$

$a_3 = \frac{45}{4} \tan^4 \alpha + \frac{5}{4} \tan^2 \alpha \sin^2 \alpha - \frac{3}{8} \sin^4 \alpha,$ and

$a_4 = -(\frac{585}{8} \tan^6 \alpha + \frac{45}{8} \tan^4 \alpha \sin^2 \alpha - \frac{15}{16} \tan^2 \alpha \sin^4 \alpha + \frac{15}{16} \sin^6 \alpha).$ The field amplitude

along y -direction on the focal plane is of the same form as Eq. (8) but with different

coefficients. In this case, the first four coefficients can be obtained as $a_1 = 1,$

$a_2 = -\tan^2 \alpha, a_3 = \frac{25}{8} \tan^4 \alpha,$ and $a_4 = -\frac{204}{8} \tan^6 \alpha.$

For a lens with a radius $\rho,$ the focus will be in the Fraunhofer region if α is small (i.e., $\alpha \rightarrow 0$) so that the condition $FN = \tan \alpha \cdot \rho / \lambda \ll 1$ is satisfied. On the other hand, the focus will be in Fresnel region if α is large.

Note that when the focus of a lens is in the Fraunhofer region, the high order terms in Eq. (2.8) will be negligible and the normalized intensity distributions along x -direction and y -direction will merge to one uniform expression:

$$I = |U|^2 = \left[\frac{J_1(k_0 \rho \sin \theta)}{k_0 \rho \sin \theta} \right]^2, \quad (2.9)$$

where θ is the angle that characterizes the distance between the observation point and the focus, as shown in Figure 2.3. Note that $\xi = k_0 x \sin \alpha \approx k_0 x \rho / f \approx k_0 \rho \sin \theta$, for small angle approximation (i.e., $\sin \theta \approx x / f$ and $\sin \alpha \approx \rho / f$). Based on Eq. (2.9), the half maximum intensity occurs at $k_0 \rho \sin \theta \approx 1.6$ and the focus size D in terms of FWHM spot size is given by

$$D = 2x \approx \frac{0.51 f \lambda}{\rho}. \quad (2.10)$$

Eq. (2.10) simply describes the physical limit of the focus in terms of the spot size for a plasmonic lens designed in the Fraunhofer region, which is limited by the traditional diffraction limit. This implies that for a plasmonic lens designed in the Fraunhofer region, no matter how the lens is designed, the obtained focus can never overcome the diffraction limit of a conventional spherical lens. It should be noted that when a plasmonic lens with specific metamaterials is designed, it is possible to achieve a sub-diffraction-limit focus in the Fraunhofer region [131], which is beyond the scope of this article that only focuses on nonmagnetic materials.

According to Eq. (2.10), for a fixed f and λ , a smaller focus size can be obtained by enlarging the lens size ρ . However in this case, α will also be increased, resulting in the focus shifting into the Fresnel region. In the Fresnel region, the focus size as

well as intensity distribution at the focal plane can be obtained by using Eq. (2.8) with higher order terms. The focus size limit for the large numerical aperture cases can be studied by using Eq. (2.8) with a large α .

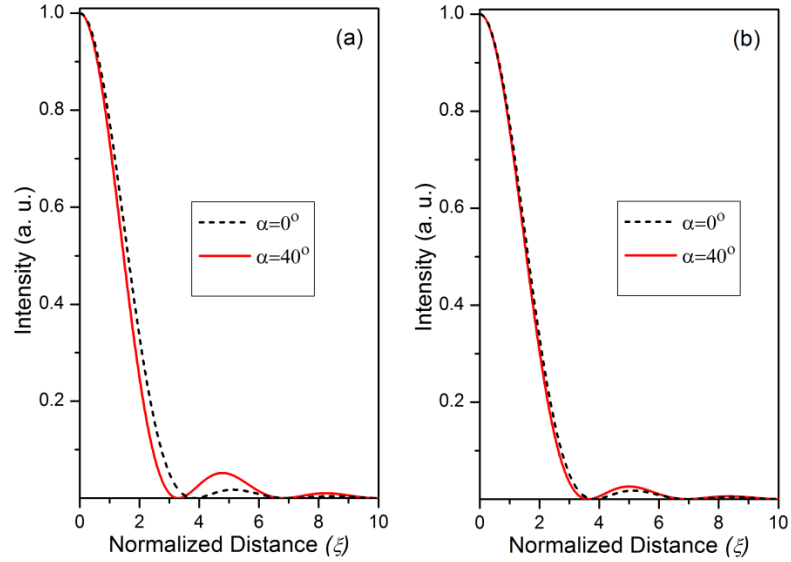


Figure 2.4 Field intensity distribution along x-direction (a) and y-direction (b), while the incident light is under x-direction polarization and with different incident angles 0° and 40° .

In Figure 2.4, the intensity distribution at the focal plane is obtained for two different α , representing the two different diffraction regions. It can be seen that the focus size obtained for $\alpha = 40^\circ$, is only slightly smaller than that obtained for $\alpha = 0^\circ$, i.e., the Fraunhofer diffraction limit. For $\alpha < 30^\circ$, the obtained focus size will be remarkably close to the Fraunhofer diffraction limit. Note that $\alpha = 40^\circ$ already represents a large angle for most plasmonic lenses designed in the Fresnel region. For an even larger α , the field amplitude based on Eq. (2.8) will become increasingly complicated due to the increased contribution from high order terms. However, by considering the first four terms only, it was found that the focus size cannot be significantly reduced by increasing α , and for certain large α , the focus size can be

even much larger than the diffraction limit. Therefore, it can be concluded that for a lens with uniform phase, a large numerical aperture cannot help significantly improve the focus size even when the lens focus is pushed into the Fresnel region.

As shown in Table 1, all the previously reported plasmonic lens designs have a larger focus size than the traditional diffraction limit predicted by Eq. (2.10), no matter they are in the Fraunhofer region or in the Fresnel region. It is interesting to note that if a plasmonic lens with a single-hole structure is designed, it will always produce a focus as small as that predicted by Eq. (2.10). This means that in terms of resolution performance, none of the designs listed in Table 1 can render a smaller focus size than a single-hole structure with the same designed radius and designed working wavelength.

Table 1. Performance parameters for the plasmonic lenses from previous references. Focal length f is predicted by Eq. (2.7) and focus size (FWHM) is predicted by Eq. (10) (length unit: nm)

Ref.	Designed Pattern	FN	Operating Wavelength	Lens Radius	Designed df	Predicted df	Measured df	FWHM	Diffraction limit
[30]	Patches of nanoholes	0.94	500	2500	NA	12500	13300	1830	1356.6
[27]	Nanoscale slit Arrays	1.18	637	2000*	20000	6279	5300	880	860.9
[31]	Nano cross-shaped aperture arrays	2.82	850	3600	15000	–	5400	1200	650.3
[26]	Nanoslits with variant widths	7.69	650	2000	600	–	800	270	132.6
[29]	Chirped circular nanoslits	50.73	532	5195	1000	–	1000	300*	52.2

* The data are approximately measured from the graph provided by the references.

Note: When $FN > 2$, Eq. (2.7) cannot be used to predict the focal length since the focus is approaching the Fresnel region.

2.3. Parameter study of plasmonic lens designed in Fresnel region

In the Fresnel region, it is meaningful to design a plasmonic lens with a specific pattern to modulate the SPP propagating constant, which makes it possible to control the interference pattern to enhance the relative intensity at the focus. Here, we will address the fundamental question: how can we design a plasmonic lens to overcome the diffraction limit? In fact, it is noted that if there is only a single ring slit at the rim of the plasmonic lens, the normalized intensity distribution on the focal plane can be obtained as [132]

$$I = |J_0(k_0 \rho \sin \theta)|^2 \quad (2.11)$$

Based on the property of zero order Bessel function of the first kind, the FWHM spot size can be found when $k_0 \rho \sin \theta \approx 1.13$. The focus size of a plasmonic lens with a ring slit can thus be determined to be

$$D \approx \frac{0.36 f \lambda}{\rho} \quad (2.12)$$

Based on this equation, the focus size of a plasmonic lens with a ring slit is about 30% smaller than the diffraction limit described in Eq. (2.10) for a circular lens of the same radius.

To verify this conclusion, FDTD simulations for a plasmonic lens with a single ring slit were conducted. As shown in Figure 2.5, the plasmonic lens used in the simulations has a thin gold film with a thickness of 400 nm deposited on a glass substrate with a refractive index of 1.458. A single ring slit with a radius of 1600 nm and a width of 120 nm is grooved on the film. The propagating media is chosen to be air with a refractive index of 1.0. A Gaussian beam with an 808 nm wavelength is

used to illuminate the lens from the substrate side. The incident light is polarized along x -direction.

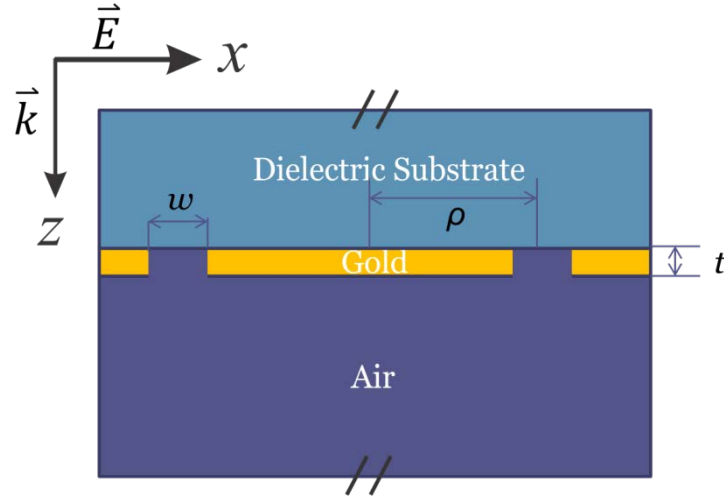


Figure 2.5 Schematic of a plasmonic lens with a single ring aperture with radius ρ and width w , which is milled in a gold film with thickness t .

The obtained intensity distribution in the x - z plane is shown in Figure 2.6(a). Because the light will be coupled into in-phase radial polarization after SPP is guided through the subwavelength MDM ring slit [44, 133], only the field distribution in the x - z plane is considered, which dominates the field distribution in all the azimuthal directions. From the intensity distribution obtained along the optical axis (Figure 2.6(b)), the focus can be found at the focal length $f=1843$ nm. Based on the intensity along the x -axis at the focal plane, as shown in Figure 2.6(c), the FWHM focus spot size can be determined as $D=320$ nm. This result is consistent with that obtained with Eq. (2.12); that is $D \approx 0.36 f \lambda / \rho$.

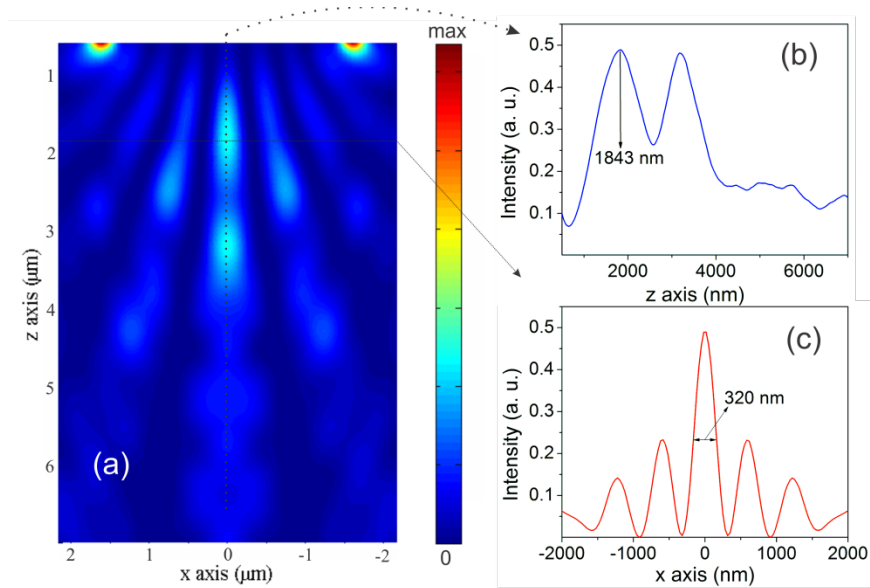


Figure 2.6 Fig 6. FDTD simulation results obtained for a plasmonic lens with a single ring slit: (a) intensity distribution of the focal plane along x - z direction, (b) intensity distribution along the optical axis, and (c) intensity distribution along the x -direction of the focal plane.

FDTD simulations of a single ring plasmonic lens with various ring radius, ring width, and lens thickness were also carried out (data not shown). The results indicate that the field distributions of all the plasmonic lenses with a single ring aperture can be characterized by using the zero order of Bessel function of the first kind, as long as the following two conditions are satisfied: i) the ratio w/ρ is small enough so that the structure can be considered as a single ring and ii) the thickness of the lens is big enough to prevent direct light penetration. All focus sizes obtained from these simulations match well with those predicted by using Eq. (2.12). Therefore, a plasmonic lens with a single ring structure can indeed help achieve a sub-diffraction-limit sized focus. However, as can be seen from Figure 2.6(c), the intensity pattern at the focal plane has many strong side lobes, which is the disadvantage of the plasmonic lens with a single ring structure, resulting in relatively low intensity at the

focus. For practical applications, the side lobes need be suppressed and the relative intensity of the focus should be enhanced.

To address the issue of strong side lobes, a plasmonic lens with multiple concentric rings can be used. Consider a representative example that has three concentric ring structures added to the single ring structure, as shown in Figure 2.7. The effect of multiple rings can be considered to be similar to that of multiple slits in one dimension. Owing to the contribution of the multiple slits interference, the number of the side lobes can be decreased and the relative intensity at the focus can be enhanced. FDTD simulations were carried out for a plasmonic lens with 4 concentric rings with radii of 300 nm, 828 nm, 1074 nm, and 1600 nm, which is grooved on a 400 nm thick gold film deposited on a glass substrate with a refractive index of 1.458.

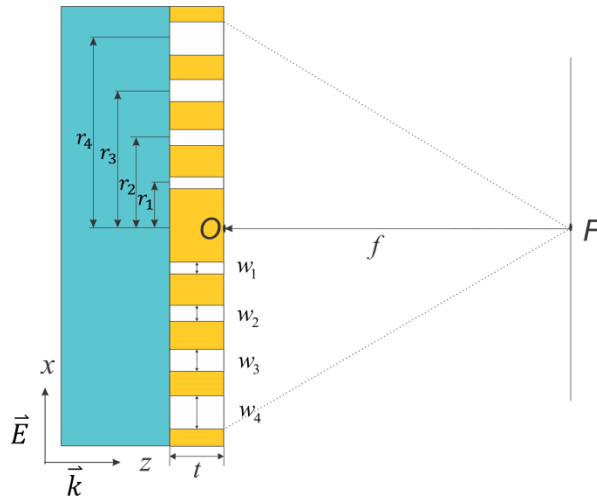


Figure 2.7 Schematic of a plasmonic lens of 4 concentric ring slits with radii of r_1 , r_2 , r_3 , r_4 and widths of w_1 , w_2 , w_3 , w_4 milled on a gold film with a thickness of t . The designed focal length is f . F is the focal point and O is the center of the lens.

The widths of the rings are 60 nm, 72 nm, 85 nm and 120 nm, respectively. The width of each ring is chosen to be different so that the corresponding phase modulation obtained at each slit will ensure constructive interference at the focus and Eq. (2.4) can be satisfied. The propagating media is considered to be air. Note that the focal length should be carefully chosen so that the lens will work in the Fresnel region to take advantage of the phase modulation induced by SPP propagation constants, as discussed previously. It is worth noting that the outermost ring is designed to have the largest width to ensure that the light propagating through this ring will dominate the field distribution, and thus, the field distribution at the focus can be approximated by using the zero order Bessel function of the first kind. This makes the current design conceptually different from the previously reported plasmonic lens designs with concentric rings structures [29], in which the outermost ring was designed to have the smallest width. Compared with the design described in Ref. [29], this new type of design will render much smaller focus size which is even smaller than the diffraction limit. The experimental demonstration of sub-diffraction-limit focusing phenomenon has been reported in our previous work [83]. Here, in this article, we provide further understanding of the physical behaviors of this type of lenses.

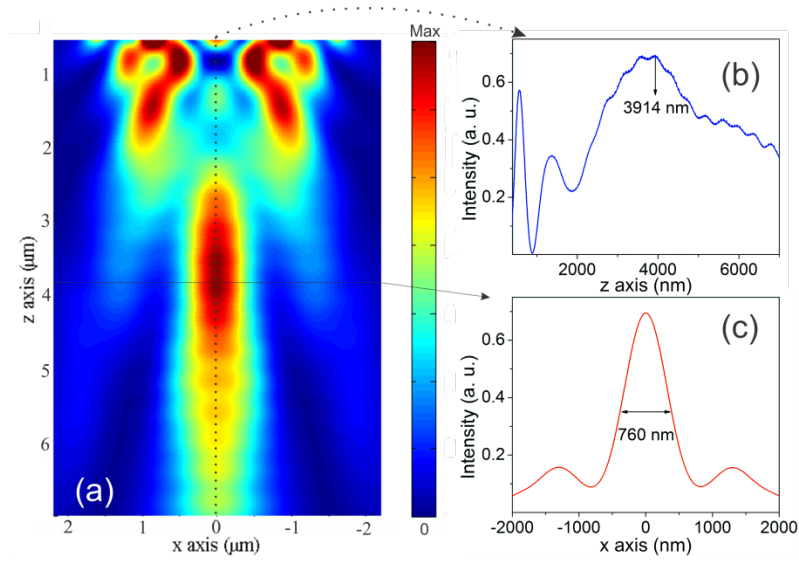


Figure 2.8 FDTD simulation results of a plasmonic lens with 4 rings: (a) field intensity distribution in the x - z plane, (b) intensity distribution along the optical axis, and (c) intensity distribution along the x -direction of the focal plane.

As can be seen in Figure 2.8, the field intensity distribution (Figure 2.8(a)) of the plasmonic lens with 4 rings exhibits a much stronger focus than that of the plasmonic lens with a single ring (Figure 2.8(a)). The intensity distributions along the optical axis and the x -direction of the focal plane are also obtained, as shown in Figure 2.8(b) and Figure 2.8(c), respectively. Based on these results, it can be seen that the side lobes have been greatly suppressed. The focal length f and focus size D are found to be 3914nm and 760 nm, respectively. This renders a focusing resolution of $D \approx 0.38f\lambda / \rho$, which is slightly larger than the resolution defined by Eq. (2.12), but still smaller than the conventional diffraction limit.

To further enhance the relative intensity at the focus and suppress the side lobes, it was found that enlarging the width of the outermost ring is the most efficient way. Therefore, FDTD simulations were conducted for a plasmonic lens with the same parameters as that used to obtain Figure 2.8 except that the width of the outmost

ring is enlarged to 180 nm. The phase delay rendered by the 180 nm slit is only 5% different from the one presented by 120 nm slit. Thus the constructive interference at the focus will be reasonably satisfied with the width change. The results are shown in Figure 2.9.

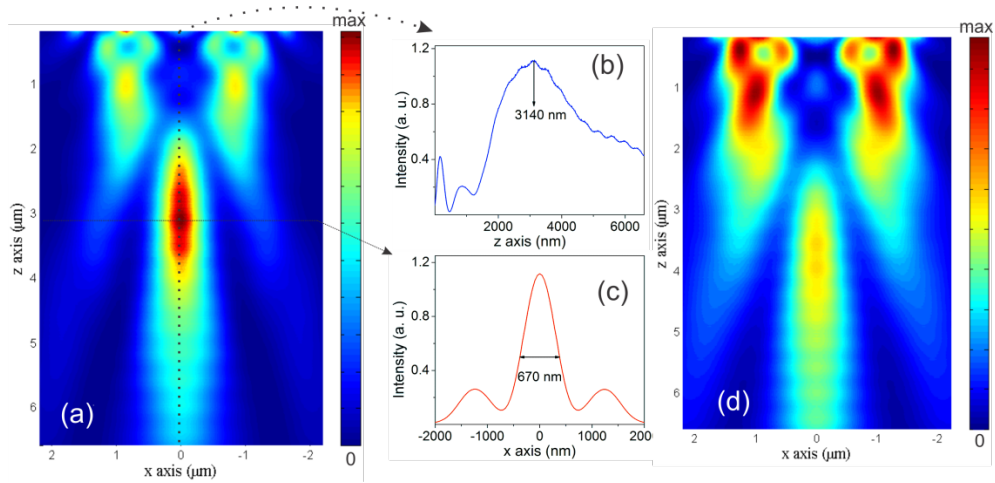


Figure 2.9 FDTD simulation results of a 4 ring plasmonic lens with an enlarged width: (a) field intensity distribution in the x-z plane, (b) intensity distribution along the optical axis, and (c) intensity distribution along the x-direction of the focal plane. (d) Field distribution in the x-z plane of a 4 ring plasmonic lens with perfect conductor.

As can be seen from Figure 2.9(a), the relative intensity at the focus is largely enhanced and the side lobes are heavily suppressed, compared with Figure 2.8(a). It can be obtained from Figure 2.9 (b) and (c) that the focal length is 3140 nm and the focus size is 670 nm. In this case, the resolution is found to be further decreased to $D \approx 0.42f\lambda/\rho$.

To address the importance of the phase modulation induced by SPP propagating through the lens, we also conduct a simulation for a lens that has the same parameters as the lens used to obtain Figure 2.9 (a) but using perfect conductor (PEC) as the material for comparison, as shown in Figure 2.9(d). In this case, there will be no

plasmonic wave propagating along the MDM structure and thus there is no plasmonic phase modulation in Eq. (2.4). This will result in non-perfectly constructive interference at the focus, but strong constructive interference at the side lobes. As can be seen from Figure 2.9(d), the perfect conductor lens has a low relative intensity at the focus, worse resolution, and strong side lobes. This result validates the role of the plasmonic waves for enhancing the constructive interference at the focus and to suppress the side lobes. Nevertheless, a perfect conductor lens can also present high relative intensity focusing by applying the design of Fresnel zone plates where the phase modulation is purely from the spatial phase difference. However compared with the plasmonic lens design shown in Figure 2.8, a Fresnel zone plate lens suffers from large size and its focus is limited by the diffraction limit. For instance, the radius of a Fresnel zone plate lens should be designed to be larger than 5000 nm to achieve the similar focusing effect as that shown in Figure 2.9(a).

In fact, the relative intensity at the focus can be further enhanced by enlarging the width of the outermost ring even further. However, this will result in a further degradation of the resolution. Therefore, there is a trade-off between the resolution and the relative focus intensity in the design of a plasmonic lens with multiple ring structures. This trade-off can be understood by examining the properties of the Bessel function $J_0(\xi)$ in Eq. (2.12) and the first order Bessel function of first kind $J_1(\xi)$ in Eq. (2.9). When the width of the ring is small enough, Eq. (2.12) can be applied to calculate the intensity distribution of the cross-section, which is defined by the profile of $J_0(\xi)$. However, as the ring width increases, the field distribution of the plasmonic lens will approach to that of a single hole, which is getting more and more close to the

profile of $J_1(\xi)$ as defined in Eq. (2.9) since the aperture gradually changes from a ring to a hole. Clearly, the intensity distribution defined by $J_0(\xi)$ will have better focus resolution, while an intensity distribution defined by $J_1(\xi)$ will give much smaller side lobes and stronger relative focus intensity, as illustrated in Figure 2.10.

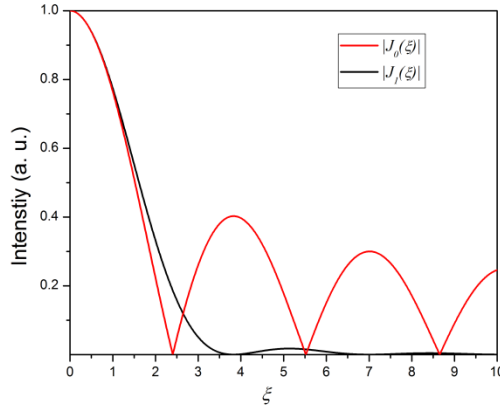


Figure 2.10 Comparison of angular intensity distribution of a single ring lens $J_0(\xi)$ (red line) and a single hole lens $J_1(\xi)$ (black line)

In summary, the FDTD simulations show that a sub-diffraction-limit focus size can be achieved by using a plasmonic lens with a single ring or multiple concentric rings. A single ring plasmonic lens renders better resolution, while a lens with multiple rings enables better relative focus intensity. The intensity at the focus can be enhanced by utilizing multiple-slit interference as well as enlarging the width of the outermost ring. However, there is a trade-off between the resolution and the relative focal intensity; the resolution will be reduced while the relative intensity at the focus is enhanced. Furthermore, to design a plasmonic lens with a sub-diffraction-limit focusing resolution, the following guidelines need to be considered. First, the focus of the multiple-ring plasmonic lens must be designed to be close to the Fresnel region to render any meaningful phase delay that can play an important role in multiple-slit

interference. Second, the grooved area of the outermost ring should be designed to be much larger than the sum of the rest rings so that it can play a dominating role to the intensity distribution and can be treated as the rim of the lens. In this case, the intensity distribution profile will be close to $J_0(\xi)$ to render the sub-diffraction-limit resolution. Third, the width of the outermost ring should not be too large. Otherwise, it will lead to the intensity distribution close to that of a single hole that is governed by $J_1(\xi)$ and the sub-diffraction-limit resolution cannot be achieved.

It's worth to mention that our plasmonic lens design in Fresnel region has some similarity with Fresnel zoom plates [134], since they both utilize the phase modulation in Fresnel region to focus light. However, Fresnel zoom plates, which are mostly used to focus high energy electromagnetic radiation (Gamma ray and X-ray), are designed with smaller ring width for the outer ring. That is opposite to our design. More importantly, Fresnel zoom plates are still restrained by diffraction limit [134, 135].

Besides plasmonic lenses, there are multiple other methods to improve the optical focusing resolution have been achieved. Holographic techniques can break the diffraction limit, though the resolution was restricted in the specific experimental analysis [136]. Confocal laser scanning microscope is capable of enhancing the resolution to $D \approx 0.37\lambda / NA$ because of the narrower intensity point spread function[137]. However, the confocal microscope system is difficulty to be miniaturized. Near-field scanning optical microscopy (NSOM), on the other hand, which uses evanescent waves, has been demonstrated a lateral resolution of 20 nm [138, 139]. Nevertheless, it suffers from the limited working distance similar to the

case of the plasmonic lens in the surface plasmon dominating region. After all, we find plasmonic lens might be the best candidate for improving the miniaturized imaging system.

In this chapter, we define three different regions in designing a plasmonic lens, namely, the surface plasmon dominated region, the Fraunhofer region, and the Fresnel region. We have shown that it is important to understand the physical behaviors of a plasmonic lens designed in the three different regions, because each of them is governed by different physics principles and presents different physical limits in focal length and focal size. In the SPP dominating region, both the region boundary and focus size depend on the material properties of the metal and dielectric. The SPP attenuation length on the dielectric side defines the boundary of the SPP dominating region. The focus size can be much smaller than the conventional diffraction limit due to the short SPP wavelength. Away from SPP dominating region, diffraction behavior will dominate the lens performance and two diffraction regions, namely, the Fraunhofer region and the Fresnel region are defined by Fresnel number FN . For a plasmonic lens designed in the Fraunhofer region ($FN \ll 1$), the focal length can only be determined by using the Fraunhofer diffraction theory and the focus size is always limited by the traditional diffraction limit for a normal propagating media. In the Fresnel region ($FN \gg 1$), owing to the diffraction property of a single-ring-slit aperture and the phase modulation induced by the SPP propagating constant, it is possible to achieve a plasmonic lens with a sub-diffraction limit focus size in this region and it is feasible to design a lens with a desired focal length. This has been demonstrated in this article by using a plasmonic lens with a single ring structure or

multiple concentric ring structures through numerical simulations. The multiple concentric ring structure is found to be helpful to enhance the relative intensity at the focus, which can be enhanced further by enlarging the width of the outermost ring, yet resulting in degradation of the resolution. The parameter study provides some guidelines to design sub-diffraction limit plasmonic lens in Fresnel region.

The physical understanding and results presented in this article for plasmonic focusing in different regions provide a basis for future plasmonic lens designs with the objective of enhancing the focus resolution. These findings can also provide guidelines to inspire new designs of high performance plasmonic lenses, which will have great potential in many applications including microscopy, sensing, and nanofabrication.

Chapter 3. Radially polarized light generated by TEM mode resonance and its applications

3.1. *Introduction*

Radially polarized light has many applications, such as photolithography, imaging and optical manipulation, because of its property to focus light to a smaller spot than linearly polarized light. However, it is not easy to generate a radially polarized light (Coherent superposition of two orthogonally polarized modes, conical Brewster prism, integrate spatially variant wave plate, combination of SLMs, concentric metallic gratings fabricated on optical fibers). On the other hand, for many applications, it requires aligning the optical axis with the axis of the radially polarized light, which brings another difficulty. Here, we want to discuss the new method to generate TEM mode, which is naturally radially polarized light, with the help of metallic annular aperture array and radially polarized focusing with ring structure on a metal film with dielectric layer covered.

Recently, it has been found that the TEM mode can be excited in the annular aperture array on the metal slab with inclined TM incidence[140]. We will investigate this phenomenon in details and will introduce the structure which can excite TEM mode resonate with normal incidence. TEM mode is naturally radially polarized. Thus it may find useful in some applications requires radially polarized light source. Additionally, the extraordinary transmission through the metal slab due to the TEM

mode resonance may play importance role in some applications, since there is no cut-off wavelength for TEM mode.

3.2. TEM resonance generated with inclined incidence

3.2.1. Theoretical model

The TEM mode resonance will be generated in a finite coaxial waveguide structure without cut-off frequency under TM inclined incidence. For the normal incidence, no TEM mode resonance can be excited due to the component mismatch. For the propagating TEM mode in the annular aperture, there will be a peak in the transmission spectrum while the Fabry-Perot resonance condition is satisfied.

$$\lambda_{TEM} = \frac{2\pi n'_{eff} l}{N\pi - \phi_r}, \quad (3.1)$$

where λ_{TEM} is the resonance wavelength, n'_{eff} is the real part of the effective index of the TEM mode, ϕ_r is the phase delay due to the reflection at the interface (it can be obtained theoretically), and N is the order of the resonance and l is the thickness of the metal film. $n'_{eff} = 1$ for the perfect conductor (PEC) and air situation and will be larger than one for the real metal or the situation that dielectric fills in the aperture. While the resonance condition stands, radially polarized beams will be found on the emitting side.

If the TEM mode can be excited in the annular apertures, it's naturally radial polarized as the electric field and magnetic field can be expressed as

$$E_\rho = \frac{e^{ik_d z}}{\rho} \quad (3.2)$$

$$\text{and } H_\phi = \sqrt{\frac{\varepsilon_d \varepsilon_0}{\mu_0}} \frac{e^{ik_d z}}{\rho}, \quad (3.3)$$

where $k_d = \omega \sqrt{\varepsilon_d \varepsilon_0 \mu_0}$, ω is the angular frequency, ε_0 and μ_0 are the permittivity and permeability in air and ε_d is the permittivity of the dielectric in the annular aperture. Moreover, this radially polarized light is naturally aligned with the optical axis of plasmonic lens. The annular aperture is shown as in Figure 3.1[141]. The thickness of the structure is l and the inner and outer radii of the annular aperture are a and b . It is assumed that the material of the lens is perfect conductor.

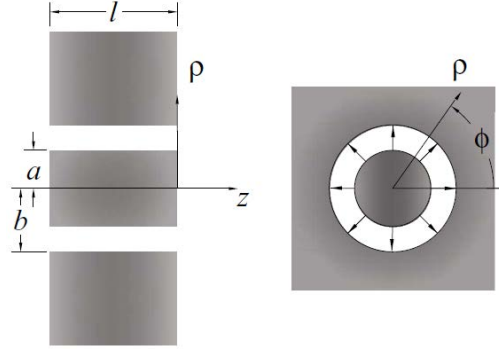


Figure 3.1 Schematic of annular aperture in a metal plate. The electric field polarization of the TEM mode is also shown[141].

For any incident light, it is composed of TE and TM components. Assume the amplitudes of TE and TM electric fields are E_{TE} and E_{TM} . By solving the TEM modes in the annular aperture, the electric field and magnetic field of a TEM mode with E_{TE} and E_{TM} can be expressed as [140]

$$E_\rho = C \cos \theta E_{TM} J_1(kr \sin \theta) \text{ and}$$

$$H_\phi = \frac{-Ck}{\mu_0 \omega} E_{TM} \left\{ \left(\frac{3}{4} \cos 2\theta + \frac{1}{4} \right) J_1(k\rho \sin \theta) + \frac{\sin^2 \theta}{2} J_3(k\rho \sin \theta) \right\}, \quad (3.4)$$

where $C = ie^{ikz\cos\theta}$. J_n is the Bessel function of the first kind of order n . As can be seen, the fields of TEM modes will be non-zero only if E_{TM} and θ are non-zero, in another word, the TEM modes in the annular aperture can only be excited when the incident light has an off-normal TM component.

After the TEM mode is excited by inclined TM incidence, it propagates along the annular aperture as (3.2) and (3.3). Assume the reflective coefficient of the TEM mode at the end of the annular aperture is r , the TEM mode fields at the interface are

$$E_\rho(\rho, z = 0^-) = (1+r) \frac{1}{\rho} \quad (3.5)$$

$$\text{and } H_\phi(\rho, z = 0^-) = (1-r) \sqrt{\frac{\varepsilon_d \varepsilon_0}{\mu_0}} \frac{1}{\rho}. \quad (3.6)$$

For the light remitting to the free space (with permittivity ε_0) at $z = 0^+$, it can only have the rotationally symmetric modes as the same as TEM modes, thus

$$E_\rho(\rho, z = 0^+) = \int_0^\infty t(k) \frac{\sqrt{k_0^2 - k^2}}{\omega \varepsilon_0} J_1(k\rho) dk \quad (3.7)$$

$$\text{and } H_\phi(\rho, z = 0^+) = \int_0^\infty t(k) J_1(k\rho) dk. \quad (3.8)$$

By applying the continuous boundary condition at $z=0$ and with considering orthogonality of Bessel functions, the reflective coefficient can be found as [141]

$$r = \frac{1-G}{1+G}, \quad (3.9)$$

where

$$G = \sqrt{\frac{\mu_0}{\varepsilon_d \varepsilon_0}} \frac{\omega \varepsilon_0}{\ln \frac{b}{a}} \int_0^\infty \frac{[J_0(ka) - J_0(kb)]^2}{k \sqrt{k_0^2 - k^2}} dk. \quad (3.10)$$

The phase delay can be presented as

$$\varphi_r = \tan^{-1}(\text{Im}(r) / \text{Re}(r)) , \quad (3.11)$$

which is the important term in Eq. (3.1).

3.2.2. Simulations with PEC

As mentioned previously, the inclined incident light can be used to generate TEM mode in the annular aperture on metal at the resonant wavelength. For proof-of-concept demonstration, FDTD simulations (CST MWS) were carried out to calculate the transmission spectrum for such structure and the field distribution at the resonance. Here, the following structure is considered: an annular aperture array with the periodicity of 300 nm fabricated on a perfect conductor slab with a thickness of 600nm. The inner radius and the outer radius of each annular aperture are 75 nm and 100 nm respectively. With the 45° inclined incidence with TM polarization, the spectrum is calculated and shown in Figure 3.2. It is seen that, in the frequency range of 200 THz to 700 THz, there are three TEM mode resonances at 232 THz, 465 THz and 661 THz, which satisfy Eq. (3.1). To verify that these peaks are the TEM mode resonances, the field distributions at the surface of the emitting side are calculated at the emitting surface of the structure. After normalized by the maximum intensity, the field distributions show the same profile as shown in the inset, which are the profile of TEM mode field distribution with radial symmetry. The field distributions of the non-TEM mode peaks are also calculated for comparison. As can be seen, there is no radial symmetry for those modes, which indicates they are TE or TM modes.

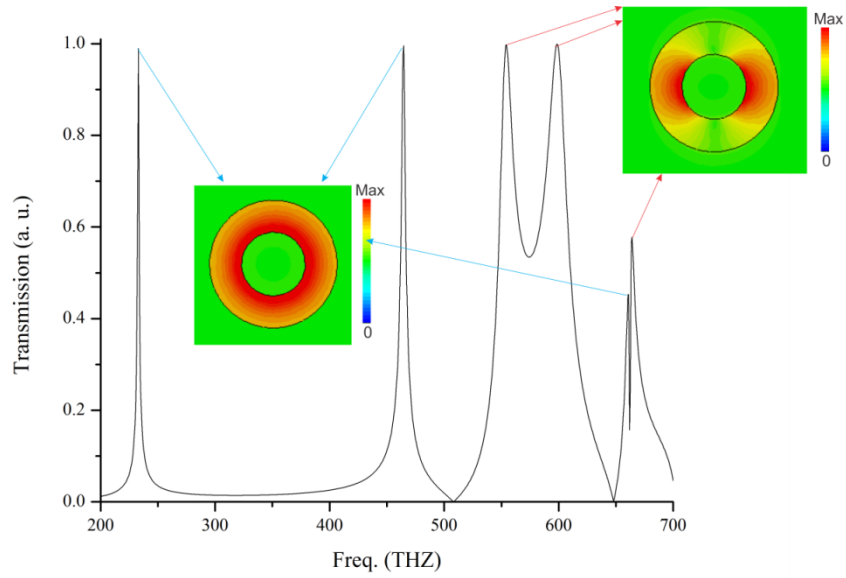


Figure 3.2 Transmission spectrum for the annular aperture array with PEC. The field distribution is calculated at the end of the emitting side.

Further, the TEM resonances are found to be independent of periodicity and incident angle. As shown in Figure 3.3, the periodicity is changed from 300 nm to 600 nm, but the position of the first order TEM mode at 232 THz does not change. It shows similar results with incident angle changing. Thus, the resonant frequency of TEM modes does not change either with the periodicity or the incident angle.

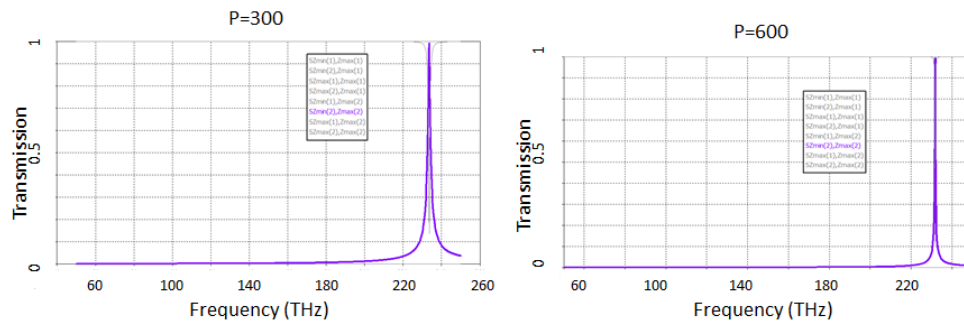


Figure 3.3 Transmission spectrum for 1st order TEM mode for $P=300\text{nm}$ and $P=600\text{nm}$.

3.2.3. Simulations with silver

For the real metal situation, silver has been considered. From the Eq. (3.1), it is expected that the effective refractive index will increase for the silver situation, which results in an increase in the resonance wavelength. To ensure the TEM mode resonance occurs in the visible range for the silver case, the parameters of the structure are modified accordingly. An annular aperture array with the periodicity of 450 nm is fabricated on a silver slab with the thickness of 495 nm. The inner radius and the outer radius of each annular aperture are 65 nm and 130 nm respectively. The spectrum of the structure under 45° inclined incidence with TM polarization is calculated and shown in Figure 3.4. The first order of TEM mode is found at 193 THz. On the other hand, the TE modes and TM modes supported in this structure are also shifted to a lower frequency region and the line-widths are broadened. Thus, the higher order TEM modes, $N=2$ and $N=3$, are overlapped with the TE and TM modes. Therefore, only one pure TEM mode has been found in the silver situation at the frequency range of the simulation. The field distribution at the end of emitting side for the peak at 193 THz has been calculated. As can be seen from the field distribution, it is TEM mode.

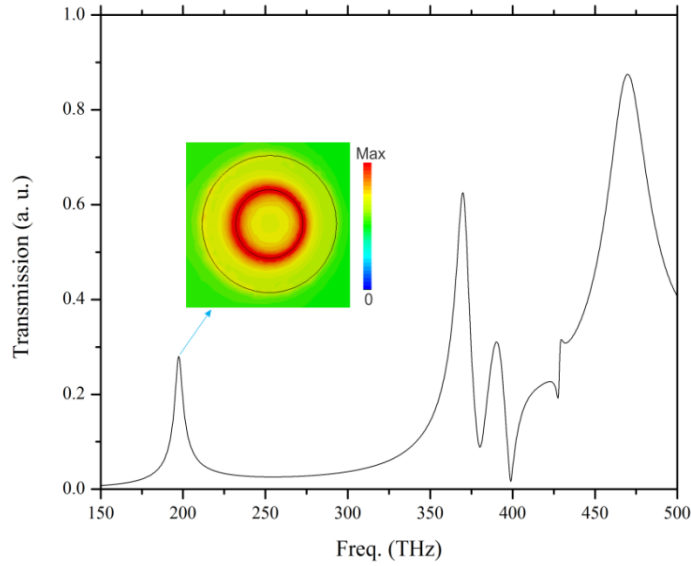


Figure 3.4 Transmission spectrum for the annular aperture array with silver. The field distribution is calculated at the end of the emitting face.

The field distributions were also calculated in the cross-section planes from the side view, for the first order TEM mode at 193 THz in Figure 3.5 (a), and 440 THz where the 3rd TEM mode should occur according to Eq. (3.1) in Figure 3.5 (b). As we can see, for the 1st order TEM mode, the mode penetrates through the silver slab and the radial symmetry is kept. For 440 THz case, the radial symmetry is lost gradually along the propagation direction and the TE mode field distribution becomes dominating. This means the TEM mode is overlapped with TE mode at 440 THz.

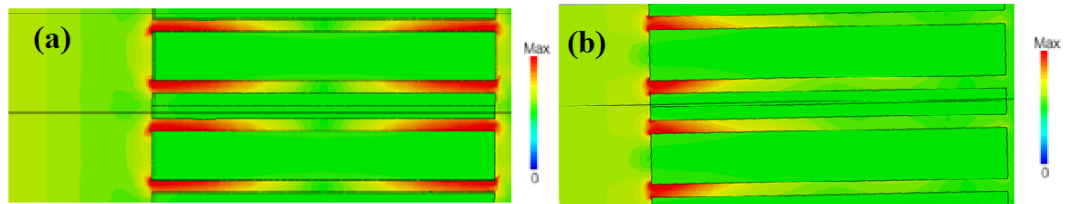


Figure 3.5 The field distributions at the cross-sections from side view for (a) 193 THz and (b) 440 THz.

3.3. TEM resonance generated with normal incidence on PEC

For the structures discussed in the previous sections, an inclined incidence is required for the TEM mode generation. However, this is not preferable for many applications. Although the resonance frequency of TEM mode is affected by the incident angle, the angle will vary with respect to the transmittance of TEM mode. Moreover, the normal incidence is much easier to align than the inclined incident. Therefore, a configuration that can excite the TEM mode resonance with normal incidence is preferable. Here, a SiO₂ grating layer on the top of the annular aperture with the same periodicity of the annular aperture is introduced. The field component of TEM mode can be matched with the diffraction from the grating. Thus the TEM mode can be generated even with the normal incidence.

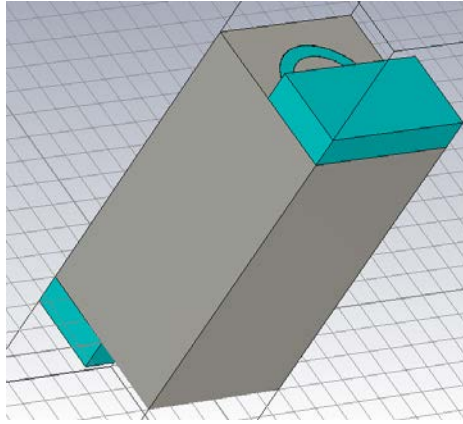


Figure 3.6 Schematic of the annular aperture array with dual gratings on the top and bottom.

For the simulation simplicity, the PEC is chosen as the metal film in this case. As shown in Figure 3.6, a SiO₂ grating is attached to the PEC annular aperture array. The annular aperture is filling with SiO₂ for the fabrication consideration. Another SiO₂ grating layer is attached to the bottom of the metal film to match the ϕ_r in the Eq. (3.1) from the top and bottom interface. The thickness of PEC is 600 nm, the

periodicity is 300 nm, the inner and outer radii of the annular aperture are 75 nm and 100 nm respectively. A normal incident light with TM polarization is considered. The spectrum is calculated as shown in Figure 3.7(a). It is seen that, there is a transmission peak at 317THz. To find out whether it is TEM mode resonance, the field distribution at the end of the emitting surface and the cross-section have been calculated. As can be seen, the peak at 317THz is a TEM mode with central symmetric field amplitude distribution. Therefore, it is demonstrated that the novel design of the annular aperture array with dual gratings on the top and bottom can be used to excite TEM resonance under normal incidence. It is expected that it can benefit some imaging systems which require radially polarized light generated under normal incidence to improve the resolution.

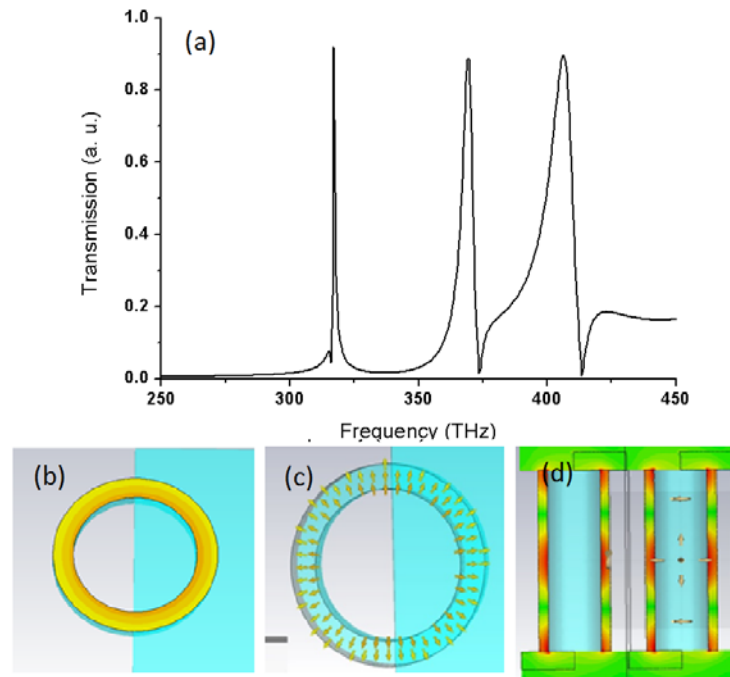


Figure 3.7 (a) The transmission spectrum for the structure in Figure 3.6 under normal incidence. (b) The field distribution calculated at the end of the emitting face at 317 THz. (c) The direction of electric field distribution at the end of the emitting face at 317 THz. (d) The field distributions at the cross-sections from side view at 317 THz.

3.4. Surface plasmon dominating region plasmonic lens with radially polarized light generated by TEM resonance

It has been theoretically shown that the radially polarized light can be generated on a plasmonic annular structure with a linearly polarized incidence if the incident angle is off-normal. In this section, the behavior of plasmonic lenses under inclined incident light is studied.

Plasmonic lenses under inclined incidence for very small incident angle have been studied [15]. As shown in Figure 3.8, a ring slit aperture with radius R is milled on a silver film, serving as a plasmonic lens. The excitation light is incident at an angle θ . The surface plasmon excited at the edge of the slit at point A will propagate on the surface and superposition with the contribution from other points on the circumference of the slit at point B with a distance x away from the center. The position of B can be determined by the relation

$$x^2 \left(\frac{k_{spp}^2}{k_{in}^2} - 1 \right) = R^2 - 2Rx \cos \alpha , \quad (3.11)$$

where k_{in} is the in-plane component of the incident wave vector k_0 defined by $k_{in} = k_0 \sin \theta$, k_{spp} is the excited SPP wave vector. For a very small incident angle, x is much smaller than R , then the term $-2Rx \cos \alpha$ is much smaller than R^2 , which means it is negligible. Therefore the equation can be expressed as

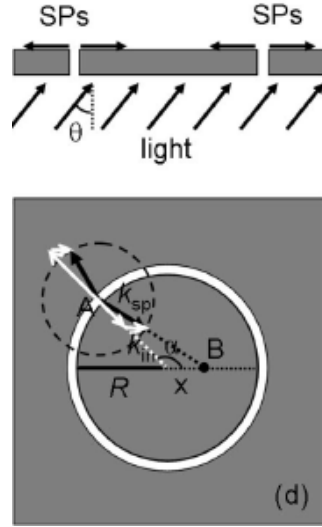


Figure 3.8. Sketch of a plasmonic lens under inclined illumination and its top view. The focus point B of the plasmonic lens shifts away from the center under inclined illumination [15]

$$x = \frac{Rk_{in}}{\sqrt{k_{spp}^2 - k_{in}^2}} \quad (3.12)$$

In this condition, x is independent of α , which means all the SPP will be guided to point B and there will be only one focus point on the surface. It is verified by the numerical simulations and experiments that there is only one focus on the surface while the incident angle is within 26.6° [15].

When the incident angle keeps increasing, k_{in} will become larger. Thus, x gets bigger according to Eq. (3.12). Therefore, the term $-2Rxcos\alpha$ in Eq. (3.11) can no longer be negligible. This means x will depend on α , which indicate that there will be multiple constructive interference points (focus points) near the surface. To verify this, consider a plasmonic lens under large incident angle as shown in Figure 3.9. A plasmonic lens with large radius $r=3000$ nm is milled on a free standing silver film with thickness $t=570$ nm. The width of the slit is $w=65$ nm. The plasmonic lens is under the illumination with an inclined angle $\theta=45^\circ$. The incident light is linearly

polarized with polarization direction parallel to x -axis (i.e., TM polarization incidence). The incident wavelength is $\lambda=1435$ nm.

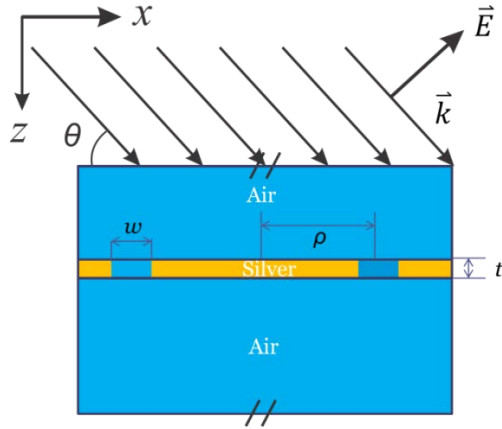


Figure 3.9 Schematic of a plasmonic lens with a single ring aperture with radius ρ and width w , which is milled in a gold film with thickness t

The FDTD simulation result of the field distribution of the plane 10 nm away from the plasmonic lens is shown in Figure 3.10. The permittivity of silver from the optical handbook [127] is used in the simulation. It can be clearly seen from the result that there are multiple focus points with the same order of intensity shown near the lens surface.

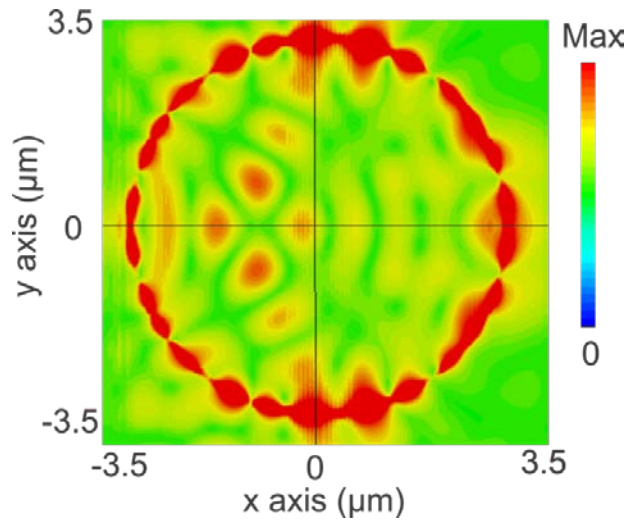


Figure 3.10 The field intensity distribution at the plane 10 nm distance away from the designed plasmonic lens surface for $\theta=45^\circ$ and $\lambda=1435$ nm.

It is known that the plasmonic lenses under inclined incidence could present multiple focuses in the near-field, which is not preferable to the nanolithography application. Therefore, the question is how the plasmonic lens can generate a single focus and render a large focal depth at the same time.

As discussed previously, the annular aperture under linearly polarized inclined incidence can couple TEM waveguide mode inside the aperture out to the free space if the aperture thickness is big enough and Fabry-Perot resonant condition in Eq. (3.1) is satisfied by all the parameters. Because TEM mode is naturally radially polarized, it will excite SPPs with the same phase and amplitude at every point on the circumference of the aperture. Thus a strong constructive SPP interference will be formed in the center of the lens. Moreover, the field intensity will follow the trend of zero-order Bessel function due to the radially symmetric solution enforcement which means it will render non-diffractive Bessel beam with very long focal length.

To demonstrate this kind of non-diffractive Bessel beam, a plasmonic lens working at the Fabry-Perot resonant condition is designed. The configurations are the same as the plasmonic lens described in Figure 3.9, with $r=3000$ nm, $t=570$ nm and $w=65$ nm. However, the operating wavelength is shifted to 758 nm. The incident light is also TM polarized with incident angle $\theta=45^\circ$. The numerical simulation result for the field distribution at the plane that is 10 nm away from the plasmonic lens is shown in Figure 3.11.

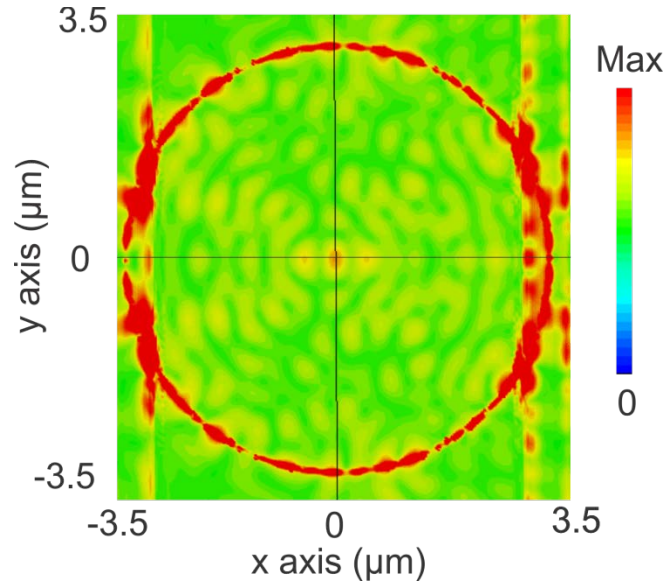


Figure 3.11 The field intensity distribution at the plane 10 nm distance away from the designed plasmonic lens surface for $\theta=45^\circ$ and $\lambda=758$ nm

From the result, it can be seen there is only one strong focus occurred at the center of the lens while the plasmonic lens is working at Fabry-Perot resonant wavelength under inclined incidence. The field intensity distribution at the x-z cross section is also plotted in Figure 3.12(a). As can be seen, the emitting beam does have the property close to non-diffractive Bessel beam, which has a very large focal depth and the intensity profile following the trend of zero order Bessel function. The intensity along the optical axis is plotted in Figure 3.12(b), and it shows that the focal depth (FWHM) is 1280nm which is much larger than any other plasmonic design for nanolithography application.

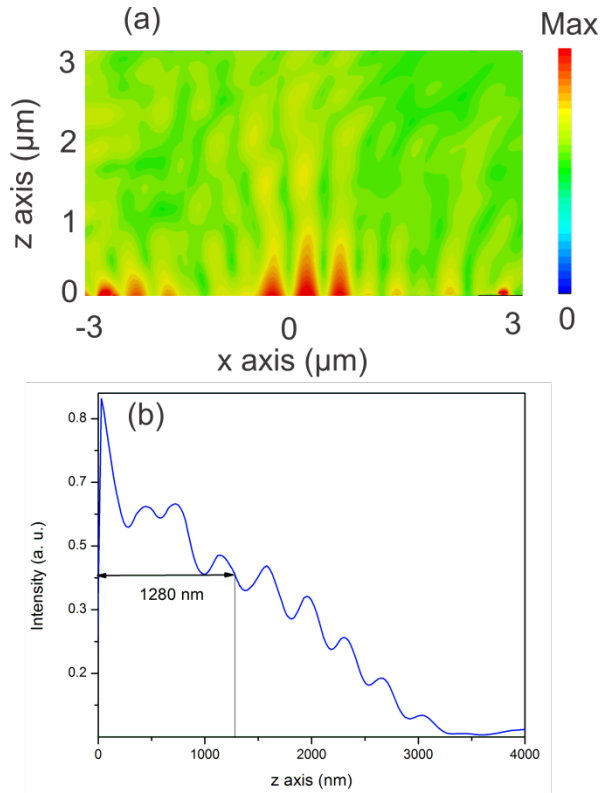


Figure 3.12(a) The field intensity distribution at the x-z cross section for the designed plasmonic lens surface for $\theta=45^\circ$ and $\lambda=758$ nm. (b) The intensity along the optical axis.

The field intensity distribution on the y-z cross section is also shown in Figure 3.13(a). The same non-diffractive Bessel beam property can be found. The intensity along the y axis for $x=0$ and $z=0$ is presented in Figure 3.13(b) to find the focus size (FWHM) is about 370 nm which is a small subwavelength focus.

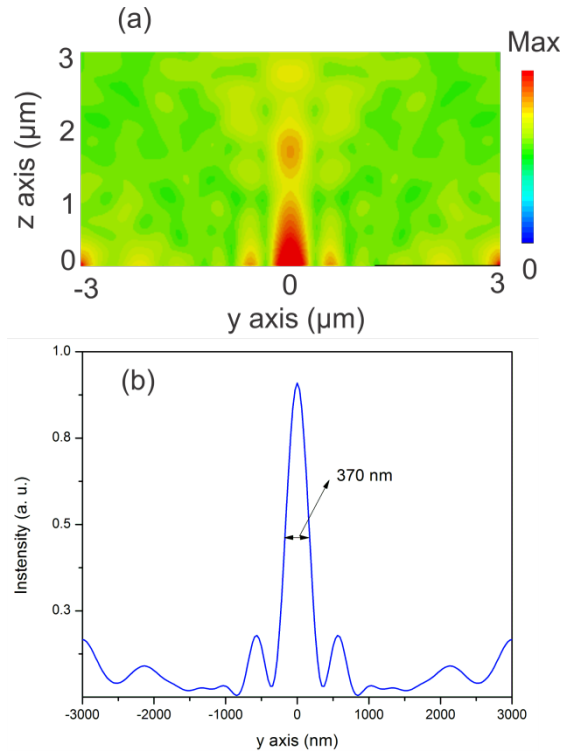


Figure 3.13 The field intensity distribution at the y - z cross section for the designed plasmonic lens surface for $\theta=45^\circ$ and $\lambda=758$ nm. (b) The intensity along the y axis for $x=0$ and $z=0$

Here, it is demonstrated that the plasmonic lens working at Fabry-Perot resonant wavelength under inclined incidence can emit non-diffractive Bessel beam that has a large focal depth and a small focus size. Although it is not a pure non-diffractive Bessel beam due to the existence of the other modes other than the TEM mode in the annular aperture, these results may benefit miniature imaging systems, such as maskless nanolithography systems.

It is worth to mention that we theoretically and numerically studied a suspending silver plasmonic lens here as a proof of concept that TEM resonance can be utilized to enhance the performance of the plasmonic lens and solve the system aligning difficulty. Nevertheless, in the real applications, a dielectric substrate must be considered in the system, including the scattering from the dielectric interface, and

effective material property change. Also, silver, although it owns a very good plasmonic property, is not preferred for the real applications due to its chemical instability[142]. Other materials, such as gold, platinum, and aluminum might be found better candidates for the real devices, by considering the plasmonic property and chemical stability [143].

Chapter 4. On-fiber plasmonic structures for multi-parameter sensing

4.1. *Overview of on-fiber multi-parameter sensing*

For decades, sensor miniaturization has received a lot of attention in a broad range of applications for physical, chemical and biomedical parameters sensing [49, 50]. Owing to the recent advances in micro/nano fabrication techniques [51], miniature sensors can be realized in smaller and smaller scales. As a popular miniature sensor platform, optical fiber based sensors have been extensively investigated because of their small sizes, light weight, flexibility, robustness to electromagnetic interference, and remote sensing ability [49]. However, as the size of a conventional optical element gets closer to the operating wavelength, the size of fiber-optic sensors seems irreducible due to the diffraction limit [52]. Nevertheless, recent studies on surface plasmons (SPs) shed some light on the realization of optical devices with an even smaller form factor. SPs are electromagnetic wave induced collective oscillations of free electrons on a metal/dielectric interface with a wavelength shorter than that of the incident light, which enable the confinement and manipulation of light at the subwavelength scale [14]. With the help of SPs, sensors with excellent sensing ability and ultra-thin film configurations have been demonstrated, including SP resonance [53], localized SP [54], and plasmonic interferometer based sensors [55]. Recently, the facet of an optical fiber tip is found

to be an appealing platform to integrate plasmonic structures for sensing applications [56, 57]. However, all of these sensors are either limited to single parameter sensing or can be sensitive to multiple parameters but are not capable of distinguishing different parameters.

On the other hand, sensors with multi-parameter sensing ability become more and more important, since in practical situations the measured parameters are often coupled with each other. Therefore, sensor designs that can distinguish different parameters in a single measurement are highly desirable. Over the last decade, a number of multi-parameter fiber-optic sensors have been presented [108, 111, 116, 144-148]. There are generally two methods. One method is to include additional sensing elements to measure different parameters, such as dual Bragg gratings in a fiber [145], cascaded Fabry–Pérot (FP) cavities [146, 147], and fiber Bragg grating (FBG) cascaded to a photonic crystal fiber interferometer [148]. Consequently, this method will increase the size of the sensor. Another method is to utilize multiple modes that are distinctively responsive to different parameters. As a result, multiple parameters can be discriminated by using a sensitivity matrix [108, 116, 144, 147]. However, all these sensors utilize conventional optical components with a relatively large sensor size.

In this chapter, a novel miniature on-fiber multi-parameter sensor based on a plasmonic interferometer is presented. The sensor consists of a two-dimensional (2D) nano-hole array pattern fabricated on a silver film deposited on a cleaved fiber facet, as shown in Figure 4.1. The nano-hole array induces SPs, which propagate at the interface of metal and silica, resulting in plasmonic interference of the multiple

reflections at the boundaries of the finite-sized pattern. Owing to the distinct responses of the SP resonance and the plasmonic interference to temperature and refractive index, simultaneous measurements of temperature and refractive index can be achieved, which are the essential sensing parameters in many biomedical applications [149, 150].

In addition to the plasmonic structure on SMF, we also investigate a multimode fiber (MMF) with a planar grating for the multi-parameter sensing purpose, which might be found useful for the sensing application in an extremely harsh environment.

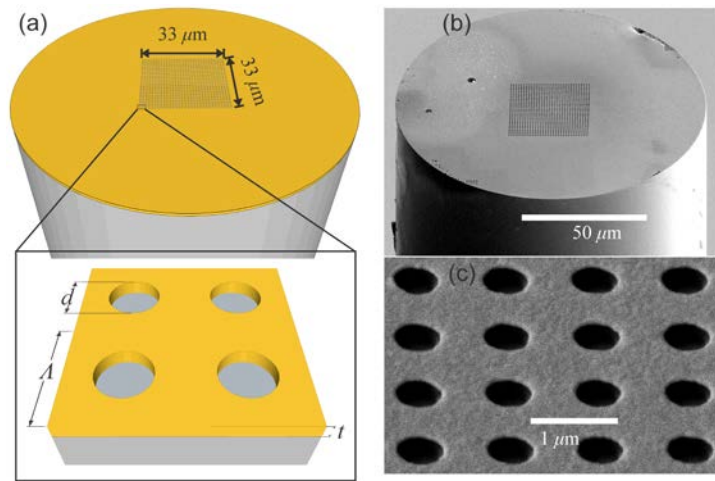


Figure 4.1(a) Schematic of on-fiber plasmonic interferometer with nano-hole array. The inset shows the unit cells of the array ($t=150$ nm, $d= 528$ nm and $\Lambda = 1055$ nm). (b) SEM of the fabricated sensor. (c) SEM of the nano-hole array.

4.2. On-fiber plasmonic interferometer design and fabrication

To fabricate the on-fiber plasmonic interferometer illustrated in Figure 4.1(a), a single mode fiber (SMF28, Corning) [151] was first cleaved with a typical cleave angle of $\pm 0.5^\circ$. Next, a silver film with a thickness of $t=150$ nm was deposited on the cleaved facet by magnetron sputtering. Further, a focused ion beam (FIB) (Helios 650, FEI) milling was used to write the nano-hole array pattern on the silver film

around the fiber core region. The diameter d of the individual hole was designed to be 528 nm and periodicity Λ is 1055 nm. The entire array pattern consists of 31×31 units with an overall patterned area of $d \times d$ ($\approx 33 \mu\text{m} \times 33 \mu\text{m}$). This design ensures the following: i) SPs can be excited around the optical communication wavelength of 1550 nm, ii) a proper free spectrum range is obtained to observe multiple fringes in our spectrum range, iii) the SP resonance will not be degraded by the finite pattern size [152, 153], and iv) the entire core area of the fiber is covered by the hole array. The scanning electron microscopy (SEM) pictures of the fabricated device are shown in Figure 4.1 (b) and (c).

The reflection spectrum of the fabricated device was measured by using an optical sensing interrogator (SM130, Micron Optics) with an uncertainty of 1 pm in the wavelength range from 1510 nm to 1590 nm. The remote sensing configuration was used, so that both incident light and the reflected signal can be guided through the fiber, as shown in Figure 4.2(a). A polarization controller was used in the light path to control the light polarization. The measured reflection spectra were normalized by the reflection spectrum of a fixed fiber mirror (a cleaved fiber with 150 nm silver deposited without patterning). Note that the nano-hole array structure was designed to be polarization independent, since the 2D symmetric structure is illuminated under normal incidence through the fiber. A typical reflection spectrum of the sensor is shown in Figure 4.2(b), which is a result of two mechanisms: SP resonance and plasmonic interference. The incident light first interacts with the hole array structure. Due to the grating diffraction of the nanopattern, momentum

matching can be achieved, which leads to effective coupling from incident light to SPs at the resonant wavelength [125]:

$$\lambda_{resonance} = \Lambda \sqrt{\frac{\epsilon_d(\lambda)\epsilon_m(\lambda)}{\epsilon_d(\lambda) + \epsilon_m(\lambda)}}, \quad (4.1)$$

where ϵ_d and ϵ_m are the permittivities of silica and silver, respectively. Moreover, the individual holes could act as elementary scatters, which enables broadband excitation of surface waves [see Figure 4.2(e)], resembling the spoof/hybrid surface plasmons (SSPs)[154-156] counter-propagating on the hole-array structures. These surface modes will be reflected at the boundaries of the hole array pattern, resulting in an interference effect of surface waves propagating at the metal-fiber interface. It should be noted that the SSPs could be re-scattered through the individual holes, and their signals can be collected and guided through the optical fiber. From the fringe pattern shown in the fiber reflection spectrum [Figure 4.2(b)], it indicates that the interference effect of SSPs on the fiber end-face can be measured and characterized in the far field. Therefore, the sensor can act as a plasmonic interferometer [55, 75, 98] as well as a SP resonator. It should be noted that SP resonance is usually accompanied with Wood's anomalies in long wavelength region [157]. The Wood's anomaly happens at the wavelength predicted by $\lambda_{Wood's} = \Lambda\sqrt{\epsilon_d(\lambda)}$, which is close to the SP resonance but at a shorter wavelength.

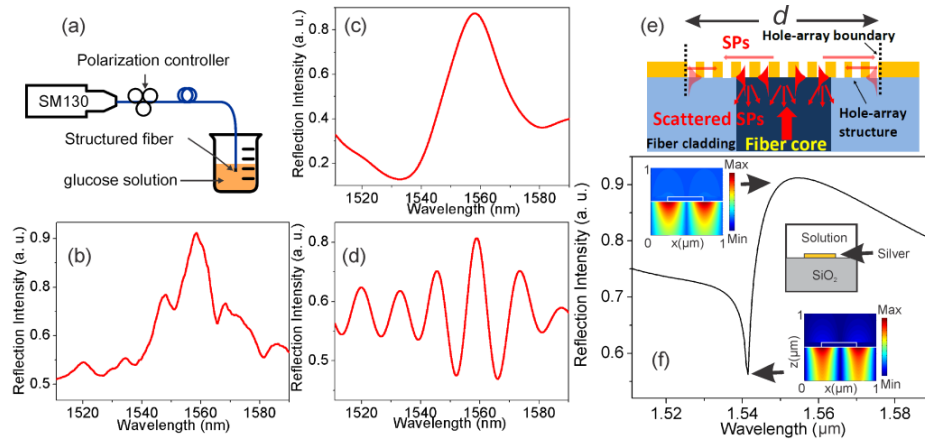


Figure 4.2(a) Schematic of the experimental setup, (b) typical reflection spectrum of the sensor in glucose solution at room temperature (glucose concentration 10%), (c) reflection spectrum of SP resonance extracted from (b), (d) reflection spectrum of plasmonic interference extracted from (b), (e) schematic of the on-fiber plasmonic interference, (f) reflection spectrum obtained with RCWA simulations for a hole array structure of infinite size in a 10% glucose solution. The insets show the field distributions at the SP resonance peak and the Wood's anomaly dip in one unit cell.

To clearly observe the two different mechanisms from the reflection spectrum, fast Fourier transform (FFT) of the measured spectrum is performed and the corresponding spatial frequency spectrum (i.e., wavenumber spectrum) is obtained [116, 146]. It is noted that the SP resonance mainly affects the low spatial frequency components while the plasmonic interference contributes to the higher spatial frequency components of the spatial frequency spectrum. Therefore, after filtering out DC component in the spatial frequency spectrum, we applied two bandpass filters to the first and second peaks the spatial frequency spectrum and performed inverse FFT. Two distinctive spectra corresponding to the SP resonance effect [Figure 4.2(c)] and plasmonic interference [Figure 4.2(d)] can be obtained, respectively. Figure 4.2(c) shows an asymmetric Fano line shape of the spectrum, which clearly indicates a SP resonance peak accompanied by a Wood's anomaly dip at a shorter wavelength. On

the other hand, Figure 4.2(d) clearly indicates the periodic fringes of a Fabry-Perot (F-P) interferometer due to the plasmonic interference. To validate the influence of SP resonance, a rigorous coupled-wave analysis (RCWA) simulation was conducted for a nano-hole array structure with the same hole diameter and periodicity as the fabricated device but an infinite size, shown in Figure 4.2(f). Due to the excitation of SPs, a resonance peak can be found around 1553 nm in the reflection spectrum, which agrees well with the theoretical prediction using Eq. (4.1) (≈ 1542 nm). Further, it can be seen that the spectrum obtained with RCWA simulations exhibits an asymmetric Fano line shape, which matches with the filtered experimental spectrum shown in Figure 4.2(b). The experimentally measured resonance peak is about 1558 nm, which agrees well with the theoretical prediction and numerical simulation.

4.3. On-fiber plasmonic interferometer fabrication and sensing measurement

To demonstrate the multi-parameter sensing ability of the on-fiber plasmonic interferometer, the responses of the sensor was characterized with respect to refractive index of the environment and temperature changes. In the refractive index experiments, the sensor was immersed in glucose/water solution. By changing the concentration of glucose solution to 5 %, 10 %, 15 %, 20 %, and 25 %, the refractive index of the solution was tuned to 1.3382, 1.3448, 1.3506, 1.3575 and 1.3623 respectively. The refractive index of the solution was calibrated by using a refractometer (Digital Brix/RI-Chek, Reichert) with an uncertainty of 4.1×10^{-5} (note the uncertainties discussed in this paper are defined by the coverage factor $k=1$ [158]). The temperature measurements were conducted in air by using a temperature control chamber that allows us to accurately calibrate temperature. The device was

sandwiched between two polyimide-insulated flexible film heaters (KH 103/10, Omega Engineering Inc.) and the temperature control was achieved by using a temperature controller (CN77333, Omega Engineering Inc.) with a film thermocouple (CO1-K, Omega Engineering Inc.) as the reference that has a measurement uncertainty of 0.4 °C.

Further, the spatial frequency filtering method was used to extract the spectra dominated by two different mechanisms discussed previously. For refractive index measurements, Figure 4.3(a) shows the filtered spectra dominated by the SP resonance. The SP resonance exhibits a red shift with increasing refractive index of the solution, which is consistent with the prediction of Eq. (4.1). By tracing the shift of SP resonance, the refractive index of the solution can be determined. Here, the Wood's anomaly dip was not used to obtain the refractive index change. Instead, the SP resonance peak was chosen, since it is more sensitive to the refractive index change. This can be explained by using the field distributions obtained at the SP resonance peak and the Wood's anomaly dip [insets of Figure 4.2(f)]. At the Wood's anomaly, light is mostly confined in the SiO₂ region, while around the SP resonance more evanescent field can extend into the environment (solution region). Hence the SP peak is more sensitive to the environmental changes. Figure 4.3(b) shows the obtained peak wavelength shift with respect to the refractive index change. The estimated sensitivity is 220 nm/RIU with an uncertainty of 2.1 %. All the sensitivity uncertainties calculated here are standard deviations based on the linear fits. Similarly, the high spatial frequency contribution from plasmonic interference was extracted [see Figure 4.3(c)]. By tracking the peak around 1545 nm, the effective

optical path difference (OPD) for the interference was obtained by using the one peak tracing method [159] [see Figure 4.3(d)]. The effective OPD increases with increasing the refractive index. The sensitivity of effective OPD with respect to the refractive index change of the environment was determined to be 1700 nm/RIU with an uncertainty of 17.2 %. Due to the short wavelength span of SM130 (80 nm), the resolution of spatial frequency spectra is limited, which causes the fluctuation in Figure 4.3(d). Nevertheless, we still use the linear fit because of the underlying mechanism. It is known that $OPD=2n_{eff}d$, where d is the pattern size and n_{eff} is effective refractive index of surface plasmon modes on the hole array structure. Since the effective refractive index is proportional to the environmental dielectric refractive index in the infrared region ($n_{eff} \propto \sqrt{\epsilon_d}$) [160], the effective OPD should linearly change with the environment refractive index.

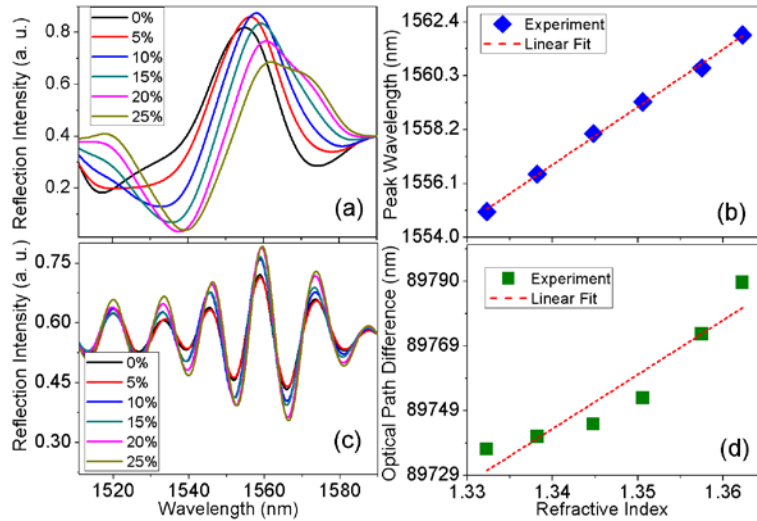


Figure 4.3(a) Extracted reflection spectra dominated by SP resonance with respect to refractive index change, (b) peak wavelength of the SP resonance versus refractive index, (c) extracted reflection spectra dominated by plasmonic interference with respect to different refractive indices, (d) effective OPD versus refractive index.

With the spatial frequency filtering method, the spectra obtained at different temperatures in air were also analyzed (see Fig. 4). As shown in Figs. 4(a) and 4(b), the peak wavelength due to the SP resonance manifests a blue shift as the temperature increases. This is because the negative thermo-optical coefficient of silver (on the order of $10^{-3}/^{\circ}\text{C}$ around 1550 nm [161]) dominates in the temperature measurement, compared with the thermo-optical coefficient of SiO_2 (on the order of $10^{-6}/^{\circ}\text{C}$ [162]) and thermal expansion coefficient of both silver and SiO_2 (on the order of $10^{-6}/^{\circ}\text{C}$ [163, 164]). The temperature sensitivity of the SP resonance was obtained as -60 pm/ $^{\circ}\text{C}$ with an uncertainty of 11.6 %. Furthermore, the effective OPD increases as the temperature rises [see Figure 4.4(c) and (d)]. The temperature sensitivity for the effective OPD was estimated to be 500 pm/ $^{\circ}\text{C}$ with an uncertainty of 9.7 %.

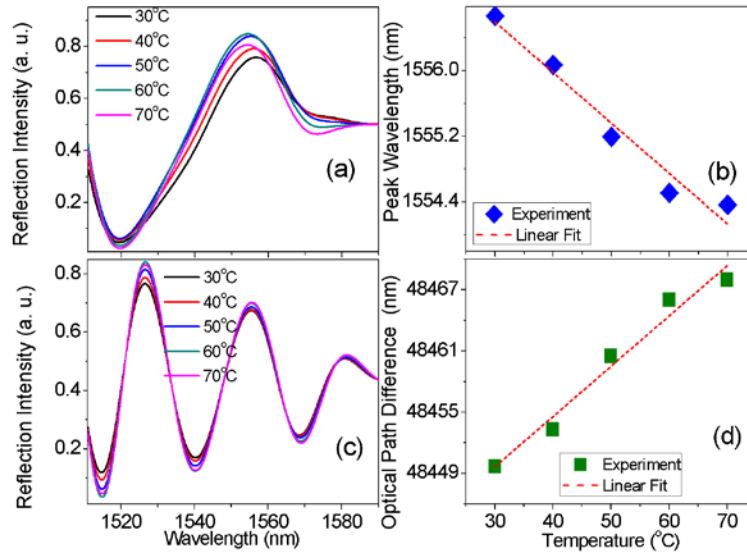


Figure 4.4(a) Extracted reflection spectra dominated by SP resonance with respect to temperature change, (b) peak wavelength of SP resonance versus temperature, (c) extracted reflection spectra due to plasmonic interference with respect to temperature change, and (d) effective OPD versus temperature.

In order to distinguish the refractive index and temperature in a single measurement, the sensitivity matrix method was used, in which the refractive index

and temperature changes (Δn , ΔT) as functions of the peak wavelength shift of the SP resonance and the effective OPD change ($\Delta\lambda$, ΔL) can be represented as .

$$\begin{pmatrix} \Delta n \\ \Delta T \end{pmatrix} = K^{-1} \begin{pmatrix} \Delta\lambda \\ \Delta L \end{pmatrix} = \begin{pmatrix} k_{\lambda,n} & k_{\lambda,T} \\ k_{L,n} & k_{L,T} \end{pmatrix}^{-1} \begin{pmatrix} \Delta\lambda \\ \Delta L \end{pmatrix} = \begin{pmatrix} 220\text{nm} / \text{RIU} & -60 \times 10^{-3} \text{nm} / ^\circ \text{C} \\ 1700\text{nm} / \text{RIU} & 500 \times 10^{-3} \text{nm} / ^\circ \text{C} \end{pmatrix}^{-1} \begin{pmatrix} \Delta\lambda \\ \Delta L \end{pmatrix}, \quad (4.2)$$

where K is the sensitivity matrix, $k_{\lambda,n}$ and $k_{L,n}$ are the refractive index sensitivities of SP resonance peak and the effective OPD, respectively, and $k_{\lambda,T}$ and $k_{L,T}$ are the corresponding temperature sensitivities, respectively.

Note that the $k_{L,n}$, $k_{L,T}$ are obtained only for facilitating the multi-parameter sensing and discriminating the temperature and refractive index change. In terms of wavelength shift, the SP resonance gives much larger sensitivities as the primary system sensitivities for refractive index and temperature measurements. For the SP resonance, the obtained refractive index sensitivity of 220 nm/RIU is comparable to the localized SP sensor on a fiber facet working in the visible region [56]. Moreover, the temperature sensitivity of -60 pm/ $^\circ$ C is six times higher than that of a FBG temperature sensor [165].

4.4. Discussion for on-fiber plasmonic interference

The geometries of the hole-array structure could play an important role to modify the surface plasmons (SPs) dispersion relation, and therefore can influence the plasmonic interference effect. The fringe patterns appear in the reflection spectrum [see Figure 4.2(d)] clearly indicates the interference effect of SPs, which may be characterized by an effective F-P resonance equation:

$$k_{sm}(\omega) \cdot d - 2\varphi(\omega) = m\pi. \quad (4.3)$$

Here, $k_{sm}(\omega)$ is the wave-vector of the SPs, d is the total size of the hole array pattern, $\varphi(\omega)$ represents the phase shift due to the SPs reflection at the boundaries of the hole array structure. $m=1, 2, \dots$ a positive integer, corresponding to the F-P mode orders. Since the SPs are re-scattered on the fiber hole-array interface, the far-field measurement of the spectrum fringing pattern will carry information about the SPs modes, and the dispersion relation of the SPs may be extracted (estimated) from the fringe patterns of the reflection spectrum by using the following approximation equations:

$$d(2\pi/\lambda_i)n_i - 2\varphi_i = (m+i) \cdot \pi, \quad (4.4)$$

where $i=1,2,3,\dots$ represents the fringing order numbers, λ_i is the mode wavelength corresponding to the fringing peaks in the reflection spectrum, n_i is the effective refractive index of the SPs. For closely spaced fringes in the spectrum, the phase-shift difference between these modes (e.g. i and $i+1$) is assumed to be small, and approximates as $\varphi_i \approx \varphi_{i+1}$. On the other hand, since the SPs with larger wavelength will be relatively insensitive to the surface corrugations (patterns), the SPs on the hole array in the long wavelength region (e.g. λ_i) may behave like a surface plasmon mode propagating on a flat metal surface, and approximately satisfy the relation $n_i \approx n_{sp} = \sqrt{\varepsilon_m \varepsilon_d / (\varepsilon_m + \varepsilon_d)}$. Based on the Eq. (4.4) and the above approximations, the effective refractive index n_i of the SPs can be estimated from the fringing patterns obtained from the experiment measurements:

$$n_{i+1} = \lambda_{i+1}/2d + n_i/\lambda_i \quad (4.5)$$

and the dispersion relations of the SPs can be obtained as

$$k(f_i) = n_i 2\pi/\lambda_i, \quad (4.6)$$

where f_i corresponds to the frequency of SPs. As shown in Figure 4.5, in the low frequency region, the dispersion curve of SPs approaches the dispersion line of surface plasmon on the flat silver surface, while at high frequency range the dispersion of SPs starts to deviate from the flat surface dispersion. Therefore, it is evident from the experiment that the hole-array structure will modify the dispersion properties of SPs as compared with surface plasmon propagating on a flat metal surface, this bears a resemblance of spoof or hybrid surface plasmons supported by the hole array structures [154-156]. The reflections of SPs at the boundaries of the hole array pattern is due to their wave impedance mismatch (refractive index difference) in the hole array region and outside the hole array pattern. It is expected that the geometries of the hole array structure, including the size, shape and depth of the individual holes as well as the periodicity of the array could modify the dispersion relation of the SPs [156], and therefore will influence the effective Fabry-Perot resonance due to the plasmonic interference effect. Here, it should be emphasized that the experimental results and the above analytical model can provide us a good physical understanding of the on-fiber plasmonic interference effect, however, they may not accurately characterize the influences of hole array geometries on the free-spectrum-range (FSR) and finesse of the plasmonic F-P cavity. The accurate and comprehensive analysis of these properties should rely on more rigorous numerical simulations (e.g. 3D FDTD model), which is however beyond the scope of current work.

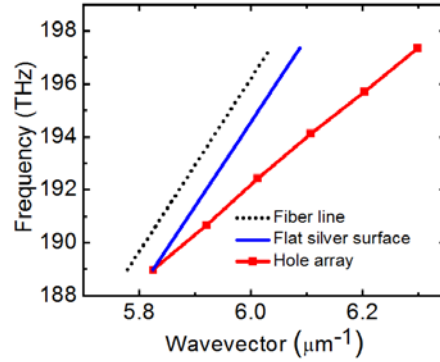


Figure 4.5 The comparison of dispersion relations of surface plasmons on the hole array structure and on the flat silver surface. The dashed line represents the light dispersion in the fiber core region

In summary, an on-fiber plasmonic interferometer with nanohole array structures has been successfully demonstrated for multi-parameter sensing. This device can excite SPs in the optical communication wavelength range and induce plasmonic interference due to the finite pattern area. The influences of two different mechanisms (i.e., SP resonance and plasmonic interference) on the reflection spectrum have been studied and utilized as a novel mechanism for multi-parameter sensing on a miniaturized sensing area. To the best of our knowledge, this is the first time that high sensitivity, simultaneous sensing of refractive index (220 nm/RIU) and temperature (-60 pm/ °C) has been achieved by using such a compact device. Owing to the ultra-thin sensing element (≈ 150 nm thick) with a small sensing area ($\approx 33 \mu\text{m} \times 33 \mu\text{m}$), our sensor has a much smaller volume than conventional fiber optic sensors. Moreover, the sensing is based on the measurement of SPP evanescent fields, thus enabling a very short light-sample interaction depth of about 1 μm . This enables the capability of measuring the refractive index of femto-liter samples ($\approx 33 \mu\text{m} \times 33 \mu\text{m} \times 1 \mu\text{m}$) and at the same time provides a high spatial resolution for temperature sensing. This work renders a new paradigm for the realization of ultra-miniature

multi-parameter optical sensors, which can impact many fronts, such as biological and chemical sensing, biomedical diagnostic, and environmental sensing.

4.5. Multi-parameter sensing with a planar grating on the facet of a multimode fiber

In addition to a 2D hole array on an SMF end face, a planar grating on a multimode fiber (MMF) for the multi-parameter sensing purpose. Compared with SMFs, MMFs have larger core diameters, which can support multiple modes traveling in the core region. Typically they have larger numerical apertures and higher energy density than SMFs. Since sapphire fibers, which can bear high temperature up to 2000 °C, are mostly multimode at the wavelength of visible to near-infrared range. Here, MMFs are chosen as proof-of-concept platform for multi-parameter sensing in high temperature harsh environment. This study can be potentially extended to study Sapphire fibers for multi-parameter sensing in high temperature harsh environments.

Different from SMFs, MMFs enable multi-mode interference in the core region, which dominates the spectrum features. Therefore, the cladding modes and buffer-guided modes, which will be discussed in Chapter 5, can be negligible in the MMF cases. The multi-mode interference, which happens in the core region with no contact with outside medium environment, is affected by the intrinsic fiber material property. Therefore, multi-mode interference can be used for temperature sensing [107, 166, 167]. Here, a planar grating supported SP resonance on the MMF facet is used to sense the refractive index change, as discussed previously with SMFs.

The fabrication process is similar to the hole array structure on a SMF facet. However, to investigate the future potential of high temperature sensing, platinum

instead of silver is used in this case. To enhance the metal adhesion a 10-nm-thick chromium is firstly deposited at the fiber facet. After that, a 90 nm platinum film is deposited. A MMF (50/125, Corning), which has a core diameter about 49.5 μm and a cladding diameter about 125 μm is used for sample preparation. FIB is used to directly develop grating patterns on the MMF end face. In the end, a one-dimensional (1D) grating of 30 units is fabricated on a Cr/Pt film at the fiber end face. The width and length of one individual unit are about 530 nm and 40 μm , respectively, and the periodicity Λ of the grating is 1050 nm. The overall pattern area, about 30 $\mu\text{m} \times 40 \mu\text{m}$, is aligned with the center of the MMF and covers most of the core area, as seen in Figure 4.6. The metal grating serves two functions here: 1) increase the reflection power at the fiber end face to enhance the multi-mode interference to be clearly observed in the wavelength range around 850 nm, 2) excite SPs around the optical communication wavelength of 1550 nm. Note that two different wavelength regions are used to characterize the multi-mode interference and SP resonances in the MMF case.

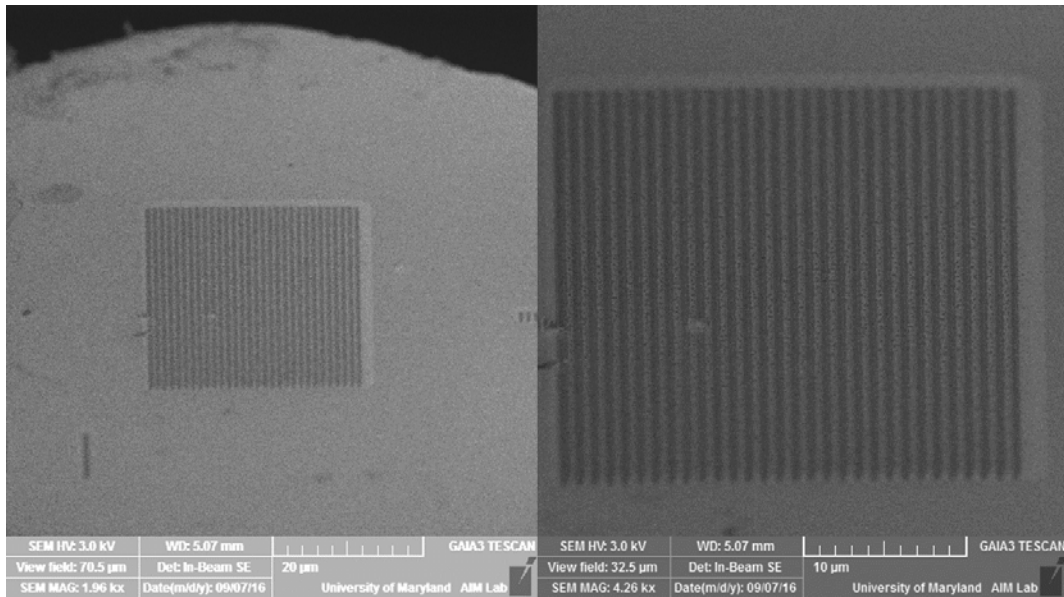


Figure 4.6 SEM pictures of the planar grating fabricated on a MMF end face.

The schematic of the multimode interference in the MMF fiber sensor is shown in Figure 4.7. The MMF with a planar grating is connected with a SMF with a FC/PC fiber connector to connect to a reflection spectrum measurement system, such as in Figure 4.2(a). As the light is coupled into the system through the SMF, it scatters at the SMF/MMF interface, due to the large core diameter mismatch. The guided mode in the SMF now is converted into multiple modes traveling along the MMF, reflecting back at the platinum film on the fiber end face, and eventually coupling back to the single mode at the SMF/MMF interface. After all that, the multimode interference is formed and can be found in the reflection spectrum of the sample.

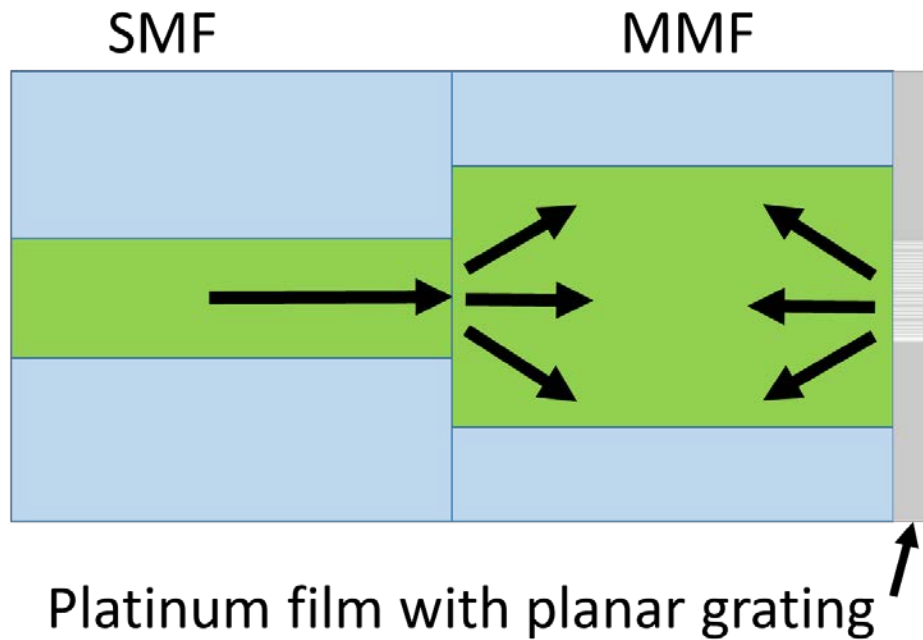


Figure 4.7 Schematic of multimode interference.

To measure multimode interference around 850 nm, a 30 cm long MMF with the planar grating at the facet was studied with a broadband light source (HL-2000, Ocean Optics) and a spectrometer (USB4000, Ocean Optics). The multimode interference was measured at around 850 nm wavelength to avoid the influence of SP resonance. Since the planar grating structure has a similar period to the 2D hole array that was previously discussed, the SP resonance appeared at the same wavelength of ~1550 nm. Therefore, if the spectrum is measured at around 850 nm, there will be only the effect of multimode interference. The temperature response of the sensor was characterized by measuring the spectra under different temperature environment, shown in Figure 4.8(a). The temperature control used for the on-fiber plasmonic interferometer was applied here again. Multimode interference fringes can be clearly observed in the spectra. As temperature increases, the multimode peaks exhibit red shift, which is consistent with the observations reported in previous literature [107,

166]. It is easy to understand that the optical path difference of the multimode interference increases as the temperature increases. The peak around 830 nm was tracked under different temperatures to extract the temperature sensitivity of the sensor. The sensor was heated up from 30 °C to 100 °C by a step of 10 °C, and the spectrum was measured, which was used to obtain the peak positions. An hour was given before each measurement to allow the system to reach the thermal equilibrium. To test the repeatability, the sample was also measured as the temperature was cooled down. The peak positions under different temperature while the sample was heated up and cooled down were recorded, as shown in Figure 4.8 (b). It is found the temperature response is quite linear with a sensitivity of ~ 135 pm/°C.

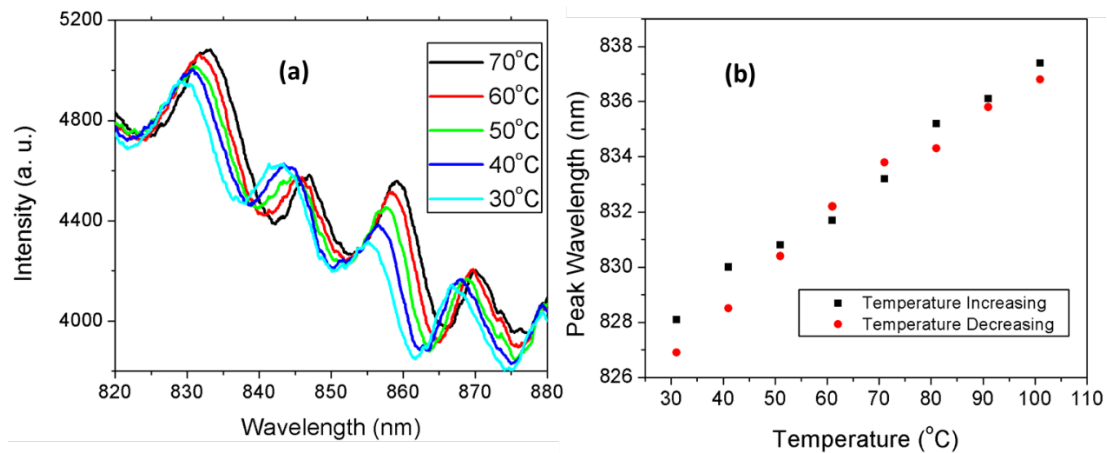


Figure 4.8 (a) reflection spectra of multimode interference with respect to temperature change (b) peak wavelength position as temperature increased (black)/decreased (red) over the range from 30 °C to 100 °C.

On the other hand, the refractive index change can be detected with this the planar grating fabricated on a MMF end face around the wavelength of 1550 nm, where SP resonance plays a role. To measure the spectrum of the sensor around 1550 nm, an optical interrogation system, shown in Figure 4.9, was used. This system measures the reflection spectrum of the structured sample by using a tunable laser

(TSL-550, Santec), a photodiode, and a fiber circulator (6015-3-FC, Thorlabs). This high power optical interrogation system was used, because the SP resonance from the planar grating on MMF was vastly affected by the multi-mode interference. In this case, the intensity of the multi-mode interference was too strong to dominate the SP resonance. Even with the help of spatial FFT, it was difficult to obtain the wavelength shift of SP resonance. However, the SP resonance still plays a role to influence the reflectance at a fixed wavelength as the refractive index of the environment media changes. Therefore, a light source with very stable intensity is required to detect the spectrum intensity change over different refractive index condition. The tunable laser used here has the power stability of $\pm 0.1\%$, and thus it is suitable for this application.

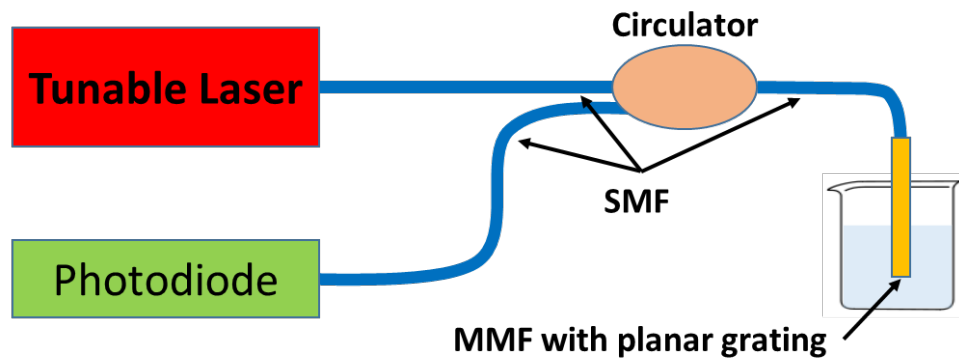


Figure 4.9 Schematic of the optical interrogation system with tunable laser

The spectra of the MMF with planar grating in air and in water were first measured, as shown in Figure 4.10. As can be seen, the multimode interference still plays a strong role in this wavelength range. However, the SP resonance exhibiting around the wavelength 1500 nm to 1540 nm should still change the reflection intensity while the refractive index of the environment changes from air to water. In the meantime, the multimode interference fringes will stay at the same position.

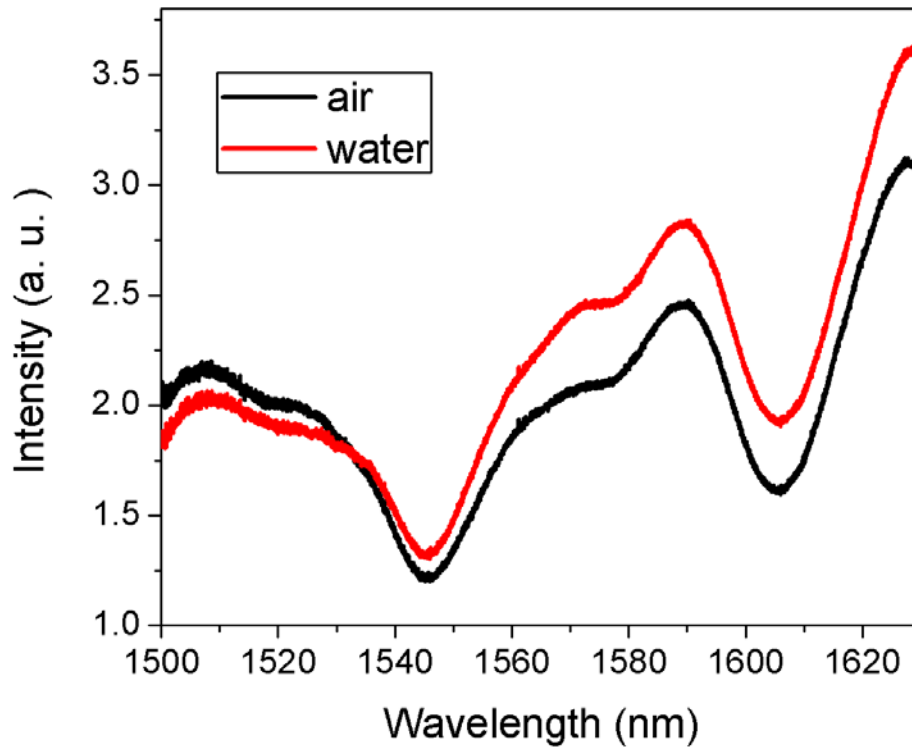


Figure 4.10 reflection spectra of the sensor in air and in water around 1550 nm

To test the intensity change under different refractive index environment, the spectra of the sample in IPA/water mixture with different concentration were measured. By changing the concentration of IPA/water solution to 0 %, 20 %, 60 %, and 100%, the refractive index of the solution was tuned to 1.3333, 1.3477, 1.3648, and 1.3776 respectively. The spectra exhibited clear intensity change in the range from 1500 nm to 1540 nm, which are shown in Figure 4.11 (a). With even a very small change of refractive index, the reflection intensity, which is under the influence of SP resonance, can be captured by the optical interrogation system. The reflection intensities at the fixed wavelength 1507 nm with different refractive indices are plotted in Figure 4.11 (b). With a higher refractive index, the reflection intensity becomes smaller. Thus, after calibration, the environment refractive index can be measured by tracking the reflection intensity at a fixed wavelength.

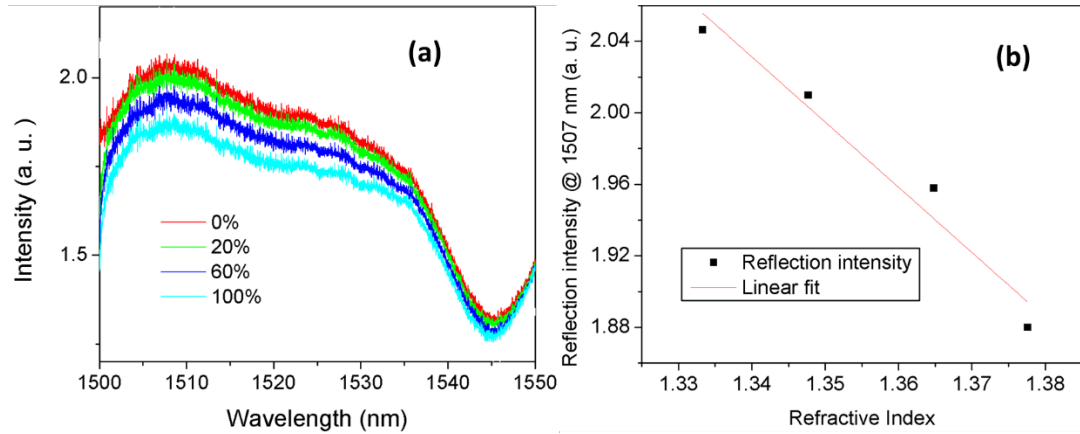


Figure 4.11 (a) reflection spectra of the sensor in IPA solution with different concentration, (b) reflection intensity at the fixed wavelength 1507 nm as the refractive index of the solution changes

Here, it has been demonstrated that the MMF with a planar grating at the facet of the fiber has the multi-parameter sensing ability. With the effect of multimode inference at the shorter wavelength around 850 nm, high sensitivity temperature sensing can be achieved. In addition, with the influence of the SP resonance in the longer wavelength region, the refractive index can be detected by monitoring the reflection intensity change at a fixed wavelength.

Nevertheless, in the real-world applications, intensity based sensing mechanisms are not always preferred. That is because many factors can influence it, such as laser power degradation, photodetector degradation, temperature, and humidity. Therefore, the wavelength shift based mechanism is still a better choice for the MMF case. The weak SP intensity in the MMF case results from the angle dependence of the SP resonance. Compared with the case of SMF, the broad range of the incidence angle on the MMF facet broadens the FWHM of the SP peak and lowers peak intensity. One possible solution in the future work is to design a plasmonic structure which can excite the localized SP resonance which is insensitive

to the incident angle. In that case, the localized SP intensity can be large enough to be distinguished from multimode interference, which enables the sensing by monitoring the wavelength shift.

Chapter 5. Cladding mode and buffer-guided mode excited by a planar grating on a fiber facet for multi-parameter sensing

5.1. Introduction of cladding modes and buffer-guided modes in SMF

While light travels in a SMF at the designed wavelength, most of the energy is confined in the fiber core region, propagating as the core mode (Figure 5.1, red line). On the other hand, cladding modes which confine energy in the cladding of a fiber can be supported at a shorter wavelength (Figure 5.1 blue line). These modes are generally undesirable for communication applications, although it is hard to generate cladding modes in general.

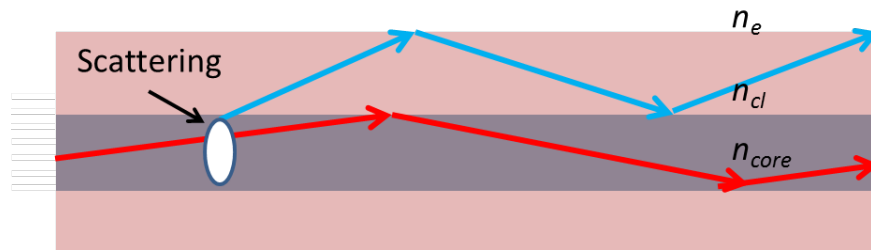


Figure 5.1 Schematic of core mode (red line) coupled to cladding mode (blue line) in a step-index SMF by scattering.

Nevertheless, cladding modes are found useful in the sensing applications. The field of cladding mode can penetrate into the medium and enhance the sensitivity to certain environmental parameters. For this reason, many methods have been developed to couple the core mode into cladding modes [60, 61, 109, 115]. The simplest way is to scatter the core mode by using some defect or a cavity in the fiber core as shown in Figure 5.1. Therefore some of the energy will be coupled into the

cladding mode. If there is another scattering objective downstream, it will couple the cladding mode back into the core mode to form a Mach-Zehnder interferometer and the inference spectrum can be observed in the transmission. By detecting the spectral change, the change of environment parameters can be measured. However, the coupling coefficient by scattering from a single objective is weak and the cladding mode is not easy to observe in the spectrum. Furthermore, the cladding modes can be easily removed by leakage loss when the fiber is coated with a material of index higher than the cladding. The FBG, on the other hand, has multiple scattering objectives. Light can be coupled into cladding mode and coupled back into core mode multiple times in the grating area. Thus the intensified interference spectrum similar to Figure 1.30 and Figure 1.31 can be easily observed. That explains why the sensors based on cladding modes were first demonstrated in the LPFG fibers [110], which support large coupling coefficient from core modes to cladding modes. However, the drawback of FBGs as sensors is that the length of FBG is too long, which limits their lateral resolution. To date, the shortest FBG sensors base on cladding modes are made with tilted fiber Bragg grating (TFBG) which is designed to shorten the grating length as well as enhance the core mode to cladding mode coupling coefficient [61].

Nevertheless, the length of TFBG is still about millimeters long.

On the other hand, the buffer layer of optical fibers typically serves as a mechanical protection to the glass surface. Unlike the core and cladding, the optical property of the buffer layer had not drawn much attention, since the light field is concentrated around the core region for most cases of optical communication and sensing, even for low order cladding mode cases. Since the early 1990s, the

whispering gallery mode (WGM) supported by the buffer coating has been recognized [68] after the studies of bend-induced losses [69, 70]. When an optical fiber is bent, the guided light in the core region can penetrate to the cladding and buffer regions, and later recouple coherently to the core mode, forming WGMs. Since its light field is extended to the cladding and buffer region, WGM provides a much easier way for the interaction between light and environment than the optic fiber sensors based on core modes. Therefore, WGMs have been extensively studied afterwards for the sensing applications. WGMs in the cladding region were used to enhance the sensitivity to the environment refractive index [168, 169]. Moreover, highly sensitive temperature sensors have been achieved by using WGMs in buffer based configurations [71-73]. As can be expected, the optical property of the buffer layer becomes very important in these cases, and hence, many efforts have been conducted to study the optical property of the buffer [68, 170-173].

Nevertheless, in most of the previous studies, a large fiber bending is needed to generate the WGMs in the buffer layer, which has two limitations. First, bending locally modifies the refractive index profile of core, cladding, and buffer [174]. Second, the bending radius needs to be precisely controlled and accurately measured to interpret the WGMs [68]. Due to these two problems, the buffer property extracted from WGM studies loses its generality. More importantly, the bending radius requirement limits the sensing capability of the buffer guided WGM. Most WGM sensors have only been demonstrated for detecting the parameters that do not involve the bending radius change (i.e., temperature and refractive index). Although there was

a study on the buffer property with a straight fiber [172], it requires spatial filtering of the core modes, which is impractical for most applications.

In this chapter, a novel method is proposed to simultaneously generate buffer guided modes and cladding modes in a straight single mode fiber by using a planar grating fabricated on the fiber end face. The planar grating diffracts light guided in the core into the cladding and buffer regions. By studying the interference resonances in the reflection spectrum resulting from buffer guided modes and cladding modes, the optical property of buffer layer can be extracted. Furthermore, this method enables a sensor with the capabilities of simultaneous, high-sensitivity temperature and axial strain sensing. In addition, because of the different responses from buffer-guided-mode resonances and cladding-mode resonances, this system demonstrates the potential for multi-parameter sensing.

5.2. *Cladding modes and buffer-guided modes generated by using planar gratings*

Instead of fabricating periodic structures along the fiber core as those in FBGs, a metal grating structure is fabricated on the end face of a fiber. The configuration of the proposed sensor structure is illustrated in Figure 5.2. A single mode fiber (SMF28e+, Corning), which has a core diameter about 8.2 μm , a cladding diameter about 125 μm and a buffer coating diameter about 242 μm , is used for sample preparation. The fabrication process is similar to that used for the on-fiber plasmonic interferometer [175]. A one-dimensional (1D) grating of 50 units is fabricated on a silver film at the fiber end face. The width and length of one individual unit are about 650 nm and 53 μm , respectively, and the periodicity Λ of the grating is 1068 nm. The overall pattern area, about 53 $\mu\text{m} \times 53 \mu\text{m}$, is aligned with the center of the fiber and

is sufficiently big to cover the core area. The metal grating on the fiber facet serves the following two functions: 1) efficiently diffract the incidence core mode to cladding modes and buffer modes, 2) enhance the reflection power since cladding modes attenuate easily along the fiber. Note that the working wavelength of this structure should be shorter than that of the plasmonic interferometer, while the grating periods are similar. With a shorter wavelength, higher order diffractions can be achieved at the grating, which can eventually be coupled into higher order cladding modes as well as buffer-guided modes.

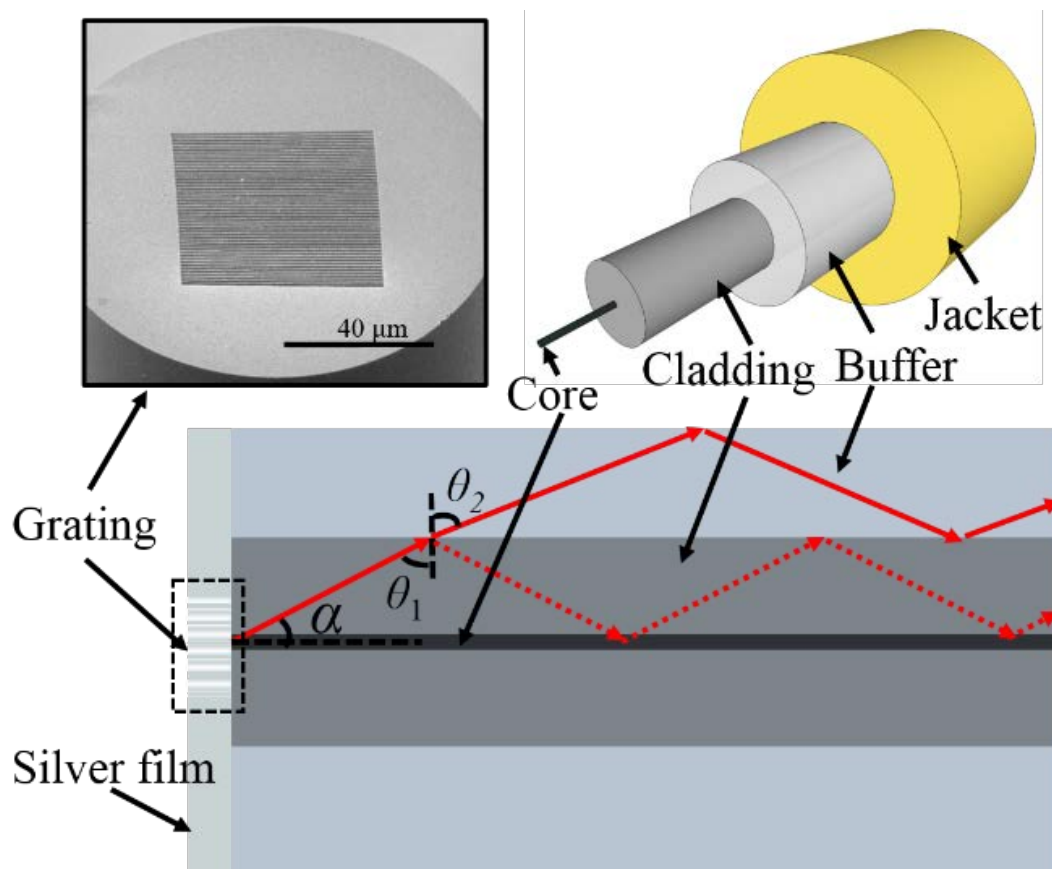


Figure 5.2 Schematic and SEM of the planar grating fabricated on a fiber end face to generate buffer modes and cladding modes.

In experiments, the fabricated fiber with a length of Z is connected with the optical interrogation system shown in Figure 5.3 (a), which measures the reflection

spectrum of the structured sample by using a broadband light source (HL-2000, Ocean Optics), a spectrometer (USB4000, Ocean Optics), a 2×2 coupler (Gould Fiber Optics), and single mode fibers (780 HP Thorlabs). A typical reflection spectrum is shown in Figure 5.3 (b). As can be seen, there are two types of interference resonances in the spectrum: the buffer-guided-mode resonances in the shorter wavelength range and cladding-mode resonances in the longer wavelength range. The underlying mechanism of simultaneously exciting buffer guided modes and cladding modes will be explained as follows, while two-dimensional simplification and linear polarization assumption are used.

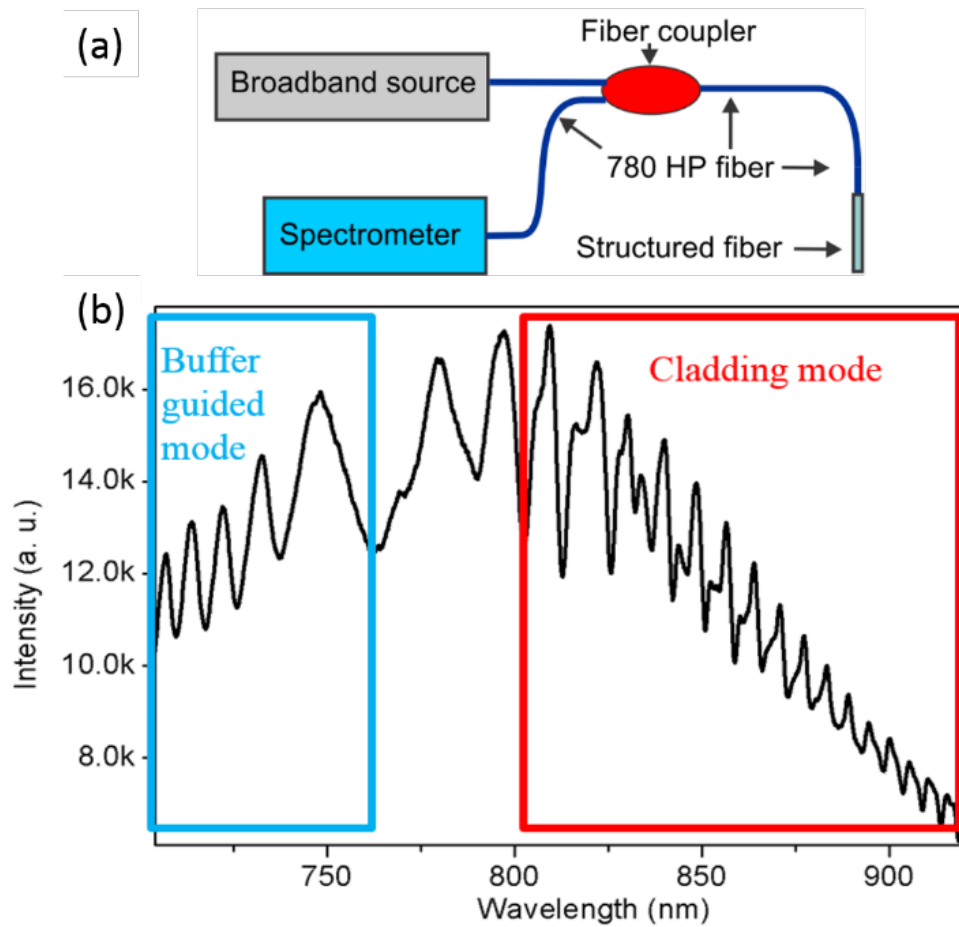


Figure 5.3 (a) Schematic of the optical interrogation system, and (b) a typical reflection spectrum of the sensor with $Z \approx 28$ cm.

While the core mode is guided through the fiber and used to illuminate the structured fiber end face, the grating on the silver film diffracts back the light with a diffractive angle of α , which can be expressed as [52]

$$\sin\alpha = \frac{l\lambda}{\Lambda n_{core}}, \quad (5.1)$$

where l is an integer representing the diffraction order, λ is the wavelength and n_{core} is the refractive index of the fiber core. Since most of the diffraction energy is in the first order, only $l=0$ is considered here. The diffracted light can penetrate into the cladding and buffer region and form buffer guided modes and cladding modes. Depending on the refractive indexes of cladding and buffer, buffer-guided-mode resonances and cladding-mode resonances can be found in different wavelength regions.

In the shorter wavelength region, where the refractive index in the buffer is larger than that in the cladding, light partially penetrates into the buffer region and forms guided buffer modes and cladding modes as illustrated in Figure 5.2. After traveling through the fiber of length Z , light is recoupled to the core due to the diameter mismatch between SMF 28e+ and 780 HP fibers. The optical path difference (OPD) between light traveling in buffer and cladding is

$$OPD = Z \left(\frac{n_2}{\sin\theta_2} - \frac{n_1}{\sin\theta_1} \right), \quad (5.2)$$

where n_1, n_2 are the refractive indexes of cladding and buffer, θ_1 and θ_2 are the incident angle and reflection angle shown in Figure 5.2. By considering the Fresnel equation and $\theta_1 = \pi/2 - \alpha$, Eq. (5.2) can be derived as

$$OPD = Z \frac{n_1}{\cos \alpha} \left(\frac{n_2^2}{n_1^2} - 1 \right), \quad (5.3)$$

The buffer-guided-mode resonances can be found in the reflection spectrum, where the OPD satisfies the constructive interference condition.

In the longer wavelength region, the refractive index in the buffer is smaller than that in the cladding, thus the diffracted energy is mostly constrained in the cladding region (i.e., cladding modes are dominated). The cladding mode yields to the step-index planar waveguide dispersion, and travels through the fiber with the angle $\theta_N = \cos(N\lambda/2D)$ [176] instead of θ_1 , where N is the cladding mode order and D is the diameter of the cladding. Therefore, the OPD can be expressed as

$$OPD = Z \frac{n_1}{\cos \theta_N} \left(1 - \frac{n_2^2}{n_1^2} \right). \quad (5.4)$$

Thus, in the longer wavelength region, the cladding-mode resonances can be found in the reflection spectrum, where the OPD satisfies the constructive interference condition.

On the other hand, the OPD at each resonance peak in reflection spectrums such as in Figure 5.3 (b) can be estimated by the free spectrum range $\Delta\lambda$ by $OPD = \lambda^2 / \Delta\lambda$ [52], as illustrated in Figure 5.4(a) for the cases of $Z \approx 10$ cm and $Z \approx 50$ cm. By combining with Eq. (5.3) in the shorter wavelength range or Eq. (5.4) in the longer wavelength range, the effective refractive index of the buffer as a function of wavelength can be extracted. For simplicity, assume $n_1 = 1.458$ in the whole wavelength range, since it is less dispersive than n_2 [172]. As a result, in the shorter wavelength range as shown in Figure 5.4 (b), all the three fiber length cases lead to similar results for the buffer refractive index since the buffer modes are determined by the same diffractive angle.

On the contrary, different length of the fiber selects different cladding modes [177] and results in different effective refractive indices of n_2 , shown in Figure 5.4 (c). Note that there are multiple branches of the dispersion relation. For example, it can be seen from the extracted result that there are three branches in the case of $Z \approx 10$ cm. This means that there are three cladding modes have been selected by the system parameters and excited in this wavelength range.

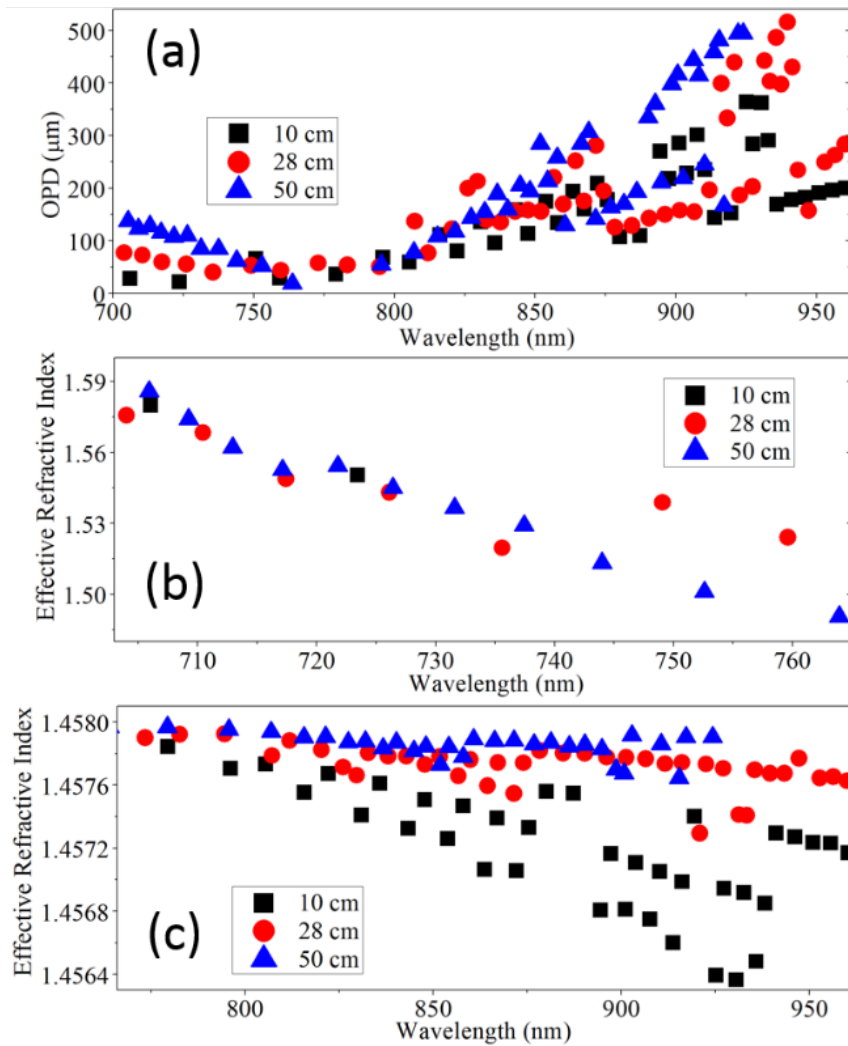


Figure 5.4 (a) OPDs extracted from the reflection spectrums for the cases of $Z \approx 10$ cm, 28 cm and 50 cm (b) effective refractive index of the buffer extracted from reflection spectrums in the buffer modes dominating wavelength range, and (c) effective refractive index of the buffer extracted from reflection spectrums in the cladding modes dominating wavelength range.

To further investigate the different mode resonances in Figure 5.3 (b), a finite-difference time-domain method based software (FDTD Solutions, Lumerical) has been used to obtain electric field distributions of the first few orders supported at a shorter wavelength (736 nm) and a higher wavelength (840 nm). As can be seen in Figure 5.5, at 736 nm, the buffer modes are supported in the system while the cladding modes dominate the system at 840 nm.

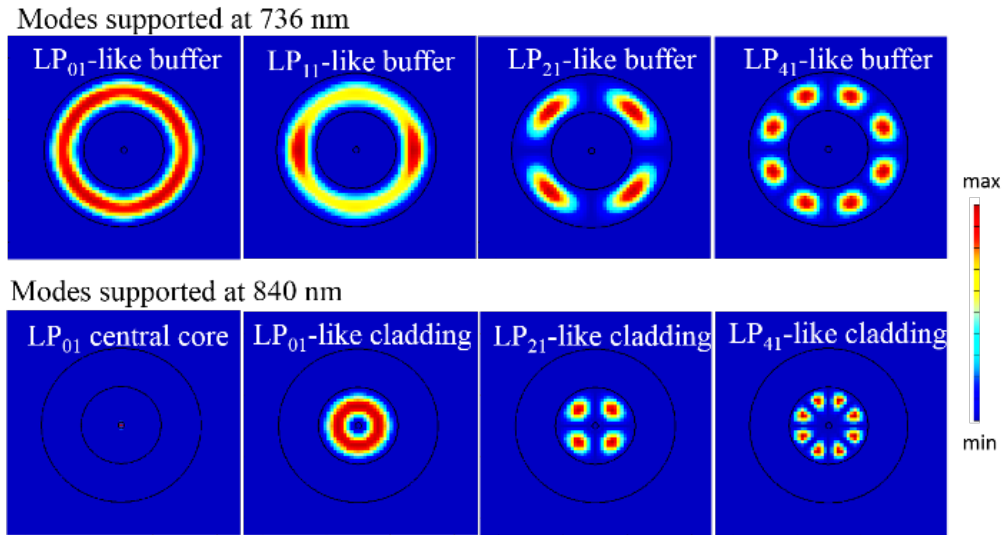


Figure 5.5 Electric field intensity distributions of the first few modes supported at 736 nm and 840 nm in the system.

5.3. Multi-parameter sensing

To characterize its temperature responses, the planar grating structured fiber with $Z \approx 28$ cm was put in a setup the same as used in our previous studies [175, 178, 179] with a temperature accuracy of 0.4 °C. Part of the fiber with the length of 7.5 cm was clamped by micro-heaters and was under temperature test from 22.2 °C to 55 °C. The reflection spectra with different temperatures were recorded, as shown in Figure 5.6 (a). From the spectra, it can be observed that the resonances in the buffer-

mode region have opposite response to the temperature, compared with the resonances in the cladding-mode region.

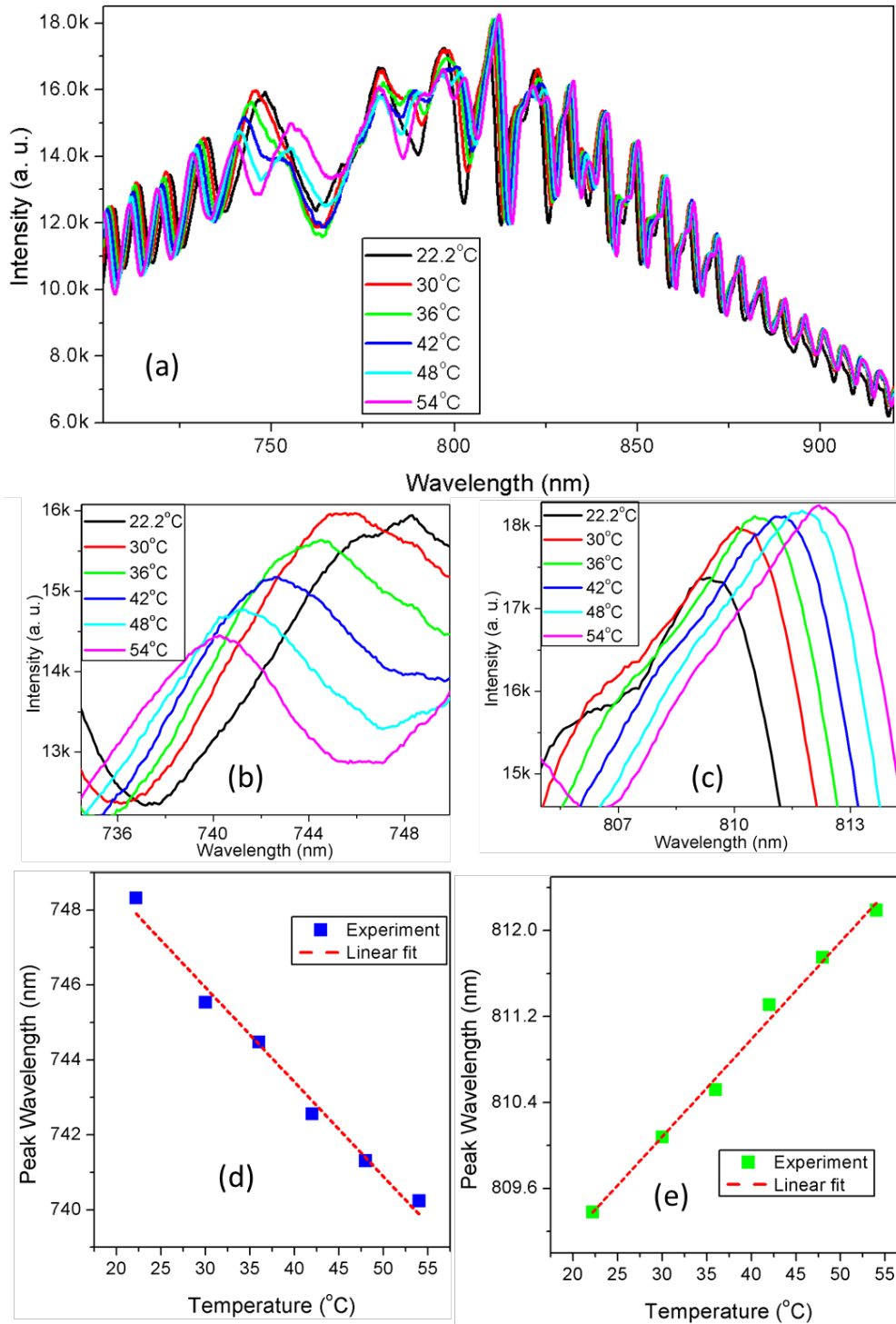


Figure 5.6 (a) the whole reflection spectra with respect to temperature change, (b) reflection spectra around peak A with respect to temperature change, (c) reflection spectra around peak B with respect to temperature change, (d) peak positions of peak

A with respect to different temperatures, (e) peak positions of peak B respect to different temperatures,

To characterize the temperature sensitivities, the buffer-guided-mode resonance around 740 nm (peak A) and cladding-mode resonance around 810 nm (peak B) were used. Due to different material properties of buffer and cladding, peak A and peak B exhibit blue shift [Figure 5.6 (b)] and red shift [Figure 5.6 (c)], respectively, as the temperature increases. Because of the polymer material properties of the buffer, a large temperature sensitivity of the buffer-guided-mode resonance was obtained as -252 pm/°C, shown in Figure 5.6 (d). The temperature sensitivity of the cladding-mode resonance was obtained as 91 pm/°C, shown in Figure 5.6 (e), which is also comparable with the highest sensitivities achieved by the cladding modes based on single mode fibers [180, 181].

To study the repeatability of the temperature measurements, three different sets of measurements were conducted. For each measurement, peak A and B were tracked, and the averaged results for peak A and B are shown in Figure 5.7 (a) and (b), respectively. As can be seen from the error bars, the temperature measurement is quite repeatable, and the estimate temperature accuracy is about 1.3 °C from peak A and 2.4 °C from peak B.

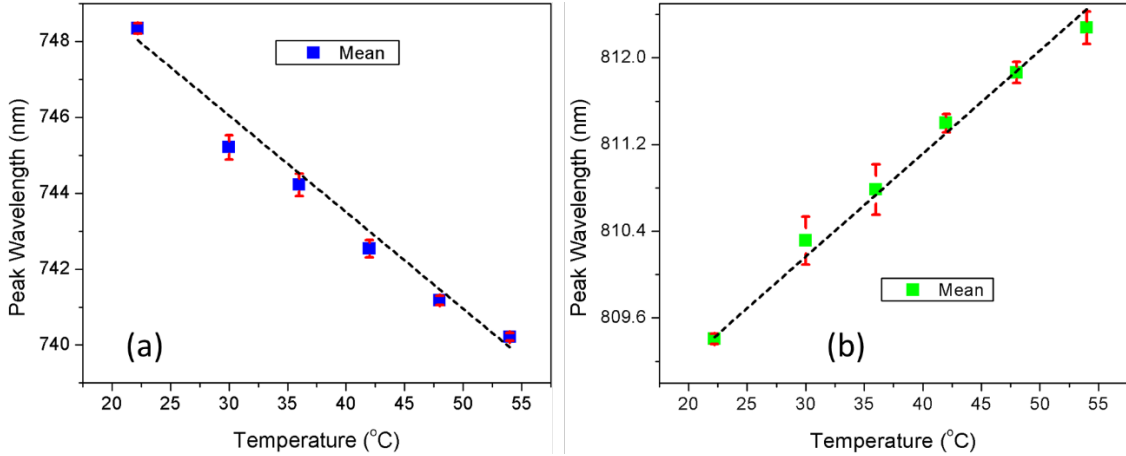


Figure 5.7 (a) mean peak positions of peak A with respect to different temperatures in three different measurements, (b) mean peak positions of peak B with respect to different temperatures in three different measurements.

Furthermore, the proposed structure for axial strain sensing is studied. The sample was loaded by using an ElectroForce test instrument (Bose 3330 Series II). Part of the fiber with the length about 8.8 cm was stretched by the translation stage. With displacement measurement resolution of a nanometer, the axial strain can be calculated. The whole reflection spectra with respect to different axial strain were recorded, as shown in Figure 5.8 (a). Similar to the temperature responses, the resonances in the buffer-mode region are found to have opposite response to the axial strain change, compared with the resonances in the cladding-mode region.

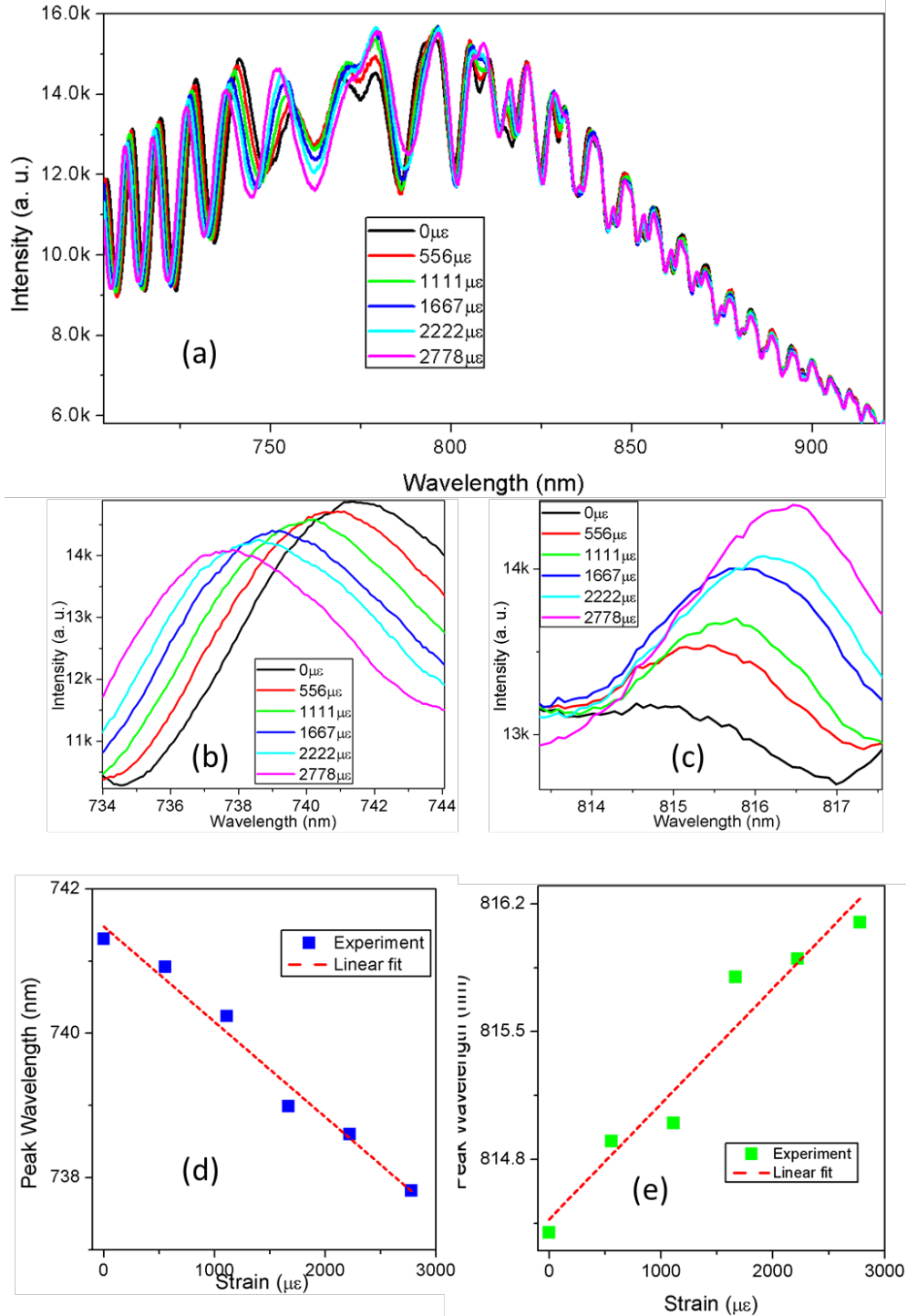


Figure 5.8 (a) the whole reflection spectra with respect to axial strain change, (b) reflection spectra around peak A with respect to axial strain change, (c) reflection spectra around peak B with respect to axial strain change, (d) peak positions of peak A with respect to different axial strains, (e) peak positions of peak B respect to different axial strains.

As the axial strain is increased from 0 to 2778 $\mu\epsilon$, peak A shifts to shorter wavelengths (Figure 5.8 (b)) and peak B shifts slightly to longer wavelengths (Figure 5.8 (c)). The axial strain sensitivity of peak A is about -1.32 pm/ $\mu\epsilon$ (Figure 5.8 (d)), which is similar to the axial strain sensor based on a polymer optical fiber [117]. The axial strain sensitivity of peak B is characterized as 0.54 pm/ $\mu\epsilon$ (Figure 5.8 (e)).

The repeatability study was also carried out for the axial strain measurements, as shown in Figure 5.9 (a) and (b). The estimated strain accuracy calculated from the error bars is about 317 $\mu\epsilon$ for peak A and 352 $\mu\epsilon$ for peak B.

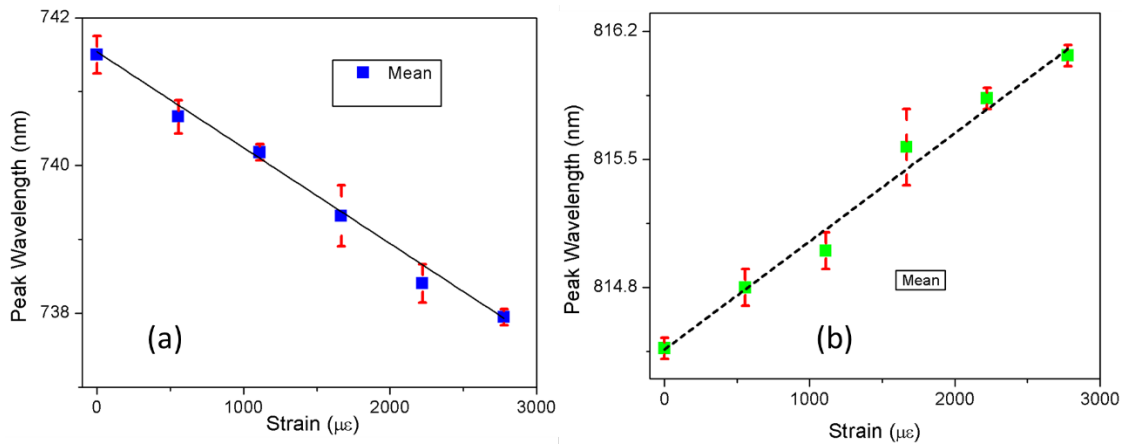


Figure 5.9 (a) mean peak positions of peak A with respect to different axial strains in three different measurements, (b) mean peak positions of peak B with respect to different axial strains in three different measurements.

In summary, it is demonstrated that the planar grating structured fiber can simultaneously excite buffer modes and cladding modes in a straight fiber, and this results in buffer-guided-mode resonances and cladding-mode resonances in the reflection spectrum. The buffer property of a fiber can be determined from these resonance positions. Moreover, in the shorter wavelength region, where the buffer modes dominate, the structured fiber exhibits high temperature sensitivity of -252 pm/ $^{\circ}\text{C}$ and high axial strain sensitivity of -1.32 pm/ $\mu\epsilon$, owing to the material

properties of the buffer. Whereas, the cladding-mode resonances in the longer wavelength region are found to have opposite sign of the temperature and axial strain sensitivities as $91 \text{ pm}/^\circ\text{C}$ and $0.54 \text{ pm}/\mu\epsilon$. The different behaviors of buffer-guided-mode resonances and cladding-mode resonances hold great promise for multi-parameter sensing in many applications.

Chapter 6. Summary

6.1. *Summary of the dissertation work*

Miniature imaging and sensing systems, which utilize conventional optical components, are limited by the diffraction limit. This poses a challenge for the development of high performance miniature imaging and sensing systems. Recently, nanophotonic structures have drawn great attention due to its ability to confine and manipulate light in the nanoscale. It sheds light on further improving the performance of miniaturized imaging and sensing systems.

In this dissertation, nanophotonic that can be used to enhance the performance of imaging and sensing in miniaturized systems are investigated. As one of the most important performance properties in an imaging system, enhanced focusing ability is first investigated. Theoretical study on the physical behaviors of plasmonic lenses in three different regions is carried out. The results from this study can help determine the design guidelines for a plasmonic lens. For proof-of-concept, a plasmonic lens is designed to obtain a sub-diffraction limit focus in the Fresnel's region. To further enhance the focusing ability, plasmonic structures with the ability to generate radial polarization through the TEM resonance are investigated. A plasmonic lens working in the surface plasmon dominating region, which is self-aligned with the radial polarization generating structure, is designed. In terms of sensing systems, an on-fiber plasmonic interferometer for the multi-parameter sensing is designed and fabricated.

The experiment study demonstrates its ability to simultaneously measure refractive index and temperature. Furthermore, the multi-parameter sensing ability of a MMF with a planar grating on its facet is demonstrated. The multimode interference at the shorter wavelength is utilized for the temperature sensing, while the SP resonance in the longer wavelength region is used to detect the refractive index change of the medium. In addition, a novel method to generate buffer-guided modes and cladding modes simultaneously in the reflection spectrum of a straight single mode fiber is studied by using a planar grating fabricated on the fiber end face. Temperature and axial strain sensing with high sensitivities are experimentally demonstrated with this structure.

The original contributions of this dissertation work are summarized as follows:

Contribution 1: An enhanced understanding of plasmonic lens is achieved. By the theoretical studies of plasmonic focusing in three regions, which are surface plasmon dominating region, Fresnel region, and Fraunhofer region, the boundaries of the three regions are defined and the physical behaviors of plasmonic lenses in terms of focal length and focus size in these regions are investigated. This can serve as a basis for understanding plasmonic focusing phenomenon and designing plasmonic lenses for various applications. A plasmonic lens that renders a sub-diffraction-limit focus in the Fresnel region is designed. The lens performance with respect to the design parameters is studied by using finite-difference time-domain (FDTD) simulations. In the surface plasmon dominating region, radially polarized light generated by the TEM mode in a

metal annular structure is studied. A novel plasmonic lens is designed to work in the surface plasmon dominating region with self-alignment to the radial polarization generating structure. The enhanced focusing ability in the near-field is demonstrated by numerical simulations. This plasmonic lens design might find applications in photolithography, imaging, and optical manipulation.

Contribution 2: A novel ultra-thin multi-parameter sensing device based on a plasmonic interferometer fabricated on a fiber facet in the optical communication wavelength range is demonstrated for the first time. This device enables the coupling between surface plasmon resonance and plasmonic interference in the structure, which are the two essential mechanisms for multi-parameter sensing. It is experimentally shown that these two mechanisms have distinctive responses to temperature and refractive index, rendering the device the capability of simultaneous temperature and refractive index measurement on an ultra-miniature form factor.

Contribution 3: A novel method which utilizes planar gratings on fiber facets to generate buffer-guided modes and cladding modes simultaneously in a straight fiber is developed for the first time. By studying the interference resonances in the reflection spectrum resulting from buffer guided modes and cladding modes, the optical property of the

buffer layer can be determined. More importantly, a new sensor based on these cladding and buffer-guided modes is fabricated and experimentally studied. It shows great temperature sensitivity and axial strain sensing ability. Moreover, because of the different responses from buffer-guided-mode resonances and cladding-mode resonance, the system shows the potential of multi-parameter sensing.

6.2. *Future work*

Upon the completion of this dissertation work, the future work is suggested as follows.

- 1) **Demonstration of multi-parameter sensing capability of a fiber optical sensor at a temperature above 1500 °C.** In this dissertation, we demonstrated the multi-parameter sensing capability of a MMF with a planar grating on the facet. With a proper selection of the materials of the fiber and metal film, a higher temperature fiber optical sensor with the ability to sense refractive index change of the environment can be achieved. The most straightforward choice is to choose a sapphire fiber to replace the MMF used in the dissertation, and still use platinum film for the grating. Due to the high temperature property of sapphire and platinum, the estimated working temperature of fiber optical sensor can easily go up to 1500 °C. This might find great applications in harsh environment monitoring. For example, it can be used for measuring the temperature and gas concentration in a higher temperature combustion chamber.

2) **Fabrication and characterization of the multi-parameter sensing device based on simultaneously exciting cladding mode and buffer-guided mode with a planar grating on the fiber facet.** A new way to excited cladding modes and buffer-guided modes in the reflection spectrum by a grating on a fiber facet is explored in the dissertation. It has been demonstrated to serve as a new platform for multi-parameter sensing. Besides temperature and axial strain sensing discussed in this dissertation work, other parameters such as bending angle, twisting angle, and humidity are all possible parameters that can be measured by using this platform, since these parameters are closely related to the buffer property.

3) **Modeling, design, fabrication and experimental study the distribution sensing optical fibers with utilizing buffer-guided modes generated by the planar gratings.** Since it has been demonstrated that the reflection spectrum of the buffer-guided resonance depends on the property of the buffer coating, it is possible to achieve distributed sensing capability with implementing different buffer coatings at different locations.

Appendix A: Related numerical simulations and codes

A1. Plasmonic focusing lens with dielectric layers

A very preliminary simulation of a plasmonic lens with a dielectric substrate and a dielectric cover has been carried to discuss the problems of the suspending silver plasmonic lens we mentioned in Chapter 3.4.

Here, we design a near-field focusing lens with normal incident light and small focus size. In addition to the large annular aperture (radius $r=3000$ nm) milled on a silver film with thickness $t=570$ nm deposited on the SiO_2 substrate, a small annular aperture with radius 100 nm is added at the center. A 350 nm SiO_2 layer is deposited at the emitting sides of the aperture, as shown in Figure A.1. While the system is under the normal incidence of light at the wavelength of 758 nm, due to the constructive interface from the emitting light propagating in the SiO_2 from two ring slits, a focusing spot right at the interface of SiO_2 and air can be designed. Because of the high refractive index of SiO_2 , this focus has smaller focus size, compared with the plasmonic lens designed for the propagating media as air. From the cross-section field distribution shown, it can be seen that the focusing is at the interface of SiO_2 and air. And the simulated field distribution at the SiO_2 and air interface shows this focus size is small. This focusing structure may be found to be more practical than what we discussed in Chapter 3.4.

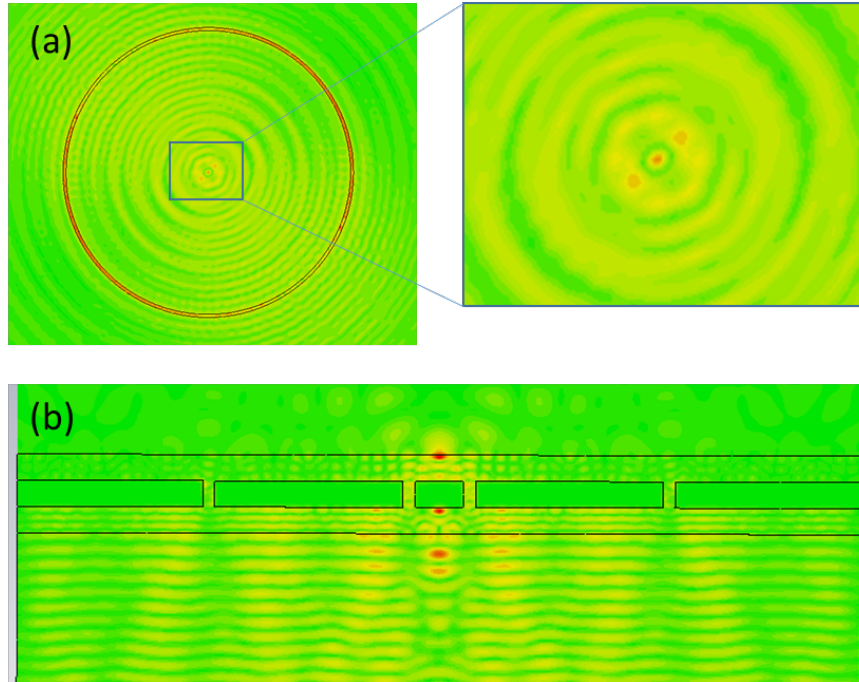


Figure A.0.1 (a) The field intensity distribution at the plane 10 nm distance away from the designed plasmonic lens surface, (b) and at the cross section, for $\theta=0^\circ$ and $\lambda=758$ nm.

A2. Matlab code for calculating the attenuation length of SP

```

%calculate the SP attenuation length of air/Pt interface
clc
lambda=700:1:900;
for ind=1:length(lambda)

[n(ind),k(ind)]= Rakic_Pt(lambda(ind)/1000);
em(ind)=(n(ind)+1i*k(ind))^2;

[nd(ind),kd(ind)]=Palik_SiO2(lambda(ind)/1000);
ed(ind)=(nd(ind)+1i*kd(ind))^2;

Lspp(ind)=sqrt((ed(ind)*em(ind))/(ed(ind)+em(ind)))*1055;
Lwa(ind)=sqrt(ed(ind))*1055;

end
plot(lambda,Lspp,'r');
hold on;
AA=[lambda;Lspp]';

%Pt property function, data from Palik handbook

function [n,k]=Rakic_Pt(lambda)

```

A=[0.2066 1.77403147162 1.48934816481
0.21089508319 1.74089031 1.48681627484
0.215279458439 1.7064516691 1.49075469521
0.219754982075 1.67153380755 1.5012003679
0.224323549012 1.63696149606 1.51806855129
0.228987093564 1.60354242845 1.54114377819
0.233747590255 1.57203802453 1.57007780763
0.238607054657 1.54313169628 1.60439744764
0.243567544248 1.5173990747 1.64352339818
0.248631159276 1.49528498058 1.68679884531
0.253800043655 1.47709078632 1.73352426366
0.259076385867 1.46297361192 1.7829936117
0.264462419893 1.452956361 1.83452724173
0.269960426156 1.44694578337 1.88749816335
0.275572732488 1.44475499622 1.94135013481
0.281301715116 1.44612713866 1.99560773024
0.287149799665 1.45075768149 2.04987963781
0.293119462189 1.45831392766 2.10385691533
0.299213230217 1.46845111275 2.15730791352
0.305433683824 1.48082512169 2.21007129054
0.311783456723 1.49510217769 2.26204816518
0.318265237381 1.51096599627 2.31319410267
0.324881770154 1.52812290634 2.36351134697
0.331635856454 1.54630538284 2.41304151463
0.338530355932 1.56527435442 2.46185883807
0.345568187689 1.58482056741 2.51006397124
0.352752331512 1.60476521634 2.55777833287
0.360085829136 1.62495999411 2.60513894682
0.367571785533 1.64528667226 2.65229373702
0.375213370223 1.66565629072 2.69939723919
0.383013818621 1.68600801545 2.74660669895
0.390976433402 1.70630770818 2.79407853453
0.399104585903 1.72654624415 2.8419651498
0.407401717548 1.74673760935 2.89041208966
0.415871341306 1.7669168069 2.93955553495
0.42451704318 1.7871376025 2.98952013674
0.433342483722 1.80747014014 3.04041719143
0.442351399584 1.82799846107 3.09234315759
0.451547605104 1.84881796058 3.14537851377
0.460934993913 1.87003281865 3.19958695317
0.470517540592 1.89175344021 3.25501490728
0.480299302349 1.91409394037 3.31169138623
0.49028442074 1.93716970763 3.36962811878
0.50047712342 1.96109507471 3.42881997142
0.510881725935 1.98598112261 3.48924562241
0.521502633549 2.0119336384 3.55086846498
0.532344343107 2.0390512423 3.61363771298
0.543411444943 2.06742369474 3.67748968311
0.554708624818 2.09713038965 3.74234922957
0.56624066591 2.12823903736 3.80813131002
0.578012450835 2.1608045382 3.87474266494
0.590028963715 2.19486804744 3.94208359627
0.602295292289 2.2304562332 4.01004983433
0.614816630068 2.26758073074 4.07853448506
0.627598278532 2.30623779999 4.14743005082
0.640645649374 2.34640819678 4.21663051868

0.653964266795 2.38805727273 4.28603350879
0.667559769839 2.43113532254 4.35554247266
0.681437914784 2.47557820139 4.42506892706
0.695604577575 2.52130823787 4.49453470327
0.710065756315 2.56823546934 4.56387418487
0.724827573806 2.61625922715 4.63303649887
0.739896280135 2.66527009746 4.70198761708
0.755278255329 2.71515228059 4.77071231512
0.770980012047 2.76578636685 4.83921592796
0.787008198346 2.81705254085 4.90752583184
0.803369600489 2.86883421801 4.97569257364
0.820071145824 2.92102210792 5.04379056045
0.837119905712 2.97351868848 5.11191821356
0.854523098523 3.02624306164 5.18019748233
0.872288092693 3.07913614766 5.24877260453
0.890422409845 3.13216615622 5.31780798978
0.908933727968 3.18533425203 5.38748509244
0.927829884674 3.23868030448 5.45799812916
0.947118880514 3.29228857703 5.5295484858
0.966808882365 3.34629316686 5.60233764927
0.986908226887 3.40088294905 5.67655849545
1.00742542406 3.45630570694 5.75238476781
1.02836916076 3.512871041 5.82995859957
1.0497483045 3.57095153936 5.90937597263
1.07157190709 3.63098156496 5.99067008178
1.09384920857 3.69345287113 6.07379269661
1.11658964103 3.75890610843 6.15859380637
1.13980283269 3.82791715124 6.24480011528
1.16349861191 3.90107708609 6.33199334899
1.18768701137 3.97896471897 6.41958985172
1.21237827235 4.06211065181 6.50682359382
1.237582849 4.15095244548 6.59273543041
1.26331141285 4.24578123198 6.67617215521
1.28957485725 4.34668144155 6.75579940197
1.31638430203 4.45346707178 6.83013249874
1.34375109819 4.5656200032 6.89758866458
1.37168683271 4.68223790941 6.95656217298
1.40020333347 4.80200075929 7.0055211777
1.42931267422 4.92316508334 7.04312101889
1.45902717974 5.04359348001 7.0683246356
1.48935943101 5.16082304849 7.0805172184
1.52032227059 5.27217093497 7.07960057721
1.55192880799 5.37486901298 7.06605373827
1.58419242529 5.466214354 7.04095021039
1.61712678277 5.5437190143 7.00592851424
1.65074582469 5.60524265655 6.96311957072
1.6850637852 5.64909465575 6.91504074429
1.72009519439 5.67409775897 6.86447034543
1.75585488439 5.67961168409 6.81431750763
1.7923579957 5.66552079063 6.7675006782
1.82961998359 5.63219403195 6.72684427003
1.86765662461 5.58042728127 6.69499840829
1.90648402331 5.51137788233 6.67438224676
1.94611861905 5.42649939227 6.66714782229
1.98657719294 5.32748164289 6.67515930134
2.02787687497 5.21619813838 6.69998185078

2.07003515123 5.09466002788 6.7428750899
2.11306987137 4.96497390521 6.80478784268
2.15699925609 4.82929982329 6.88635327392
2.2018419049 4.68980633003 6.98788591527
2.24761680399 4.54862095841 7.10938394797
2.29434333425 4.40777704221 7.25054082819
2.34204127949 4.26916027038 7.41076958554
2.39073083481 4.13446018505 7.58924101404
2.44043261516 4.00513219695 7.7849341358
2.49116766405 3.88237446118 7.99669468884
2.54295746248 3.76712155224 8.22329582712
2.59582393804 3.66005412751 8.46349512754
2.64978947414 3.56162151331 8.71608320963
2.70487691958 3.47207290205 8.97992121851
2.76110959812 3.39149268187 9.25396643991
2.81851131845 3.31983606631 9.53728692083
2.8771063842 3.25696225073 9.82906695018
2.93691960427 3.20266343939 10.1286056368
2.99797630331 3.15668903595 10.4353107632
3.06030233246 3.11876497572 10.7486897796
3.1239240803 3.08860860298 11.0683393879
3.188868484 3.06593970866 11.3939347572
3.25516304072 3.0504884077 11.7252190546
3.32283581931 3.04200050783 12.0619937059
3.39191547211 3.04024094658 12.4041095936
3.46243124716 3.04499578066 12.7514592692
3.53441300053 3.05607311815 13.1039701654
3.60789120897 3.07330329963 13.4615987455
3.68289698284 3.0965385623 13.8243255021
3.75946207926 3.12565236265 14.1921507035
3.83761891556 3.16053848634 14.5650907918
3.91740058299 3.20111003858 14.9431753377
3.99884086078 3.24729838029 15.3264444686
4.08197423038 3.29905205561 15.7149466961
4.1668358901 3.35633574056 16.1087370772
4.25346176999 3.4191292322 16.5078756548
4.34188854708 3.48742648945 16.9124261306
4.43215366088 3.56123473119 17.3224547304
4.52429532923 3.64057359348 17.7380292292
4.61835256454 3.72547434499 18.1592181082
4.71436519021 3.81597915804 18.586089821
4.81237385758 3.91214043146 19.0187121496
4.91242006309 4.01402016112 19.4571516355
5.01454616587 4.12168935328 19.9014730709
5.11879540566 4.23522747613 20.3517390424
5.22521192114 4.35472194481 20.8080095151
5.3338407686 4.48026763541 21.2703414529
5.44472794102 4.61196642365 21.7387884673
5.55792038754 4.74992674412 22.2134004911
5.67346603336 4.89426316646 22.6942234734
5.79141379999 5.04509598487 23.1812990921
5.91181362602 5.20255081786 23.6746644827
6.0347164882 5.36675821517 24.1743519821
6.16017442306 5.53785326946 24.6803888844
6.28824054896 5.71597523016 25.192797211
6.41896908852 5.90126711757 25.7115934919

```

6.55241539166 6.09387533513 26.2367885597
6.68863595894 6.29394927852 26.768387357
6.82768846557 6.50164094001 27.3063887564
6.96963178576 6.71710450697 27.8507853947
7.11452601772 6.94049595377 28.401563522
7.26243250901 7.17197262625 28.958702867
7.41341388261 7.41169281838 29.5221765192
7.56753406337 7.65981534101 30.0919508298
7.72485830511 7.9164990826 30.6679853318
7.88545321822 8.1819025622 31.2502326817
8.04938679789 8.45618347535 31.8386386238
8.21672845289 8.73949823335 32.4331419776
8.38754903495 9.03200149703 33.0336746515
8.56192086874 9.33384570604 33.6401616823
8.73991778256 9.64518060521 34.252521303
8.92161513952 9.9661527693 34.8706650393
9.10708986948 10.2969051281 35.4944978364
9.29642050165 10.6375764939 36.1239182163
9.48968719778 10.988301093 36.7588184673
9.68697178616 11.3492081043 37.3990848657
9.88835779621 11.7204212065 38.044597929
10.0939304939 12.1020581374 38.6952327036
10.3037769178 12.4942302671 39.3508590831
10.517985916 12.8970421882 40.0113421603
10.7366481837 13.3105913253 40.6765426101
10.9598563014 13.7349675681 41.3463171025
11.1877047746 14.1702529276 42.020518746
11.4202900733 14.6165212223 42.6989975577
11.6577106731 15.073837793 43.3816009608
11.9000670968 15.5422592512 44.0681743049
12.1474619572 16.0218332626 44.7585614084
12.4 16.5125983677 45.4526051203];

```

```

Rakic_lam=A(:,1);
Rakic_kap=A(:,3);
Rakic_ref=A(:,2);

```

```

if lambda<Rakic_lam(1) ||
lambda>Rakic_lam(length(Rakic_lam))
    y=0;
else
    ind=find(Rakic_lam>=lambda);
    wave_R=Rakic_lam(ind(1));
    if ind(1)==1
        n=Rakic_ref(1);
        k=Rakic_kap(1);
    else
        wave_L=Rakic_lam(ind(1)-1);
        n=(Rakic_ref(ind(1))-Rakic_ref(ind(1)-1))/(wave_R-
wave_L)*(lambda-wave_L)+Rakic_ref(ind(1)-1);
        k=(Rakic_kap(ind(1))-Rakic_kap(ind(1)-1))/(wave_R-
wave_L)*(lambda-wave_L)+Rakic_kap(ind(1)-1);
    end
end
end

```

A3. Matlab code for calculating the effective refractive index of the buffer from the reflection spectrum

```
%to calculate the effective refractive index of the buffer
clear all;
clc;
close all;
% Wavelength file loading
    data1 =
load('E:\Dropbox\Codes\SpacialFFT\2016Cladding\wavelength.txt');
    wavelength = data1(:,1);

    pressure_list=1;%No of the data

    % Import spectrum from the first data set for choosing a km
    file_name = [num2str(pressure_list) '.txt'];
    data = load(file_name);
    intensity0 = data(:,1);
    intensity=smooth(intensity0,10,'moving');

% Plot the data with peaks identification
    fig_h1 = figure('Position', [10 425 600 295]);
    figure(fig_h1)
    plot(wavelength,intensity,'b-','LineWidth',2);
    xlabel('Wavelength (nm)')
    ylabel('Intensity')
    title('Original data')
    hold on;

    PeakTo=0.01; % peak tolerance

    % Find peaks from Origin result and plot them
    delta = (max(intensity)-min(intensity))*PeakTo;
    peaks = peakdet(intensity,delta);
    index = peaks(:,1);
    o1_peaks = wavelength(index);

    I1_peaks = intensity(index);

    %plot the markers

plot(o1_peaks,I1_peaks,'rs','MarkerSize',4,'MarkerFaceColor','r')

for n = 1:length(index)
    text(o1_peaks(n),I1_peaks(n),num2str(o1_peaks(n)))
end
```



```

figure; % plot the OPD over wavelength

for k=1:length(o1_peaks)-1
OPD(k)=o1_peaks(k)^2/(o1_peaks(k+1)-o1_peaks(k))/1000; %OPD in
um
plot(o1_peaks(k),OPD(k), 's','markersize', 8);
hold on;

end

%calculate n2
n1=1.4580; %cladding RI
p=1055; %grating period in nm

Z=28e4; %fiber length in um

for m=1:length(OPD)

%calc 1st order diffraction angle for each wavelength
diffa=asin(o1_peaks(m)/p/n1);
thetal=pi/2-diffa;

clear x;
syms x;
a=double(solve(OPD(m)==Z*n1/sin(thetal)*(1-(x^2)/(n1^2)), x));

if numel(a)==2
n2(m)=a(1,1);
n3(m)=a(2,1);
elseif numel(a)==1;
n2(m)=a(1,1);
n3(m)=a(1,1);
end

if n2(m)>n3(m)
n4(m)=n2(m);
else
n4(m)=n3(m);
end

a=double(solve(OPD(m)==Z*(x/sin(thetal)-n1)/1000, x));

if numel(a)==2
n2(m)=a(1,1);
n3(m)=a(2,1);
elseif numel(a)==1;
n2(m)=a(1,1);

```

```

        n3(m)=a(1,1);
    end

    if n2(m)>n3(m)
        n5(m)=n2(m);
    else
        n5(m)=n3(m);
    end

end

%Plot results
o1_peaks=o1_peaks(1:length(o1_peaks)-1);
figure;
    plot(o1_peaks,n4, 's','markersize', 8, 'color','k');hold on;
    plot(o1_peaks,n5, 's','markersize', 8, 'color','r');

    title(['This figure used list = ', num2str(pressure_list)])
    hold on;

```

A4. Input for FDTD Solution to calculated the mode field distribution

- a. Core radius = 4.9 um
- b. Core refractive index = 1.46
- c. Cladding radius = 62.5 um
- d. Core refractive index = 1.458
- e. Buffer radius = 125 um
- f. Buffer refractive index = 1.456 (for wavelength 840nm)
- g. Buffer refractive index = 1.5132 (for wavelength 736nm)

Appendix B: Protocol for Nanofabrication on Fiber Facet and additional samples fabricated

B1. Protocol for Nanofabrication on Fiber Facet

- 2) To fabricate the on-fiber nanophotonic structures such as in Figure 4.1(a), choose a bundle of fibers depends on what kind of fibers you want to fabricate. Roughly cut them to the length you want, typically 30 cm to 50 cm.
- 3) Cleave each fiber. Exam the cleave angle under the microscope. A typical cleave angle of $\pm 0.5^\circ$ should be reached for each fiber.
- 4) Bundle and tape the cleaved fibers on a glass substrate, put them into the sputtering chamber, align their end faces vertically to the sputtering target.
- 5) Next, a thin film of desired thickness will be deposited on the cleaved facet by magnetron sputtering. Depends on the conductivity of the metal layer, you might have to deposit a very thin layer of metal on the sidewall of the fiber to improve the conductivity, which is crucial for the FIB fabrication later.
- 6) Further, a focused ion beam (FIB) (FEI Helios 650 or Tescan Gaia) milling was used to write the nanophotonic pattern on the metal film around the fiber core region.
- 7) There is a typical parameter set used in FEI Helios 650, for a 2D square nanohole array pattern on silver
 - a. Voltage 30 kV (Ion beam voltage)
 - b. Current = 0.79 nA (Ion beam current)
 - c. Tilt angle = 2.1°
 - d. Rotation angle = 51°
 - e. X = 400 nm (square length)

- f. $Y = 400$ nm (square width)
- g. $Z = 500$ nm (how deep to drill)
- h. $P = 1030$ nm (Period)

8) There is a typical parameter set used in Tescan Gaia, for a 1D grating pattern on platinumium

- a. Voltage 30 kV
- b. Current = 63 pA
- c. Tilt angle = -3.5°
- d. Rotation angle = 232°
- e. $W = 130$ nm (square width)
- f. $H = 30$ μ m (square height)
- g. $D = 650$ nm (how deep to drill)
- h. $P = 1055$ nm (Period)

B2. Additional samples fabricated and spectrum results

1) On-fiber plasmonic interferometer labeled “Ag6BA6” with a 2D circular nanohole array pattern (Tescan Gaia). SEM picture and reflection spectrum are shown in Figure A.2.

- a. Voltage 30 kV
- b. Current = 33 pA
- c. Tilt angle = -2.2°
- d. Rotation angle = -152°
- e. $D_{\text{out}} = 340$ nm

- f. $D_{in} = 0$ nm
- g. $Z = 150$ nm
- h. $P = 1040$ nm

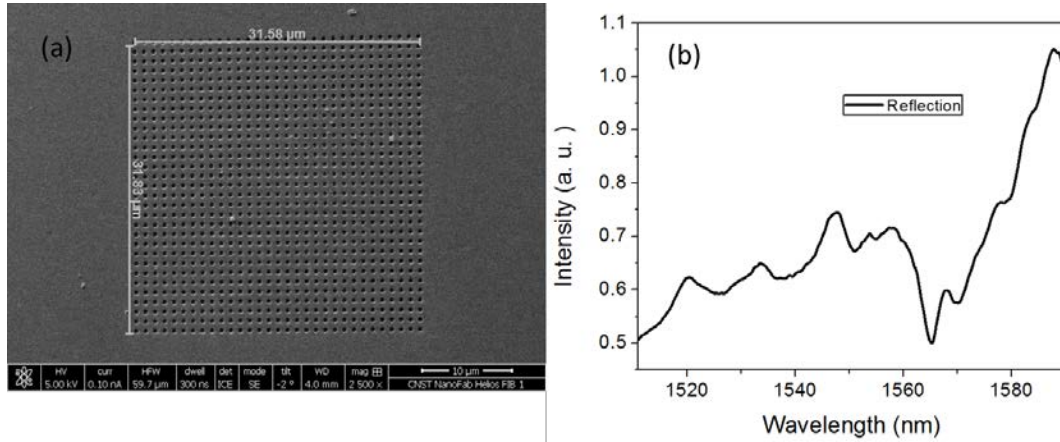


Figure A.2 (a) SEM picture of the sample, (b) reflection spectrum of the sample

2) On-fiber plasmonic interferometer labeled “Ag2BA7” with a 2D circular nanohole array pattern (Tescan Gaia). SEM picture and reflection spectrum are shown in Figure A.3.

- a. Voltage 30 kV
- b. Current = 97.8 pA
- c. Tilt angle = 1.4°
- d. Rotation angle = 28°
- e. $D_{out} = 365$ nm
- f. $D_{in} = 0$ nm
- g. $Z = 150$ nm
- h. $P = 1070$ nm

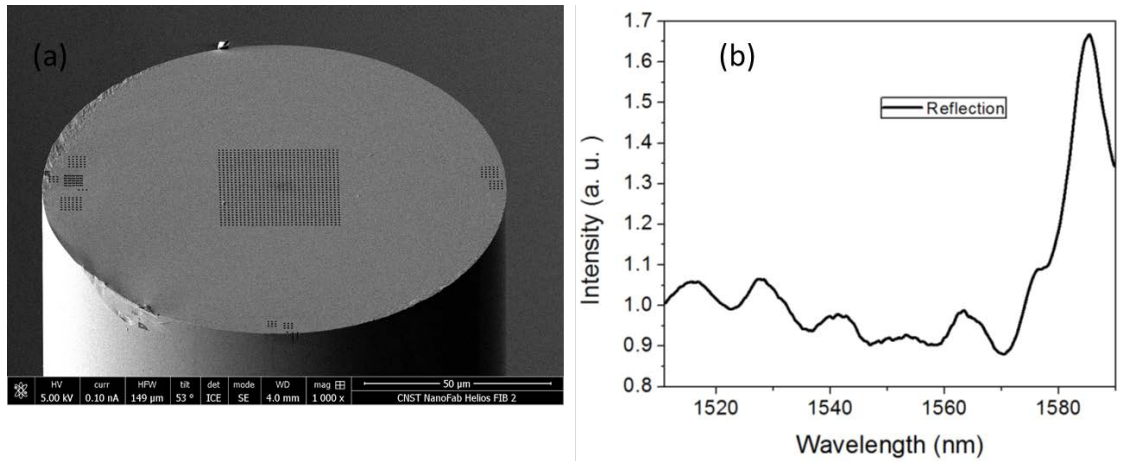


Figure A.3 (a) SEM picture of the sample, (b) reflection spectrum of the sample

3) 1D grating on MMF labeled “Pt4MMF1” (Tescan Gaia). SEM picture and reflection spectrum are shown in Figure A.4.

- a. Voltage 30 kV
- b. Current = 63 pA
- c. Tilt angle = -3.5°
- d. Rotation angle = 232°
- e. $W = 130 \text{ nm}$
- f. $H = 30 \text{ μm}$
- g. $D = 650 \text{ nm}$
- h. $P = 1055 \text{ nm}$

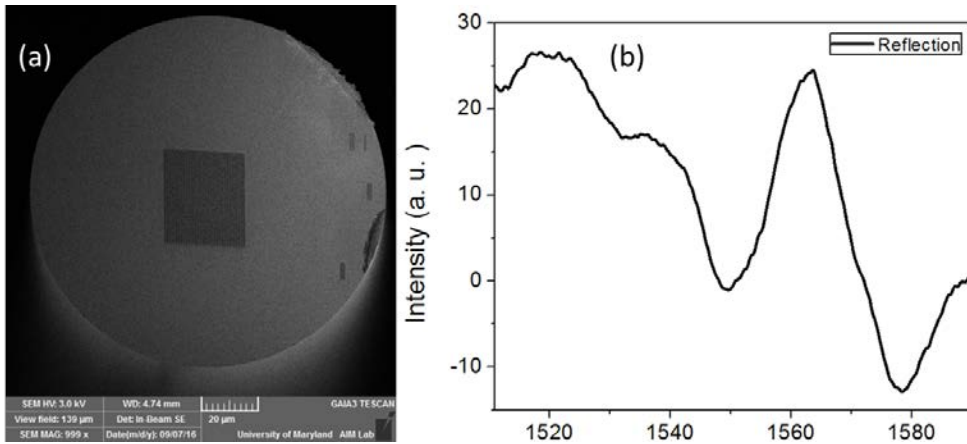


Figure A.4 (a) SEM picture of the sample, (b) reflection spectrum of the sample

Appendix C: List of Publications

Journal Publications

1. Y. Chen, H. Liu, **Z. J. Zhang**, A. K. Gupta, and M. Yu, *Planar photonic crystal based multifunctional sensors*. Applied Optics (submitted).
2. **Z. J. Zhang**, Y. Chen, Z. Wen, H. Liu, and M. Yu, *Buffer-guided-mode and cladding-mode resonances generated by a planar grating on a fiber end face for temperature and axial strain sensing*. Optics Letters (to be submitted).
3. H. Bae, **Z. J. Zhang**, T. Nagaya, Y. Nakamura, P. Choyke, H. Kobayashi and M. Yu, *In Vivo Pressure and Temperature Monitoring Using a Fiber Optic Sensor during Near Infrared Photo-Immunotherapy*. Biomedical Optics Express (to be submitted).
4. **Z. J. Zhang**, Y. Chen, H. Liu, H. Bae, D. A. Olson, A. K. Gupta, and M. Yu, *On-fiber plasmonic interferometer for multi-parameter sensing*. Optics Express 23, 10732-10740 (2015).

5. H.-T. Kim, H. Bae, **Z. J. Zhang**, A. Kusimo, and M. Yu, *Optofluidic microvalve-on-a-chip with a surface plasmon-enhanced fiber optic microheater*. *Biomicrofluidics* 8, 054126 (2014)
6. Y. Chen, **Z. J. Zhang**, M. Yu, *Tunable out-of-plane slow light in resonance induced transparent grating waveguide structures*. *Applied Physics Letters*, 103, 061109 (2013)
7. **Z. J. Zhang** and M. Yu. *Investigation of Physical Limits of Plasmonic Focusing Lens in Different Regions*. *Plasmonics*, 8, 817-827 (2013)

Conference Proceedings

1. **Z. J. Zhang**, H. Bae, T. Nagaya, Y. Nakamura, P. Choyke, H. Kobayashi and M. Yu, *In Vivo Pressure and Temperature Monitoring during Near Infrared Photo-Immunotherapy Using a Fiber Optic Sensor*. *Frontiers in Optics (OSA)*, p. FTh2E. 2., San Jose, USA (2015)
2. **Z. J. Zhang**, Y. Chen, H. Liu, H. Bae, D. A. Olson, A. K. Gupta, and M. Yu, *Ultra-thin multi-parameter sensor achieved with on-fiber plasmonic Interferometer*. *Frontiers in Optics (OSA)*, p. FTh3E. 4., San Jose, USA (2015).
3. **Z. J. Zhang**, and M. Yu, *Subdiffraction-Limit Focusing with Plasmonic Lens Designed in Fresnel Region*. *Frontiers in Optics (OSA)*, p. FTh2F. 5., Orlando, USA (2013)
4. **Z.J. Zhang**, Y. Liu and M. Yu *Investigation of Fiber Optical Tweezers for Nano/Microscale Particle Manipulation* IEEE/SPIE/OSA Student Poster Competition in Optics and Photonics, College Park, USA (2012)

Bibliography

- [1] H. Schiff, Nanoimprint lithography: An old story in modern times? A review, *Journal of Vacuum Science & Technology B*, 26 (2008) 458-480.
- [2] Z. Xie, W. Yu, T. Wang, H. Zhang, Y. Fu, H. Liu, F. Li, Z. Lu, Q. Sun, Plasmonic Nanolithography: A Review, *Plasmonics*, 6 (2011) 565-580.
- [3] D.G. Grier, A revolution in optical manipulation, *Nature*, 424 (2003) 810-816.
- [4] Y. Fu, X. Zhou, Plasmonic Lenses: A Review, *Plasmonics*, 5 (2010) 287-310.
- [5] M.E. Stewart, C.R. Anderton, L.B. Thompson, J. Maria, S.K. Gray, J.A. Rogers, R.G. Nuzzo, Nanostructured Plasmonic Sensors, *Chemical Reviews*, 108 (2008) 494-521.
- [6] C.J. Murphy, Peer Reviewed: Optical Sensing with Quantum Dots, *Analytical Chemistry*, 74 (2002) 520 A-526 A.
- [7] J.D. Joannopoulos, S.G. Johnson, J.N. Winn, R.D. Meade, *Photonic crystals: molding the flow of light*, Princeton university press, 2011.
- [8] R.H. Ritchie, Plasma Losses by Fast Electrons in Thin Films, *Physical Review*, 106 (1957) 874.
- [9] H. Raether, *Surface plasmons on smooth surfaces*, Springer, 1988.
- [10] J. Homola, *Electromagnetic Theory of Surface Plasmons*
Surface Plasmon Resonance Based Sensors, in: J. Homola (Ed.), Springer Berlin Heidelberg, 2006, pp. 3-44.
- [11] E. Ozbay, Plasmonics: Merging Photonics and Electronics at Nanoscale Dimensions, *Science*, 311 (2006) 189-193.
- [12] Z. Liu, J.M. Steele, W. Srituravanich, Y. Pikus, C. Sun, X. Zhang, Focusing Surface Plasmons with a Plasmonic Lens, *Nano Letters*, 5 (2005) 1726-1729.
- [13] N. Fang, H. Lee, C. Sun, X. Zhang, Sub-Diffraction-Limited Optical Imaging with a Silver Superlens, *Science*, 308 (2005) 534-537.
- [14] D.K. Gramotnev, S.I. Bozhevolnyi, Plasmonics beyond the diffraction limit, *Nat Photon*, 4 (2010) 83-91.
- [15] Z. Liu, J.M. Steele, H. Lee, X. Zhang, Tuning the focus of a plasmonic lens by the incident angle, *Applied Physics Letters*, 88 (2006) 171108-171103.
- [16] B. Gjonaj, J. Aulbach, P.M. Johnson, A.P. Mosk, L. Kuipers, A. Lagendijk, Focusing and Scanning Microscopy with Propagating Surface Plasmons, *Physical Review Letters*, 110 (2013) 266804.
- [17] P. Ginzburg, A. Nevet, N. Berkovitch, A. Normatov, G.M. Lerman, A. Yanai, U. Levy, M. Orenstein, Plasmonic Resonance Effects for Tandem Receiving-Transmitting Nanoantennas, *Nano Letters*, 11 (2010) 220-224.
- [18] I.I. Smolyaninov, C.C. Davis, J. Elliott, A.V. Zayats, Resolution enhancement of a surface immersion microscope near the plasmon resonance
Opt. Lett., 30 (2005) 382-384.
- [19] I.I. Smolyaninov, J. Elliott, A.V. Zayats, C.C. Davis, Far-field optical microscopy with a nanometer-scale resolution based on the in-plane image magnification by surface plasmon polaritons, *Physical Review Letters*, 94 (2005) 057401.

- [20] A.V. Zayats, J. Elliott, I.I. Smolyaninov, C.C. Davis, Imaging with short-wavelength surface plasmon polaritons, *Applied Physics Letters*, 86 (2005) 151114.
- [21] I.I. Smolyaninov, C.C. Davis, J. Elliott, G.A. Wurtz, A.V. Zayats, Super-resolution optical microscopy based on photonic crystal materials, *Physical Review B*, 72 (2005) 085442.
- [22] I.I. Smolyaninov, Y.-J. Hung, C.C. Davis, Magnifying Superlens in the Visible Frequency Range, *Science*, 315 (2007) 1699-1701.
- [23] I.I. Smolyaninov, C.C. Davis, Magnifying superlenses and other applications of plasmonic metamaterials in microscopy and sensing, *Chemphyschem*, 10 (2009) 625-628.
- [24] I. Smolyaninov, J. Elliott, G. Wurtz, A. Zayats, C. Davis, Digital resolution enhancement in surface plasmon microscopy, *Appl. Phys. B*, 84 (2006) 253-256.
- [25] I.I. Smolyaninov, Y.-J. Hung, C.C. Davis, Super-resolution optics using short-wavelength surface plasmon polaritons, *Journal of Modern Optics*, 53 (2006) 2337-2347.
- [26] H. Shi, C. Wang, C. Du, X. Luo, X. Dong, H. Gao, Beam manipulating by metallic nano-slits with variant widths, *Opt. Express*, 13 (2005) 6815-6820.
- [27] L. Verslegers, P.B. Catrysse, Z. Yu, J.S. White, E.S. Barnard, M.L. Brongersma, S. Fan, Planar Lenses Based on Nanoscale Slit Arrays in a Metallic Film, *Nano Letters*, 9 (2009) 235-238.
- [28] L. Lin, X.M. Goh, L.P. McGuinness, A. Roberts, Plasmonic Lenses Formed by Two-Dimensional Nanometric Cross-Shaped Aperture Arrays for Fresnel-Region Focusing, *Nano Letters*, 10 (2010) 1936-1940.
- [29] Y. Fu, Y. Liu, X. Zhou, Z. Xu, F. Fang, Experimental investigation of superfocusing of plasmonic lens with chirped circular nanoslits, *Opt. Express*, 18 (2010) 3438-3443.
- [30] H. Gao, J.K. Hyun, M.H. Lee, J.-C. Yang, L.J. Lauhon, T.W. Odom, Broadband Plasmonic Microlenses Based on Patches of Nanoholes, *Nano Letters*, 10 (2010) 4111-4116.
- [31] X.M. Goh, L. Lin, A. Roberts, Plasmonic lenses for wavefront control applications using two-dimensional nanometric cross-shaped aperture arrays, *J. Opt. Soc. Am. B*, 28 (2011) 547-553.
- [32] R. Dorn, S. Quabis, G. Leuchs, Sharper Focus for a Radially Polarized Light Beam, *Physical Review Letters*, 91 (2003) 233901.
- [33] Q. Zhan, Cylindrical vector beams: from mathematical concepts to applications, *Adv. Opt. Photon.*, 1 (2009) 1-57.
- [34] W. Chen, D.C. Abeysinghe, R.L. Nelson, Q. Zhan, Plasmonic Lens Made of Multiple Concentric Metallic Rings under Radially Polarized Illumination, *Nano Letters*, 9 (2009) 4320-4325.
- [35] G.M. Lerman, A. Yanai, U. Levy, Demonstration of Nanofocusing by the use of Plasmonic Lens Illuminated with Radially Polarized Light, *Nano Letters*, 9 (2009) 2139-2143.
- [36] A. Yanai, U. Levy, Plasmonic focusing with a coaxial structure illuminated by radially polarized light, *Opt. Express*, 17 (2009) 924-932.

- [37] P. Wróbel, J. Pniewski, T.J. Antosiewicz, T. Szoplik, Focusing Radially Polarized Light by a Concentric Corrugated Silver Film without a Hole, *Physical Review Letters*, 102 (2009) 183902.
- [38] L. Xiaowei, et al., Plasmonic leak-free focusing lens under radially polarized illumination, *Journal of Optics*, 12 (2010) 085001.
- [39] M. Zhang, J. Du, H. Shi, S. Yin, L. Xia, B. Jia, M. Gu, C. Du, Three-dimensional nanoscale far-field focusing of radially polarized light by scattering the SPPs with an annular groove, *Opt. Express*, 18 (2010) 14664-14670.
- [40] J. Bar-David, G.M. Lerman, L. Stern, N. Mazurski, U. Levy, Generation of a periodic array of radially polarized Plasmonic focal spots, *Optics Express*, 21 (2013) 3746-3755.
- [41] R. Peng, X. Li, Z. Zhao, C. Wang, M. Hong, X. Luo, Super-Resolution Long-Depth Focusing by Radially Polarized Light Irradiation Through Plasmonic Lens in Optical Meso-field, *Plasmonics*, (2013) 1-6.
- [42] R. Oron, S. Blit, N. Davidson, A.A. Friesem, Z. Bomzon, E. Hasman, The formation of laser beams with pure azimuthal or radial polarization, *Applied Physics Letters*, 77 (2000) 3322-3324.
- [43] G.M. Lerman, U. Levy, Generation of a radially polarized light beam using space-variant subwavelength gratings at 1064 nm, *Opt. Lett.*, 33 (2008) 2782-2784.
- [44] Z.e. Bomzon, G. Biener, V. Kleiner, E. Hasman, Radially and azimuthally polarized beams generated by space-variant dielectric subwavelength gratings, *Opt. Lett.*, 27 (2002) 285-287.
- [45] Y. Kozawa, S. Sato, Generation of a radially polarized laser beam by use of a conical Brewster prism, *Opt. Lett.*, 30 (2005) 3063-3065.
- [46] G. Machavariani, Y. Lumer, I. Moshe, A. Meir, S. Jackel, Efficient extracavity generation of radially and azimuthally polarized beams, *Opt. Lett.*, 32 (2007) 1468-1470.
- [47] M.R. Beversluis, L. Novotny, S.J. Stranick, Programmable vector point-spread function engineering, *Opt. Express*, 14 (2006) 2650-2656.
- [48] C. Weibin, et al., Generating cylindrical vector beams with subwavelength concentric metallic gratings fabricated on optical fibers, *Journal of Optics*, 13 (2011) 015003.
- [49] B. Culshaw, Optical Fiber Sensor Technologies: Opportunities and - Perhaps - Pitfalls, *J. Lightwave Technol.*, 22 (2004) 39.
- [50] O.S. Wolfbeis, Fiber-optic chemical sensors and biosensors, *Analytical Chemistry*, 80 (2008) 4269-4283.
- [51] H. Meixner, *Sensors, Micro-and Nanosensor Technology: Trends in Sensor Markets*, John Wiley & Sons, 2008.
- [52] M. Born, E. Wolf, *Principles of optics : electromagnetic theory of propagation, interference and diffraction of light*, 7th (expanded) ed., Cambridge University Press, Cambridge ; New York, 1999.
- [53] J. Homola, S.S. Yee, G. Gauglitz, Surface plasmon resonance sensors: review, *Sensors and Actuators B: Chemical*, 54 (1999) 3-15.
- [54] K.A. Willets, R.P. Van Duyne, Localized surface plasmon resonance spectroscopy and sensing, *Annu. Rev. Phys. Chem.*, 58 (2007) 267-297.

- [55] J. Feng, V.S. Siu, A. Roelke, V. Mehta, S.Y. Rhieu, G.T.R. Palmore, D. Pacifici, Nanoscale Plasmonic Interferometers for Multispectral, High-Throughput Biochemical Sensing, *Nano Letters*, 12 (2011) 602-609.
- [56] M. Consales, A. Ricciardi, A. Crescitelli, E. Esposito, A. Cutolo, A. Cusano, Lab-on-fiber technology: toward multifunctional optical nanoprobe, *ACS Nano*, 6 (2012) 3163-3170.
- [57] G. Kostovski, P.R. Stoddart, A. Mitchell, The Optical Fiber Tip: An Inherently Light-Coupled Microscopic Platform for Micro- and Nanotechnologies, *Advanced Materials*, 26 (2014) 3798-3820.
- [58] S.W. James, R.P. Tatam, Optical fibre long-period grating sensors: characteristics and application, *Measurement Science and Technology*, 14 (2003) R49-R61.
- [59] T. Erdogan, Cladding-mode resonances in short- and long-period fiber grating filters, *Journal of the Optical Society of America A*, 14 (1997) 1760-1773.
- [60] D.B. Stegall, T. Erdogan, Leaky cladding mode propagation in long-period fiber grating devices, *Photonics Technology Letters, IEEE*, 11 (1999) 343-345.
- [61] G. Laffont, P. Ferdinand, Tilted short-period fibre-Bragg-grating-induced coupling to cladding modes for accurate refractometry, *Measurement Science and Technology*, 12 (2001) 765.
- [62] C.-F. Chan, C. Chen, A. Jafari, A. Laronche, D.J. Thomson, J. Albert, Optical fiber refractometer using narrowband cladding-mode resonance shifts, *Appl. Opt.*, 46 (2007) 1142-1149.
- [63] Z. Tian, S.S.H. Yam, H.-P. Loock, Refractive index sensor based on an abrupt taper Michelson interferometer in a single-mode fiber, *Opt. Lett.*, 33 (2008) 1105-1107.
- [64] W. Tao, L. Xinwei, X. Hai, Fiber Inline Core-Cladding-Mode Mach-Zehnder Interferometer Fabricated by Two-Point CO Laser Irradiations, *Photonics Technology Letters, IEEE*, 21 (2009) 669-671.
- [65] L.-Y. Shao, J. Albert, Compact fiber-optic vector inclinometer, *Opt. Lett.*, 35 (2010) 1034-1036.
- [66] H.Y. Choi, K.S. Park, S.J. Park, U.-C. Paek, B.H. Lee, E.S. Choi, Miniature fiber-optic high temperature sensor based on a hybrid structured Fabry-Perot interferometer, *Opt. Lett.*, 33 (2008) 2455-2457.
- [67] D. Lee, M. Yang, C. Qi, J. Dai, X. Wen, W. Xie, An in-line optical fiber refractometer with porous thin film coating, *Sensors and Actuators B: Chemical*, 209 (2015) 602-605.
- [68] R. Morgan, J.S. Barton, P.G. Harper, J.D.C. Jones, Wavelength dependence of bending loss in monomode optical fibers: effect of the fiber buffer coating, *Opt. Lett.*, 15 (1990) 947-949.
- [69] D. Marcuse, Curvature loss formula for optical fibers, *J. Opt. Soc. Am.*, 66 (1976) 216-220.
- [70] W. Gambling, H. Matsumura, C. Ragdale, Field deformation in a curved single-mode fibre, *Electron. Lett.*, 5 (1978) 130-132.
- [71] F.M. Haran, J.S. Barton, S.R. Kidd, J.D.C. Jones, Optical fibre interferometric sensors using buffer guided light, *Measurement Science and Technology*, 5 (1994) 526.

- [72] N. Sung Hyun, Y. Shizhuo, High-temperature sensing using whispering gallery mode resonance in bent optical fibers, *IEEE Photonics Technology Letters*, 17 (2005) 2391-2393.
- [73] J. He, C. Liao, K. Yang, S. Liu, G. Yin, B. Sun, J. Zhou, J. Zhao, Y. Wang, High-Sensitivity Temperature Sensor Based on a Coated Single-Mode Fiber Loop, *J. Lightwave Technol.*, 33 (2015) 4019-4026.
- [74] J.M. Steele, Z. Liu, Y. Wang, X. Zhang, Resonant and non-resonant generation and focusing of surface plasmons with circular gratings, *Opt. Express*, 14 (2006) 5664-5670.
- [75] F. Lopez-Tejiera, S.G. Rodrigo, L. Martin-Moreno, F.J. Garcia-Vidal, E. Devaux, T.W. Ebbesen, J.R. Krenn, I.P. Radko, S.I. Bozhevolnyi, M.U. Gonzalez, J.C. Weeber, A. Dereux, Efficient unidirectional nanoslit couplers for surface plasmons, *Nat Phys*, 3 (2007) 324-328.
- [76] Y. Wang, W. Srituravanich, C. Sun, X. Zhang, Plasmonic Nearfield Scanning Probe with High Transmission, *Nano Letters*, 8 (2008) 3041-3045.
- [77] L. Pan, Y. Park, Y. Xiong, E. Ulin-Avila, Y. Wang, L. Zeng, S. Xiong, J. Rho, C. Sun, D.B. Bogy, X. Zhang, Maskless Plasmonic Lithography at 22 nm Resolution, *Sci. Rep.*, 1 (2011).
- [78] W. Srituravanich, L. Pan, Y. Wang, C. Sun, D.B. Bogy, X. Zhang, Flying plasmonic lens in the near field for high-speed nanolithography, *Nat Nano*, 3 (2008) 733-737.
- [79] S. Yue, Z. Li, J. Chen, Q. Gong, Deep subwavelength confinement and giant enhancement of light field by a plasmonic lens integrated with a metal-insulator-metal vertical nanocavity, *Opt. Express*, 20 (2012) 19060-19066.
- [80] H.X. Yuan, B.X. Xu, B. Lukiyanchuk, T.C. Chong, Principle and design approach of flat nano-metallic surface plasmonic lens, *Applied Physics A: Materials Science & Processing*, 89 (2007) 397-401.
- [81] X.M. Goh, L. Lin, A. Roberts, Planar focusing elements using spatially varying near-resonant aperture arrays, *Opt. Express*, 18 (2010) 11683-11688.
- [82] Q. Chen, Effect of the Number of Zones in a One-Dimensional Plasmonic Zone Plate Lens: Simulation and Experiment, *Plasmonics*, 6 (2011) 75-82.
- [83] Y. Liu, H. Xu, F. Stief, N. Zhitenev, M. Yu, Far-field superfocusing with an optical fiber based surface plasmonic lens made of nanoscale concentric annular slits, *Opt. Express*, 19 (2011) 20233-20243.
- [84] P. Wróbel, T. Antosiewicz, J. Pniewski, T. Szoplik, Single-layer metal nanolenses with tight foci in far-field, *Applied Physics A: Materials Science & Processing*, 103 (2011) 821-825.
- [85] Q. Zhan, Evanescent Bessel beam generation via surface plasmon resonance excitation by a radially polarized beam, *Opt. Lett.*, 31 (2006) 1726-1728.
- [86] X.-W. Chen, V. Sandoghdar, M. Agio, Nanofocusing radially-polarized beams for high-throughput funneling of optical energy to the near field, *Opt. Express*, 18 (2010) 10878-10887.
- [87] R.P. Zaccaria, F. De Angelis, A. Toma, L. Razzari, A. Alabastri, G. Das, C. Liberale, E. Di Fabrizio, Surface plasmon polariton compression through radially and linearly polarized source, *Opt. Lett.*, 37 (2012) 545-547.

- [88] L. Cheng, P. Cao, Y. Li, W. Kong, X. Zhao, X. Zhang, High Efficient Far-Field Nanofocusing with Tunable Focus Under Radial Polarization Illumination, *Plasmonics*, 7 (2012) 175-184.
- [89] D. Pohl, Operation of a Ruby Laser in the Purely Transverse Electric Mode TE₀₁, *Applied Physics Letters*, 20 (1972) 266-267.
- [90] I. Moshe, S. Jackel, A. Meir, Production of radially or azimuthally polarized beams in solid-state lasers and the elimination of thermally induced birefringence effects, *Opt. Lett.*, 28 (2003) 807-809.
- [91] M. Stalder, M. Schadt, Linearly polarized light with axial symmetry generated by liquid-crystal polarization converters, *Opt. Lett.*, 21 (1996) 1948-1950.
- [92] C. Nylander, B. Liedberg, T. Lind, Gas detection by means of surface plasmon resonance, *Sensors and Actuators*, 3 (1982) 79-88.
- [93] B. Liedberg, C. Nylander, I. Lunström, Surface plasmon resonance for gas detection and biosensing, *Sensors and Actuators*, 4 (1983) 299-304.
- [94] B. Liedberg, C. Nylander, I. Lundström, Biosensing with surface plasmon resonance — how it all started, *Biosensors and Bioelectronics*, 10 (1995) i-ix.
- [95] A.J. Haes, R.P. Van Duyne, A Nanoscale Optical Biosensor: Sensitivity and Selectivity of an Approach Based on the Localized Surface Plasmon Resonance Spectroscopy of Triangular Silver Nanoparticles, *Journal of the American Chemical Society*, 124 (2002) 10596-10604.
- [96] A.D. McFarland, R.P. Van Duyne, Single Silver Nanoparticles as Real-Time Optical Sensors with Zeptomole Sensitivity, *Nano Letters*, 3 (2003) 1057-1062.
- [97] D. Cialla, A. März, R. Böhme, F. Theil, K. Weber, M. Schmitt, J. Popp, Surface-enhanced Raman spectroscopy (SERS): progress and trends, *Anal Bioanal Chem*, 403 (2012) 27-54.
- [98] H.F. Schouten, N. Kuzmin, G. Dubois, T.D. Visser, G. Gbur, P.F.A. Alkemade, H. Blok, G.W.t. Hooft, D. Lenstra, E.R. Eliel, Plasmon-Assisted Two-Slit Transmission: Young's Experiment Revisited, *Physical Review Letters*, 94 (2005) 053901.
- [99] R. Gordon, Near-field interference in a subwavelength double slit in a perfect conductor, *Journal of Optics A: Pure and Applied Optics*, 8 (2006) L1.
- [100] R. Zia, M.L. Brongersma, Surface plasmon polariton analogue to Young's double-slit experiment, *Nat Nano*, 2 (2007) 426-429.
- [101] F.J. Rodríguez-Fortuño, G. Marino, P. Ginzburg, D. O'Connor, A. Martínez, G.A. Wurtz, A.V. Zayats, Near-Field Interference for the Unidirectional Excitation of Electromagnetic Guided Modes, *Science*, 340 (2013) 328-330.
- [102] P. Dvořák, T. Neuman, L. Břínek, T. Šamořil, R. Kalousek, P. Dub, P. Varga, T. Šikola, Control and Near-Field Detection of Surface Plasmon Interference Patterns, *Nano Letters*, 13 (2013) 2558-2563.
- [103] Y. Gao, Z. Xin, Q. Gan, X. Cheng, F.J. Bartoli, Plasmonic interferometers for label-free multiplexed sensing, *Optics Express*, 21 (2013) 5859-5871.
- [104] A. Ricciardi, M. Consales, G. Quero, A. Crescitelli, E. Esposito, A. Cusano, Lab-on-Fiber devices as an all around platform for sensing, *Optical Fiber Technology*, 19 (2013) 772-784.
- [105] M. Consales, M. Pisco, A. Cusano, Lab-on-fiber technology: a new avenue for optical nanosensors, *Photonic Sens*, 2 (2012) 289-314.

- [106] S. Feng, X. Zhang, H. Wang, M. Xin, Z. Lu, Fiber coupled waveguide grating structures, *Applied Physics Letters*, 96 (2010) -.
- [107] L.V. Nguyen, D. Hwang, S. Moon, D.S. Moon, Y. Chung, High temperature fiber sensor with high sensitivity based on core diameter mismatch, *Optics Express*, 16 (2008) 11369-11375.
- [108] R. Yang, Y.-S. Yu, C. Chen, Q.-D. Chen, H.-B. Sun, Rapid fabrication of microhole array structured optical fibers, *Opt. Lett.*, 36 (2011) 3879-3881.
- [109] N. Chen, B. Yun, Y. Cui, Cladding mode resonances of etch-eroded fiber Bragg grating for ambient refractive index sensing, *Applied Physics Letters*, 88 (2006) 133902.
- [110] V. Bhatia, A.M. Vengsarkar, Optical fiber long-period grating sensors, *Opt. Lett.*, 21 (1996) 692-694.
- [111] V. Bhatia, Applications of long-period gratings to single and multi-parameter sensing, *Optics Express*, 4 (1999) 457-466.
- [112] V. Bhatia, Properties and sensing applications of long-period gratings, (1996).
- [113] T. Han, Y.-g. Liu, Z. Wang, Z. Wu, S. Wang, S. Li, Simultaneous temperature and force measurement using Fabry-Perot interferometer and bandgap effect of a fluid-filled photonic crystal fiber, *Optics Express*, 20 (2012) 13320-13325.
- [114] L. Li, L. Xia, Z. Xie, D. Liu, All-fiber Mach-Zehnder interferometers for sensing applications, *Optics Express*, 20 (2012) 11109-11120.
- [115] T. Guo, L. Shao, H.-Y. Tam, P.A. Krug, J. Albert, Tilted fiber grating accelerometer incorporating an abrupt biconical taper for cladding to core recoupling, *Optics Express*, 17 (2009) 20651-20660.
- [116] C. Chen, Y.-S. Yu, X.-Y. Zhang, R. Yang, C.-C. Zhu, C. Wang, Y. Xue, F. Zhu, Q.-D. Chen, H.-B. Sun, Compact fiber tip modal interferometer for high-temperature and transverse load measurements, *Opt. Lett.*, 38 (2013) 3202-3204.
- [117] J. Huang, X. Lan, H. Wang, L. Yuan, T. Wei, Z. Gao, H. Xiao, Polymer optical fiber for large strain measurement based on multimode interference, *Opt. Lett.*, 37 (2012) 4308-4310.
- [118] J.A. Schuller, E.S. Barnard, W. Cai, Y.C. Jun, J.S. White, M.L. Brongersma, Plasmonics for extreme light concentration and manipulation, *Nat Mater*, 9 (2010) 193-204.
- [119] W.L. Barnes, A. Dereux, T.W. Ebbesen, Surface plasmon subwavelength optics, *Nature*, 424 (2003) 824-830.
- [120] Y. Yu, H. Zappe, Effect of lens size on the focusing performance of plasmonic lenses and suggestions for the design, *Opt. Express*, 19 (2011) 9434-9444.
- [121] Y. Gao, J. Liu, X. Zhang, Y. Wang, Y. Song, S. Liu, Y. Zhang, Analysis of focal-shift effect in planar metallic nanoslit lenses, *Opt. Express*, 20 (2012) 1320-1329.
- [122] I.I. Smolyaninov, C.C. Davis, Apparent superresolution in near-field optical imaging of periodic gratings, *Opt. Lett.*, 23 (1998) 1346-1347.
- [123] E. Wolf, J.T. Foley, Do evanescent waves contribute to the far field?, *Opt. Lett.*, 23 (1998) 16-18.
- [124] Z. Fang, Q. Peng, W. Song, F. Hao, J. Wang, P. Nordlander, X. Zhu, Plasmonic Focusing in Symmetry Broken Nanocorrals, *Nano Letters*, 11 (2010) 893-897.

- [125] Z.M. Zhang, Nano/microscale heat transfer, McGraw-Hill, New York, NY, 2007.
- [126] J.M. Pitarke, V.M. Silkin, E.V. Chulkov, P.M. Echenique, Theory of surface plasmons and surface-plasmon polaritons, Reports on Progress in Physics, 70 (2007) 1.
- [127] E.D. Palik, G. Ghosh, Knovel (Firm), Handbook of optical constants of solids, in, Academic Press, San Diego, 1998.
- [128] J.D. Jackson, Classical electrodynamics, 3rd ed., Wiley, New York, 1999.
- [129] P. Ruffieux, T. Scharf, H.P. Herzig, R. Völkel, K.J. Weible, On the chromatic aberration of microlenses, Opt. Express, 14 (2006) 4687-4694.
- [130] H.H. Hopkins, The airy disc formula for systems of high relative aperture, Proceedings of the Physical Society, 55 (1943) 116.
- [131] C. Ma, M.A. Escobar, Z. Liu, Extraordinary light focusing and Fourier transform properties of gradient-index metalenses, Physical Review B, 84 (2011) 195142.
- [132] J.W. Strutt, On the diffraction of Object-glasses, Astronom. Soc. Monthly Notice, 33 (1872) 59.
- [133] Y. Gravel, Y. Sheng, Rigorous solution for optical diffraction of a sub-wavelength real-metal slit, Opt. Express, 20 (2012) 2149-2162.
- [134] H.H. Barrett, F.A. Horrigan, Fresnel Zone Plate Imaging of Gamma Rays; Theory, Appl. Opt., 12 (1973) 2686-2702.
- [135] S. Matsuyama, H. Nakamori, T. Goto, T. Kimura, K.P. Khakurel, Y. Kohmura, Y. Sano, M. Yabashi, T. Ishikawa, Y. Nishino, K. Yamauchi, Nearly diffraction-limited X-ray focusing with variable-numerical-aperture focusing optical system based on four deformable mirrors, Scientific Reports, 6 (2016) 24801.
- [136] D. Courjon, J. Bulabois, Real time holographic microscopy using a peculiar holographic illuminating system and rotary shearing interferometer, Journal of Optics, 10 (1979) 125.
- [137] S. Inoué, Foundations of Confocal Scanned Imaging in Light Microscopy, in: J.B. Pawley (Ed.) Handbook Of Biological Confocal Microscopy, Springer US, Boston, MA, 2006, pp. 1-19.
- [138] U. Dürig, D. Pohl, F. Rohner, Near - field optical - scanning microscopy, Journal of Applied Physics, 59 (1986) 3318-3327.
- [139] Y. Oshikane, T. Kataoka, M. Okuda, S. Hara, H. Inoue, M. Nakano, Observation of nanostructure by scanning near-field optical microscope with small sphere probe, Science and Technology of Advanced Materials, 8 (2007) 181-185.
- [140] F.I. Baida, Enhanced transmission through subwavelength metallic coaxial apertures by excitation of the TEM mode, Applied Physics B: Lasers and Optics, 89 (2007) 145-149.
- [141] D. Li, R. Gordon, Electromagnetic transmission resonances for a single annular aperture in a metal plate, Physical Review A, 82 (2010) 041801.
- [142] M. Brust, C.J. Kiely, Some recent advances in nanostructure preparation from gold and silver particles: a short topical review, Colloids and Surfaces A: Physicochemical and Engineering Aspects, 202 (2002) 175-186.

- [143] I. Zoric, M. Zäch, B. Kasemo, C. Langhammer, Gold, platinum, and aluminum nanodisk plasmons: material independence, subradiance, and damping mechanisms, *ACS Nano*, 5 (2011) 2535-2546.
- [144] O. Frazão, L.A. Ferreira, F.M. Araújo, J.L. Santos, Applications of Fiber Optic Grating Technology to Multi-Parameter Measurement, *Fiber and Integrated Optics*, 24 (2005) 227-244.
- [145] M. Tadami, N. Drew, A multi-parameter Bragg grating fiber optic sensor and triaxial strain measurement, *Smart Materials and Structures*, 17 (2008) 035033.
- [146] H.Y. Choi, G. Mudhana, K.S. Park, U.-C. Paek, B.H. Lee, Cross-talk free and ultra-compact fiber optic sensor for simultaneous measurement of temperature and refractive index, *Optics Express*, 18 (2010) 141-149.
- [147] C. Pang, H. Bae, A. Gupta, K. Bryden, M. Yu, MEMS Fabry-Perot sensor interrogated by optical system-on-a-chip for simultaneous pressure and temperature sensing, *Optics Express*, 21 (2013) 21829-21839.
- [148] D.J. Juan Hu, J.L. Lim, M. Jiang, Y. Wang, F. Luan, P. Ping Shum, H. Wei, W. Tong, Long period grating cascaded to photonic crystal fiber modal interferometer for simultaneous measurement of temperature and refractive index, *Opt. Lett.*, 37 (2012) 2283-2285.
- [149] H.-J. van Manen, P. Verkuijlen, P. Wittendorp, V. Subramaniam, T.K. van den Berg, D. Roos, C. Otto, Refractive Index Sensing of Green Fluorescent Proteins in Living Cells Using Fluorescence Lifetime Imaging Microscopy, *Biophysical Journal*, 94 (2008) L67-L69.
- [150] H. Liao, C.L. Nehl, J.H. Hafner, Biomedical applications of plasmon resonant metal nanoparticles, (2006).
- [151] Disclaimer: Certain commercial equipment, instruments, materials, or software are identified in this paper to foster understanding. Such identification does not imply endorsement by NIST, nor does it imply that the items or software identified are necessarily the best available for the purpose.
- [152] F. Miyamaru, M. Hangyo, Finite size effect of transmission property for metal hole arrays in subterahertz region, *Applied Physics Letters*, 84 (2004) 2742-2744.
- [153] J.A. Sánchez-Gil, A.A. Maradudin, Surface-plasmon polariton scattering from a finite array of nanogrooves / ridges: Efficient mirrors, *Applied Physics Letters*, 86 (2005) -.
- [154] J.B. Pendry, L. Martín-Moreno, F.J. Garcia-Vidal, Mimicking Surface Plasmons with Structured Surfaces, *Science*, 305 (2004) 847-848.
- [155] P.B. Catrysse, G. Veronis, H. Shin, J.-T. Shen, S. Fan, Guided modes supported by plasmonic films with a periodic arrangement of subwavelength slits, *Applied Physics Letters*, 88 (2006) 031101.
- [156] S.H. Mousavi, A.B. Khanikaev, B. Neuner, Y. Avitzour, D. Korobkin, G. Ferro, G. Shvets, Highly Confined Hybrid Spoof Surface Plasmons in Ultrathin Metal-Dielectric Heterostructures, *Physical Review Letters*, 105 (2010) 176803.
- [157] Y.-W. Jiang, L.D. Tzuang, Y.-H. Ye, Y.-T. Wu, M.-W. Tsai, C.-Y. Chen, S.-C. Lee, Effect of Wood's anomalies on the profile of extraordinary transmission spectra through metal periodic arrays of rectangular subwavelength holes with different aspect ratio, *Optics Express*, 17 (2009) 2631-2637.

- [158] B.N. Taylor, Guidelines for Evaluating and Expressing the Uncertainty of NIST Measurement Results (rev, DIANE Publishing, 2009).
- [159] B. Qi, G.R. Pickrell, J. Xu, P. Zhang, Y. Duan, W. Peng, Z. Huang, W. Huo, H. Xiao, R.G. May, A. Wang, Novel data processing techniques for dispersive white light interferometer, *Optical Engineering*, 42 (2003) 3165-3171.
- [160] P. Junghyun, L. Byoungcho, An Approximate Formula of the Effective Refractive Index of the Metal–Insulator–Metal Surface Plasmon Polariton Waveguide in the Infrared Region, *Jpn. J. Appl. Phys.*, 47 (2008) 8449.
- [161] S. Tripura Sundari, K. Srinivasu, S. Dash, A. Tyagi, Temperature evolution of optical constants and their tuning in silver, *Solid State Communications*, 167 (2013) 36-39.
- [162] D.B. Leviton, B.J. Frey, Temperature-dependent absolute refractive index measurements of synthetic fused silica, in: *Astronomical Telescopes and Instrumentation*, International Society for Optics and Photonics, 2006, pp. 62732K-62732K-62711.
- [163] G. White, J. Collins, Thermal expansion of copper, silver, and gold at low temperatures, *Journal of Low Temperature Physics*, 7 (1972) 43-75.
- [164] Y. Fei, Thermal expansion, *AGU reference shelf*, 2 (1995) 29-44.
- [165] S.J. Mihailov, Fiber Bragg grating sensors for harsh environments, *Sensors*, 12 (2012) 1898-1918.
- [166] P. Wang, M. Ding, L. Bo, C. Guan, Y. Semenova, Q. Wu, G. Farrell, G. Brambilla, Fiber-tip high-temperature sensor based on multimode interference, *Opt. Lett.*, 38 (2013) 4617-4620.
- [167] L.V. Nguyen, S.C. Warren-Smith, H. Ebendorff-Heidepriem, T.M. Monro, Interferometric high temperature sensor using suspended-core optical fibers, *Optics express*, 24 (2016) 8967-8977.
- [168] G. Liu, K. Li, P. Hao, W. Zhou, Y. Wu, M. Xuan, Bent optical fiber taper for refractive index detection with a high sensitivity, *Sensors and Actuators A: Physical*, 201 (2013) 352-356.
- [169] X. Zhang, W. Peng, Bent-fiber intermodal interference based dual-channel fiber optic refractometer, *Optics Express*, 23 (2015) 7602-7610.
- [170] F.M. Haran, J.S. Barton, J.D.C. Jones, Determination of monomode fiber buffer properties from bend-loss measurements, *Opt. Lett.*, 18 (1993) 1618-1620.
- [171] R. Morgan, J.D. Jones, J. Barton, P.G. Harper, Determination of monomode fiber buffer properties, *Lightwave Technology, Journal of*, 12 (1994) 1355-1359.
- [172] A. Sharma, Y. Powell-Friend, T. George, L. Phillips, Oscillatory light loss within the cladding of a straight optical fiber: comparison with whispering-gallery modes, *Opt. Lett.*, 23 (1998) 262-264.
- [173] Y. Powell-Friend, L. Phillips, T. George, A. Sharma, A simple technique for investigating whispering gallery modes in optical fibers, *Review of Scientific Instruments*, 69 (1998) 2868-2870.
- [174] J.A. Jay, An overview of macrobending and microbending of optical fibers, White paper of Corning, (2010) 1-21.
- [175] Z. Zhang, Y. Chen, H. Liu, H. Bae, D.A. Olson, A.K. Gupta, M. Yu, On-fiber plasmonic interferometer for multi-parameter sensing, *Optics Express*, 23 (2015) 10732-10740.

- [176] E. Garmire, J. Hammer, H. Kogelnik, F. Zernike, T. Tamir, *Integrated optics*, Springer Science & Business Media, 2013.
- [177] E. Li, X. Wang, C. Zhang, Fiber-optic temperature sensor based on interference of selective higher-order modes, (2006).
- [178] Z. Zhang, y. chen, H. Liu, H. Bae, D.A. Olson, A.K. Gupta, M. Yu, Ultra-Thin Multi-Parameter Sensor Achieved with on-Fiber Plasmonic Interferometer, in: *Frontiers in Optics 2015*, Optical Society of America, San Jose, California, 2015, pp. FTh3E.4.
- [179] Z. Zhang, H. Bae, T. Nagaya, Y. Nakamura, P. Choyke, H. Kobayashi, M. Yu, In Vivo Pressure and Temperature Monitoring during Near Infrared Photo-Immunotherapy Using a Fiber Optic Sensor, in: *Frontiers in Optics 2015*, Optical Society of America, San Jose, California, 2015, pp. FTh2E.2.
- [180] L. Xu, L. Jiang, S. Wang, B. Li, Y. Lu, High-temperature sensor based on an abrupt-taper Michelson interferometer in single-mode fiber, *Appl. Opt.*, 52 (2013) 2038-2041.
- [181] Z. Yin, Y. Geng, X. Li, X. Tan, R. Gao, V-groove all-fiber core-cladding intermodal interferometer for high-temperature sensing, *Appl. Opt.*, 54 (2015) 319-323.